Memoirs of the Faculty of Engineering, Nagoya University
Vol. 39, No. 2 (1987)

MEASUREMENT OF RADIATION AND RADIOACTIVITY

TAMAKI WATANABE, CHIZUO MORI,
HIROSHI MIYAHARA and TAKAHIKO AOYAMA

Department of Nuclear Engineering

(Received October 26, 1987)

Abstract

Studies in our laboratory on the detection and measurement of radiation and radioactivity which have been continued for the last more than twenty years are reviewed. As fundamental works, the mean free path length, energy loss and penetration ranges of electrons with a few keV in aluminum and stearic-acid monomolecular layers were measured. Gas multiplication factors in proportional counters with cylindrical- and rectangular-cathodes which have been extensively used in our works were examined experimentally and theoretically. Position-sensitive proportional counters of a charge division type were examined and found some new applications.

The absolute radioactivity of β- and γ-ray emitting nuclide sources can be determined by applying $4\pi\beta$-γ coincidence absorption method. The sources for $4\pi\beta$ counting using an aluminum compound which brought less self-absorption of β-rays were prepared successfully. Electrical conductivity of the thin film for source backing was evaluated. A new method with a position-sensitive proportional counter was developed for absolute activity measurement of gaseous samples.

There are now intensive needs for tritium surface contamination monitor and gas monitor. Recently, we succeeded in developing a proportional counter with air as counting gas, named air proportional counter, for β-ray detection and applied it to tritium surface contamination monitor and gas monitor. A hybrid spark chamber was developed to obtain the image of geometrical distribution of β-ray emitting nuclides.

CONTENTS

1. Introduction 326
2. Energy loss and penetration of low energy electrons 327
    2. 1. Energy loss of low energy electrons in aluminum 327
        2. 1. 1. Mean free path for plasmon excitation in aluminum 327
        2. 1. 2. Stopping power of low energy electrons in aluminum 330
    2. 2. Energy loss of low energy electrons in organic material 331
        2. 2. 1. Mean free path of low energy electrons in stearic-acid 331
        2. 2. 2. Penetration range of low energy electrons in stearic-acid 334
    2. 3. Some applications of low energy radiations emitted from radioisotopes 336
        2. 3. 1. A new method of thin film thickness measurement 336
        2. 3. 2. Energy calibration source emitting very low energy X-rays .. 338
3. Proportional counters 340
    3. 1. Gas multiplication factor 341
        3. 1. 1. Evaluation of gas multiplication formulas for coaxial counter 341
        3. 1. 2. Gas multiplication factor in rectangular counters 342
        3. 1. 3. Effects of electron mean free path and ionization potential on gas multiplication 343
        3. 1. 4. Theoretical consideration on gas multiplication 344
    3. 2. Saturation and inordinate increase of gas multiplication factor 345
        3. 2. 1. Gas multiplication for low energy X-rays 345
        3. 2. 2. Gas multiplication for α-particles 346
        3. 2. 3. Gas multiplication for ^{3}H β-rays 347
    3. 3. Position-sensitive proportional counter (PSPC) 350
        3. 3. 1. Charge division type PSPC with resistive anode wire 350
        3. 3. 2. Charge division type PSPC with carbon fiber anode wire 351
4. Standardisation of radioactivity 352
    4. 1. Standardisation of solid source 353
        4. 1. 1. Various system for coincidence counting 354
            4. 1. 1. 1. Ordinary $4\pi\beta$-γ coincidence system 354
            4. 1. 1. 2. X-γ coincidence system 354
            4. 1. 1. 3. $4\pi\beta$-γ coincidence system using a thin $4\pi\beta$ counter operated by negative high voltage 355
            4. 1. 1. 4. $4\pi\beta$-γ coincidence system using a multi source $4\pi\beta$ counter 356
            4. 1. 1. 5. $4\pi\beta$-γ coincidence system using a pressurized $4\pi\beta$ counter 357
        4. 1. 2. Optimisation of experimental condition and efficiency function 357
            4. 1. 2. 1. Electrical conductivity of source backing film 357
            4. 1. 2. 2. Geometry of source supporting ring 358
            4. 1. 2. 3. Calculation of theoretical efficiency function 359
            4. 1. 2. 4. Optimisation of efficiency function 360
        4. 1. 3. Source preparation and evaluation 362
            4. 1. 3. 1. Thickness measurement by α particle gauge 362
            4. 1. 3. 2. Source preparation by electrospraying method 363
            4. 1. 3. 3. Source preparation by aluminum chloride treatment method 364
            4. 1. 3. 4. Evaluation of self absorption 365
        4. 1. 4. Absolute radioactivity measurement and application 366

4. 1. 4. 1. Absolute standardisation of ^{55}Fe 366
4. 1. 4. 2. Absolute standardisation of ^{85}Sr 367
4. 1. 4. 3. Absolute standardisation and measurement of decay data of ^{86}Rb and ^{103}Ru 368
4. 1. 4. 4. Effect of ^{55}Fe impurities for standardisation of ^{59}Fe 369
4. 2. Standardisation of gaseous source 370
4. 2. 1. A new principle of the standardisation method............... 370
4. 2. 2. Experimental apparatus and its characteristics 372
4. 2. 3. Direct measurement of radioactivity of ^{3}H-labeled methane 373
5. Radioactivity monitors 374
5. 1. Spark chambers 374
5. 1. 1. A parallel plate spark chamber for α-activity imaging 374
5. 1. 1. 1. Description of a spark chamber 374
5. 1. 1. 2. Dependence of sparking voltage on the specific ionization of charged particles 374
5. 1. 1. 3. α-activity imaging for α- and β-active samples ... 376
5. 1. 2. A hybrid spark chamber for β-activity imaging 376
5. 1. 2. 1. Principle and construction 376
5. 1. 2. 2. Electronic circuitry — a thyratron discharge circuit 377
5. 1. 2. 3. Spatial resolution 378
5. 2. Air proportional counters 379
5. 2. 1. Primary electron removal in cylindrical counters 379
5. 2. 2. Design consideration for tritium counters 381
5. 2. 3. Application to a tritium surface-contamination monitor 383
5. 2. 3. 1. Construction 383
5. 2. 3. 2. Optimum operation voltage 383
5. 2. 3. 3. Detection limit 384
5. 2. 4. Application to a tritium-in-air monitor 385
5. 2. 4. 1. Principle and construction 385
5. 2. 4. 2. Tritium monitoring in a γ-ray field. 386
5. 3. Background-compensated GM counters 387
5. 3. 1. Principle and construction 387
5. 3. 2. Electronic circuitry and counter characteristics 387
5. 3. 3. Application to a survey meter 389
5. 4. A tritium-in-air monitor using liquid scintillation counter 390
6. Summary 391
Acknowledgements 391
References 391

1. Introduction

Measurement of radiation and radioactivity is one of the most important means in the utilization of nuclear energy. Although there are a variety of the methods of the measurement depending on the kind of radiation and on the purpose, we have developed mainly the methods of absolute measurement and monitoring of radioactivity for more than twenty years. Also, the interaction of low energy radiation with matter and the characteristics of proportional counters have been studied as fundamental works concerning the above.

Since the measurements of low energy electrons, β-rays and X-rays are comparatively difficult, the available data on the mean free path length, energy loss and penetration range of low energy radiations are scarce. We prepared very thin specimen films through which a few keV electrons could pass, and the above physical data were measured. Concerning radiation detectors, proportional counters have mainly been studied because of their utilization in our laboratory for the internal sample counting method such as $4\pi\beta$-counting, gaseous sample counting and imaging method.

On the standardisation of radionuclides, $4\pi\beta$-γ coincidence absorption method is usually applied to β- and γ-ray emitting nuclides for obtaining the absolute radioactivity of a solid source by means of the extrapolation of β-detection efficiency to unity. Pressurized $4\pi\beta$ counters developed by A. P. Baerg made the extrapolation method easy. We have extensively improved this technique. Absolute measurement of radioactivity of gaseous nuclides was usually carried out by the internal counting which had a serious defect called the end effect. We have developed a new method by using a position-sensitive proportional counter to eliminate the defect.

We also have made efforts on the development and applications of air proportional counter which uses air as counting gas. It was difficult to operate air proportional counter for β-rays due to the oxygen molecules in air which capture free electrons. We succeeded, however, to develop the air proportional counter for β-ray detection and applied it to monitorings of the tritium surface contamination and tritium gas concentration in air. In the field of radiation imaging, we applied proportional counters to obtaining the distribution of β-emitters. A hybrid spark chamber which had regions of ionization chamber and proportional counter was developed for imaging of β-ray emitting nuclides.

2. Energy loss and penetration of low energy electrons

In the measurement of nuclear radiations, the interaction of low energy electrons or low energy β-rays with matter such as energy loss and penetration range is very important in the fields of radiation measurement and radiation health physics. However, since the range of electrons with energy less than a few keV is very short, the precise measurement of the energy loss and the range of these electrons is difficult and the experimental works are scarce. Very thin film specimens were specially prepared and hence low energy electrons could pass through them. Mean free path, energy loss and range were measured with the instruments fabricated for the purposes. Low energy radiations emitted from radioisotopes were used in new applications by making the most of their strong interactions with matter.

2. 1. Energy loss of low energy electrons in aluminum

2. 1. 1. Mean free path for plasmon excitation in aluminum

The ratio of plasmon loss to the total energy loss of low energy electrons has not been well known. Only Quinn's theoretical work (2. 1) gave the ratio to be more than ten percent in aluminum. The data of the mean free path (mfp) for plasmon excitation are necessary for the evaluation of this ratio. Any measurements of the mfp in the low energy region have not been carried out except for the Kanter's work (2. 2) because of the following problems in the use of very thin specimen films; 1) the thickness determination of a thin film, 2) the evaluation of the microscopic thickness variation in a film and 3) the estimation of the effect of the surface contamination and oxidation.

The mfp for plasmon excitation of electrons with energy of a few keV (2. 3) is presented in this section with discussions of the problems mentioned above and those of the influence of the angular dispersion of electrons due to plasmon excitation and the effect of electron diffraction. The experimental setup is shown in Fig. 2. 1. The energy distribution of electrons passed through a thin aluminum film was measured by an analyzer of a 127° electrostatic condenser type with an orbit radius of 50 mm. The energy resolution and angular resolution were 3 eV and 3 milliradians, respectively. An example of the energy loss spectra is shown in Fig. 2. 2. which was observed for electrons with zero deflection behind the aluminum film with a thickness of 240 A° for 6 keV electrons. The first peak corresponds to no loss peak and the others to the first plasmon loss peak, the second plasmon loss peak etc. The spectrum includes some informtions about the interaction of electrons with aluminum, for example the mfp for plasmon excitation, stopping power and the ratio of plasmon loss to the total energy loss. Only the mfp for plasmon excitation is discussed in this section.

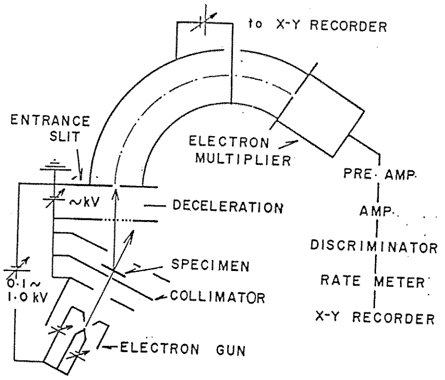

Fig. 2. 1. Electron transmission experimental setup.

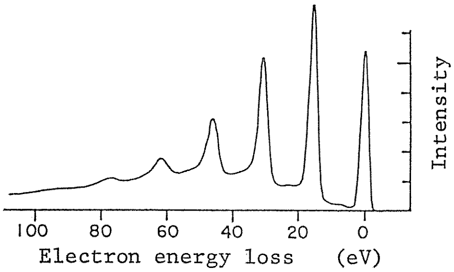

Fig. 2. 2. Electron energy loss spectrum.

The intensity of each peak is expressed by Poisson distribution,

$$P_N(t/\lambda_p) = (t/\lambda_p)^N \exp(-t/\lambda_p)/N\,! \qquad (2.1)$$

where P_N is the relative intensity of the Nth plasmon loss peak, t is the thickness of the film and λ_p is the mfp for plasmon excitation. The ratio between P_{N+1} and P_N is equal to $(t/\lambda_p)/(N+1)$ and can be used for the determination of the value of λ_p.

Very thin self-supporting films of aluminum were prepared as follows. An aluminum thin film was formed on a cleaved surface of a single crystal of sodium chloride by vacuum evaporation, then detouched from the crystal onto water surface and supported on a sheet of nickel grid of 500 mesh. The precise determination of the film thickness was one of the most essential points in this experiment. The authors developed a new nondestructive method (2. 4-5) based on the absorption of Mn K Auger electrons emitted from an ^{55}Fe source as will be described in section 2. 3. 1. With this method, the thickness of films was determined with the accuracy of 20 A° in the measurable thickness range from 50 to 500 A°. The microscopic structure of a film with a thickness of 150 A° was examined with an electron microscope as shown in Fig. 2. 3. (a). The sectional view is shown in (b). There was a thickness variation near grain boundaries, the influence of which was evaluated by taking into account the exponential characteristics of electron transmission (2. 3). It was found, as a result, that, the influence of the thickness variation gave 20 % error in average to the measured mean free path for plasmon excitation.

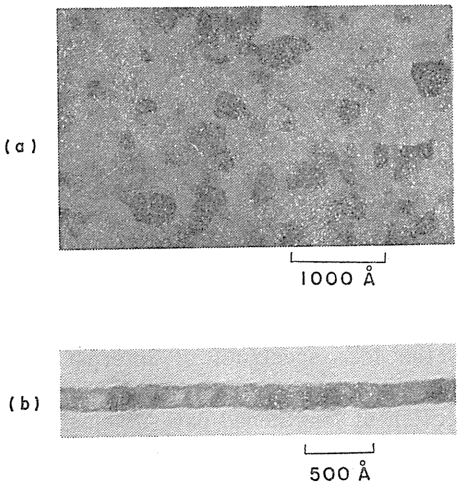

Fig. 2. 3. Fine structure of an aluminum film.

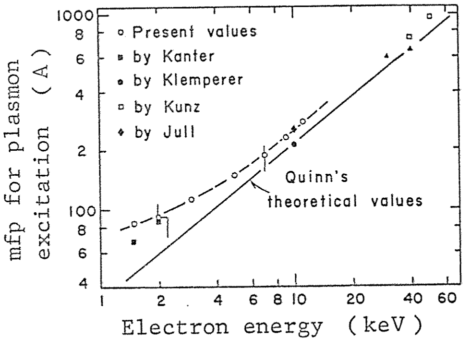

Fig. 2. 4. The mfp for plasmon excitation.

The thickness of oxide layer of the surface was evaluated by observing the binding energy and the intensity of 2p electrons by X-ray excited photoelectron technique and the result showed that the thickness was about 15 A°. The effects of angular dispersion and electron diffraction were also evaluated. The measurement of the mfp for plasmon excitation was carried out with several specimens with various thicknesses. No significant thickness dependence was found, which showed that the increase of the effective path length of electrons in a film could be negligible and that the various evaluations given were proper. Then the representative mean free path in each energy was obtained by averaging the measured values for all specimens. The results are shown in Fig. 2. 4 together with Quinn's theoretical values (2. 1) and other experimental values (2. 6-8). In the lower energy region especially for 1. 5 and 2 keV, the present values were almost twice the theoretical ones. The mfp for plasmon excitation was used for the determination of the ratio of plasmon excitation loss to the total energy loss in the next section.

2. 1. 2. *Stopping power of low energy electrons in aluminum*

There is no all-inclusive and rational theory about the interactions between electrons and matter in low energy region. Experimentally the stopping power in various gaseous materials has been presented, for example by Peterson-Green (2. 9). The result could be explained reasonably by theories (2. 10-11). In the theories, however, gaseous materials were regarded as isolated atoms. In the Peterson-Green's experiment, gaseous materials were used. But it can not be concluded that the theories can be applied without any modifications to the energy transfer process of electrons in solid materials which are constructed with combined atoms.

The experiments with solid materials have been carried out very rarely because of the weak penetration of the electrons in a few keV energy region. There are only the works by Garber (2. 12) and by Kalil (2. 13). Then in the present work (2. 14) with the help of the developments in thin film technique, the stopping power of electrons in aluminum and the ratio of plasmon loss to the total energy loss were obtained in the energy range from 2 to 10. 9 keV by analyzing the energy loss spectra which were measured for electrons passed through thin aluminum films.

The procedure of determination of stopping power was as follows. The mean energy loss of electrons deflected in a direction θ is obtained by the equation;

$$\overline{\Delta E(\theta)}=\int_{\theta}^{\Delta E(\theta)_{\max}}\Delta E(\theta)\cdot I(\Delta E(\theta))\,\mathrm{d}\Delta E(\theta)\frac{1}{2}(1+\cos\theta)\Big/\int_{\theta}^{\Delta E(\theta)_{\max}}I(\Delta E(\theta))\,\mathrm{d}\Delta E(\theta) \qquad (2.2)$$

where $\Delta E(\theta)$ is a value of the energy loss in the loss spectrum of interest and $I(\Delta E(\theta))$ is the relative intensity of electrons which lost the energy $\Delta E(\theta)$. The factor $(1+\cos\theta)/2$ is introduced for the correction of lengthened path of electrons by multiple scattering. The average value of $\overline{\Delta E(\theta)}$ over all the scattering angles gives the mean energy loss of whole electrons which pass through a specimen film, that is

$$\overline{\Delta E}=\int_{0}^{\theta_{\max}}\overline{\Delta E(\theta)}\cdot I(\theta)\,\mathrm{d}\theta\Big/\int_{0}^{\theta_{\max}}I(\theta)\,\mathrm{d}\theta \qquad (2.3)$$

where $I(\theta)$ is a relative intensity, corrected in respect of the solid angle, of electrons which are scattered in the direction θ irrespective of their energy loss. Then by dividing ΔE by the film thickness t, the stopping power is determined as $\mathrm{d}E/dx=\Delta E/t$.

Typical energy loss spectra of electrons with 3 keV are shown in Fig. 2. 5. They were measured at different scattering angles, 0, 1. 3, 3. 9, 10. 5 and 23. 7 degrees for a specimen film with 5. 4 μg/cm^2. With respect to the most probable energy loss, the spectrum measured at zero direction gave the minimum energy loss and it increased with the scattering angle and saturated to be constant over the angles beyond 10. 5 degrees. The probability that electrons lose comparatively large energy increases with the scattering angle of electrons, which was given from the calculation by Gryzinski (2. 11).

The stopping power was measured for eight specimen films with various thicknesses in order to average the errors caused by each specimen characteristic and each measurement of the energy loss spectrum. No significant thickness dependence was found in these values.

The stopping power in each energy was obtained by averaging the measured values for all specimens. The results are shown in Fig. 2. 6 together with the Sugiyama's semiempirical curve (2. 15), which is based on the Bethe-Bloch's theory and the Peterson-Green's experiment for gaseous specimens. In the error estimation, the uncertainty caused by the nonuniformity of the film was most significant, which was about 15 %. Among the other sources of errors the uncertainty of the thickness determination of the film gave the error to be 10 % and the fluctuation of the measured value with each specimen gave about 10 %.

The present values showed the E^{-1} dependence, where E is the incident electron energy. In the higher energy region smaller stopping power was obtained than those given from the Sugiyama's formula, especially at 10. 9 keV, the present value was 60 % of the calculated one, and in the region lower than 5 keV the agreement between the present stopping power and the semi-empirical one was comparatively good within the limit of the experimental errors. It was found in addition that the contribution of the energy loss due to plasmon excitation was about 20 % of the total energy loss, calculated from the mean free path and the plasmon energy in aluminum.

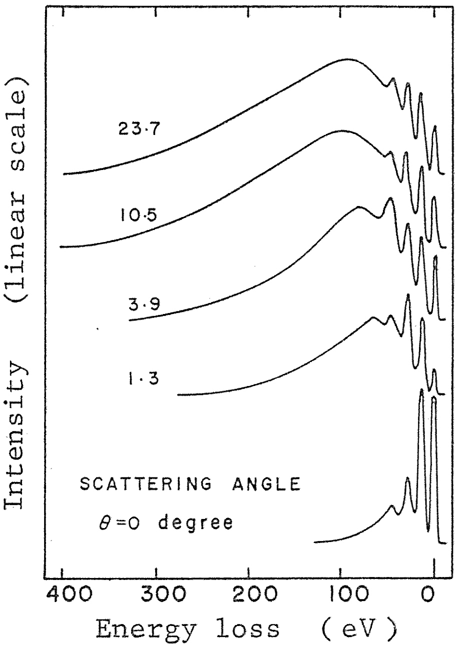

Fig. 2. 5. Energy loss spectra.

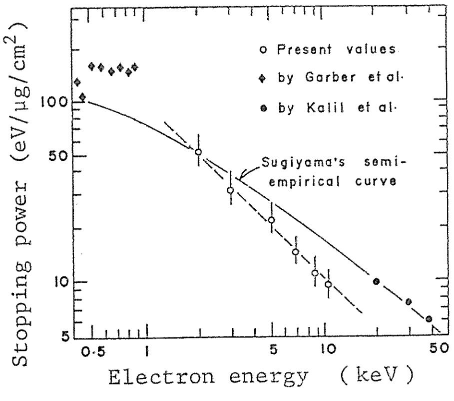

Fig. 2. 6. Stopping power.

2. 2. Energy loss of low energy electrons in organic material

2. 2. 1. Mean free path of low energy electrons in stearic-acid

Energy loss of low energy electrons in organic material is important in the field of radiation health physics. Inelastic mean free path (imfp) of very low energy electrons in stearic cobalt monomolecular layers (stearic Co MML) was obtained by the following method (2. 16). Organic material is generally insulator and hence electron charge-up phenomenon occurs in self-supporting film. X-ray excited photoelctron spectroscopic method (XPS) was applied, in which monochromatic photoelectrons emitted from a substrate plate are transmitted through stearic Co MML deposited on the substrate. Measurement of photoelectron intensity against the thickness of the MML gives escape depth. In this method, electron charge-up phenomenon hardly occurs because of the presence of conductive substrate. Furthermore, extremely thin film, down to about 20 A°, can be deposited on the substrate. Escape depth for electrons with very low energy can therefore be obtained.

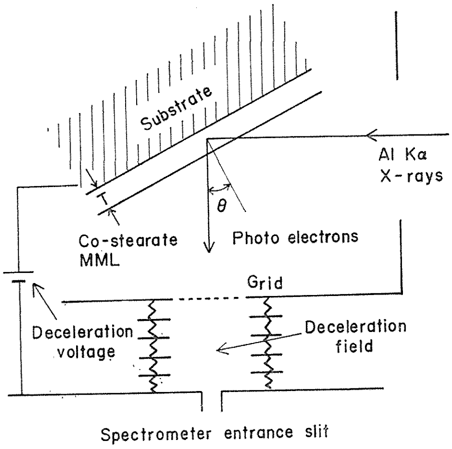

Fig. 2. 7. Schematic view around the sample holder of XPS.

Fig. 2. 7. shows a part of the XPS instrument. The ratio of monochromatic photoelectron intensity I_t passed through the MML with a thickness of t to the intensity I_0 from the substrate without the MML is simply expressed by

$$I_t/I_0=\exp(-t/(\lambda\cos\theta)) \qquad (2.4)$$

where λ is observed mean free path (observed mfp) and θ is the emission angle shown in Fig. 2. 7. Monochromatic photoelectrons excited by Al K X-rays were Au 4f$_{7/2}$(1404 eV), Au 4f$_{5/2}$(1153 eV), Cu 3p$_{1/2,\,3/2}$(1413 eV), Cu LMM Auger electrons (870 eV) and Cu 2p$_{3/2}$ (556 eV).

Stearic Co MML was deposited on a substrate by Blodgett method (2. 17) shown in Fig. 2. 8. Solution of cobalt chloride was dropped into ion-free water in a trough. A paraffin-permiated silk thread was spreaded in a loop over the water surface and a very small amount of the benzene solution of stearic-acid was dropped on the water surface inside the silk thread loop. When piston-oil was dropped outside the loop, stearic Co MML was formed on the surface. Up and down goings of a substrate plate through the MML made stearic Co monomolecular multi-layers as shown in Fig. 2. 9. The conversion factor of hydrogen atoms in carboxyle radicals to cobalt atoms was 0.4±0.04. Some of stearic-acid molecules in such multi-layers liberated from the surface by X-ray irradiation, which seriously affects the measurement of the observed mfp. The liberation of stearic-acid molecules was precisely investigated (2. 18) by using ^{14}C-labeled and ^{60}Co-labeled stearic-acid.

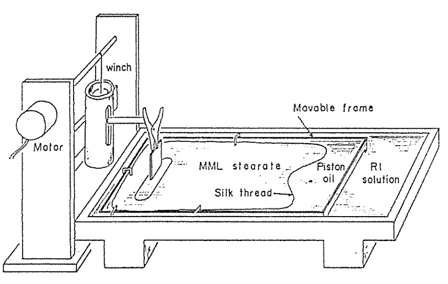

Fig. 2. 8. Setup for sample preparation by stearate MML method.

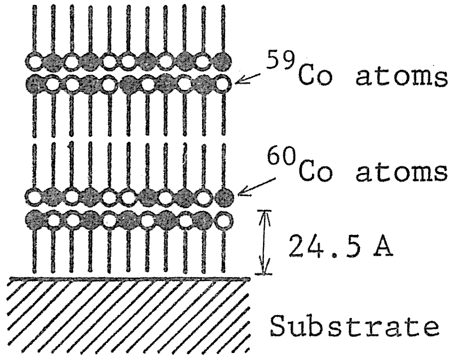

Fig. 2. 9. Cobalt stearate monomolecular multi-layers.

Among many kinds of stearate MML, the liberation of Co stearate molecules was small, about 20 %, compared with other stearates, whose liberations were more than 50 %. The effect of the liberation on the observed mfp was corrected with following equation,

$$I_t/I_0=\sum_{S=0}^{M} {}_MC_s(1-p)^s p^{M-s}\exp(-st/(M\lambda\cos\theta)) \tag{2.5}$$

where M is the number of layers, p is the rate of liberation.

Fig. 2. 10. shows the relation between $I_t(\theta)/I_0(\theta)$ and $1/\cos\theta$. If λ is constant independently of θ, Eq. (2. 5) gives the relation shown by broken lines. The experimental points deviated from the broken lines, which means that the observed mfp obtained by using Eq. (2. 5) is a function of θ. For electrons with higher energy such as 1 keV, the observed mfp was almost independent of θ. Table 2. 1 shows the observed mfp together with other reference values (2. 19). The values of our results are less than one-half of Henke et al.'s. This is probably due to the fact that Henke et al. used barium stearate MML which had a large factor of liberation by X-ray irradiation and they gave no correction for the liberation. The fact that the observed mfp is a function of the emission angle can be attributed to the presence of elastic scattering which changes the path length between the position of the emission of a photoelectron at the substrate surface and the position of the escape from the surface of the stearate MML and accordingly the elastic scattering makes the path length smaller than

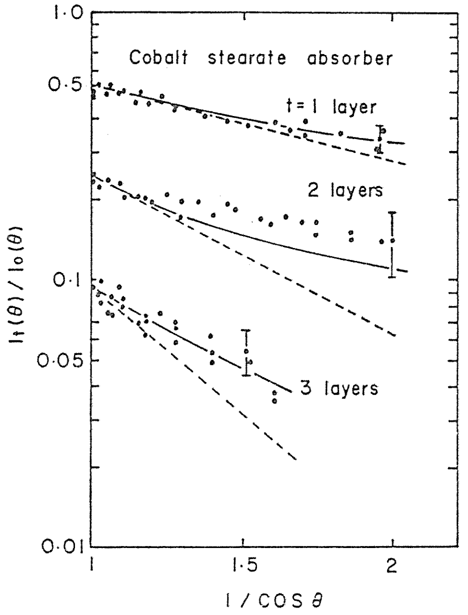

Fig. 2. 10. $I_t(\theta)/I_0(\theta)$ vs. $1/\cos\theta$.

Table 2. 1. Escape depth in organic film.

Material	Electron energy (eV)	Escape depth (Å)	
(Present values)		Emission angle	
		10°	45°
Co-H-stearate	1,404 1,413	40±4	41±6
	1,153	36±5	37±7
	860	32±5	34±7
	556	25±3	30±5
(Reference values)			
Barium stearate	705	60	
	1,350	90	

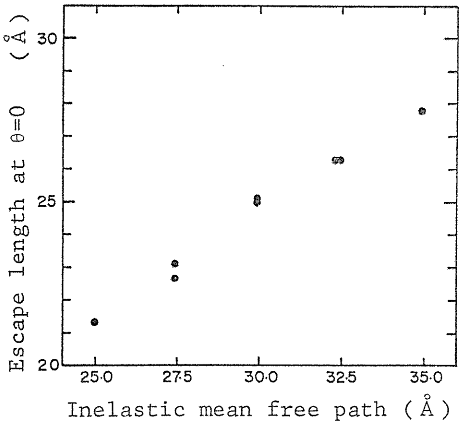

Fig. 2. 11. Inelastic scattering mfp vs. escape length.

the simple geometrical distance at a large angle θ.

The ratio $I_t(\theta)/I_0(\theta)$ obtained by Monte Carlo simulation by taking into account the elastic scattering is shown in Fig. 2. 10. by full lines (2. 20). In this simulation differential cross section of elastic scattering is obtained by modifying Fink's data (2. 21).

Since the mfp for elastic scattering is known by Fink's data, if the value of inelastic scattering mfp is assumed, the observed mfp at $\theta=0$ can be calculated by Monte Carlo simulation. Fig. 2. 11 was obtained by this procedure for electrons with 556 eV. Experimentally observed value at $\theta=0$ for 556 eV electrons was 25 ± 3A°, which gives $30\pm4°$ for inelastic mfp. On the other hand, inelastic mfp for 1500 eV determined by the same procedure was nearly same as the experimental observed value.

2. 2. 2. Penetration range of low energy electrons in stearic-acid

Ranges of electrons in organic matter were measured in the energy range from 0. 4 to 1 keV (2. 22). Stearate MML radioactive sources, being free from self-absorption, were prepared with electron capture decay nuclides which emitted low energy L Auger electrons. Barium stearate MML was appropriate as an absorber for low energy electrons. A double proportional counter (2. 23) was used, which made it possible to measure the intensity of L Auger electrons without disturbance of K Auger electrons.

Absorption characteristics, especially penetration range of electrons with energy less than a few keV is important in various fields. Although the range in organic matter in this energy region has been reported by Cole (2. 24) and Davis (2. 25), it is difficult even to estimate the extent of the error in their experimental values due to the inaccuracy of the thickness of the film. Stearate MML prepared by Blodgett method has been precisely investigated concerning their uniformity, thickness and density. Electron capture nuclides were dissolved in water. Barium stearate was chosen, because it could be stably transferred from the water surface to a substrate surface.

Fig. 2. 12 shows a schematic cross-sectional view of stearate MML radioactive source with a substrate of a dimension of $0.9\times15\times26$ mm. Electron capture nuclides emit K Auger electrons which have higher energy than that of L Auger electrons. A special counter as shown in Fig. 2. 13 was, therefore, constructed to detect only L Auger electrons without the disturbance of K Auger electrons. An electron capture nuclide source was inserted at the center

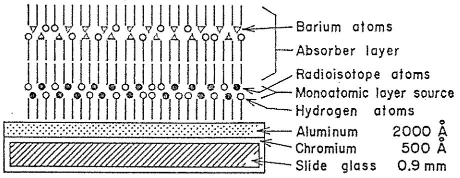

Fig. 2. 12. Stearate MML radioactive source covered with barium stearate absorber.

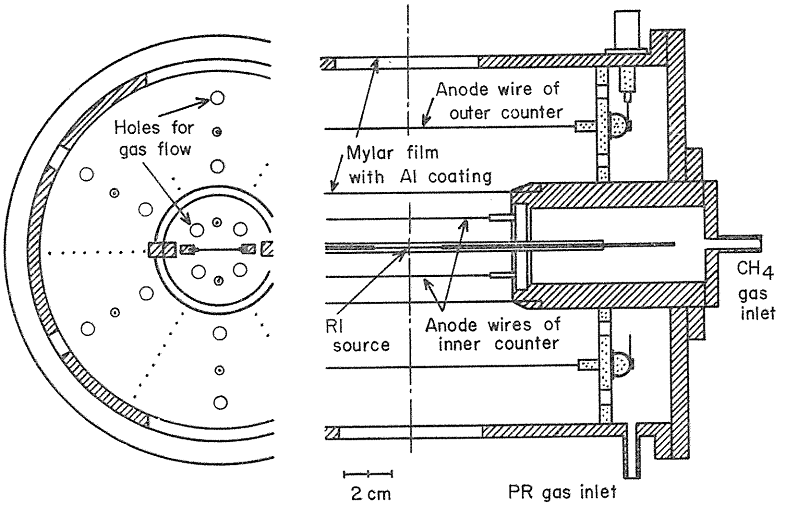

Fig. 2. 13. Sectional view of double proportional counter.

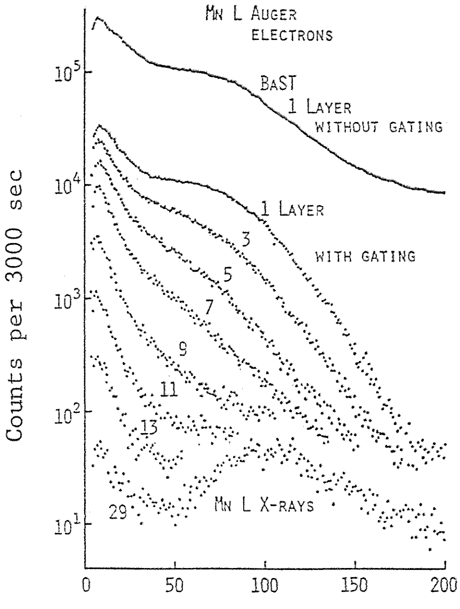

Fig. 2. 14. Energy spectra of Mn L Auger electrons from ^{55}Fe.

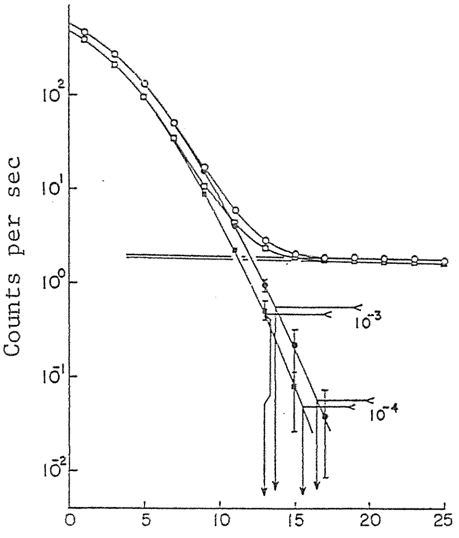

Fig. 2. 15. Mn L Auger electron intensity vs. thickness of Ba stearate monomolecular multi-layers.

of the inner counter. The signals obtained from an inner counter were observed with the gating of K X-ray signals from the outer counter. The energy spectra obtained with this counter are shown in Fig. 2. 14. The intensity of Mn L Auger electrons decreases with the number of layers of barium stearate MML.

Absorption curves of Mn L Auger electrons from ^{55}Fe, as an example, are shown in Fig. 2. 15. Circles and squares correspond to total intensity in a spectrum in Fig. 2. 14 and total intensity minus single electron intensity, respectively. Open circles and squares show the intensities including L X-rays seen in Fig. 2. 14. Extrapolation of the L X-ray intensity and subtraction of it from the total intensity yields attenuation of L Auger electrons which is shown by full circles and squares. For L Auger electrons from various nuclides the penetration ranges may be determined as thickness at which the intensity decreases to the fourth figures according to the usual method to determine the maximum range of β-rays in nuclear physics (this range is referred to as "specified projected range, R-10^{-4}" as defined by ICRU Report 16 (2. 26)) and the intensity decreases to the third figures, R-10^{-3}. The values of the ranges determined were $4.35\,^{+0.63}_{-0.50}$ μg/cm^2 of barium stearate MML for R-10^{-4} and 3.61 ± 0.39 μg/cm^2 for R-10^{-3}. The values corresponding to R-10^{-4} and R-10^{-3} are listed in Table 2. 2.

Table 2. 2. Specified projected range R-10^{-n} of low energy electrons in barium stearate mono-molecular multi-layers.

Nuclide	Auger electron	Energy (keV)	Range(μg/cm^2)	
			R-10^{-3}	R-10^{-4}
^{51}Cr	V L	0.454 ± 0.041	2.91 ± 0.32	$3.65^{+0.55}_{-0.40}$
^{54}Mn	Cr L	0.521 ± 0.047	3.15 ± 0.34	$3.84^{+0.53}_{-0.42}$
^{55}Fe	Mn L	0.578 ± 0.052	3.61 ± 0.39	$4.35^{+0.63}_{-0.50}$
^{57}Co	Fe L	0.647 ± 0.058	4.05 ± 0.60	$4.52^{+0.80}_{-0.70}$
^{65}Zn	Cu L	0.869 ± 0.078	5.73 ± 0.60	$6.26^{+0.77}_{-0.66}$
^{109}Cd	Ag L	2.77 ± 0.25	34.0 ± 3.6	$34.5^{+3.8}_{-3.6}$

Ranges of electrons in organic matter were measured by using a special technique in the energy region 0. 4-1 keV. The errors of the range were estimated by evaluating the thickness, defects of barium stearate MML layer, counting statistics and the effect of single electrons and found to be less than ±15%.

2. 3. *Some applications of low energy radiations emitted from radioisotopes*

2. 3. 1. *A new method of thin film thickness measurement*

A new and simple method (2. 4-5) is proposed for the measurement of thin films of the order of a few μg/cm^2, which is based on the absorption of Mn K Auger electrons emitted from ^{55}Fe. Thin films with a mass per unit area of a few μg/cm^2 are used in various fields of technology. The measurement of a sample weight is usually a destructive method, though it can give absolute mass thickness. Light interferometric method (2. 27) requires vacuum deposition of a small amount of metal on the surface of the film and α-particle absorption method (2. 28-29) requires vacuum instrument. A simple, quick and precise method

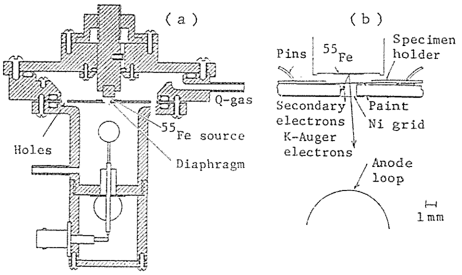

Fig. 2. 16. (a) ^{55}Fe thickness gauge, (b) the central part of the gauge.

is always desirable even if it is a relative method and needs standard samples. The apparatus proposed newly is schematically shown in Fig. 2. 16. The lower part is a bell-type GM counter with Q gas (He 99 %, isobutane 1 %) flow and the upper part contains ^{55}Fe vacuum-evaporated source with an activity of 5000 Bq. Between the upper and the lower parts, there is a diaphragm with a central hole. Auger electrons can pass through the hole toward GM region. On the diaphragm, nickel grid (500 mesh) was attached and supplied with a negative voltage. As a specimen film, vinyl chloride film (VYNS film), collodion film or aluminum film was streched on a metal frame. The role of the nickel grid with negative voltage is the suppression of secondary electrons produced by primary Mn Auger electrons in the space between specimen film and the grid.

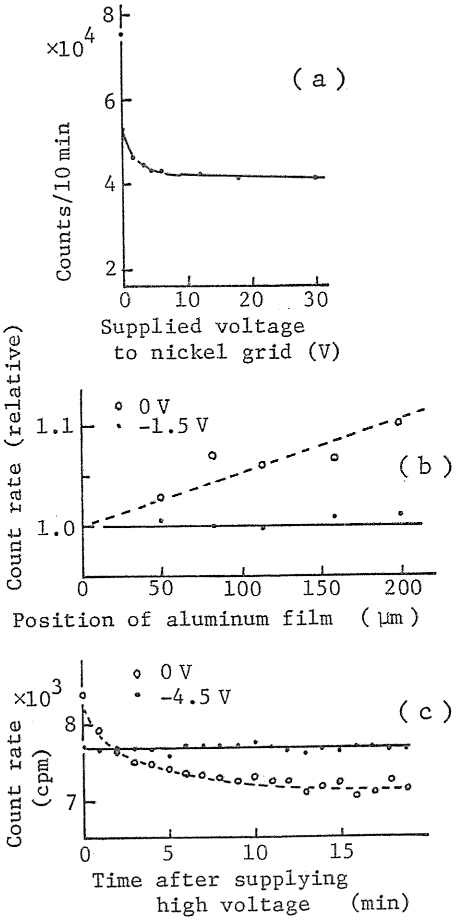

Fig. 2. 17. Effect of nickel grid with negative voltage.

Fig. 2. 17 (a), (b) and (c) show the effect of nickel grid. (a) Count rate decreases with the supplied voltage. (b) Count rate doesn't change with the thickness of aluminum film inserted intentionally between the specimen holder and the diaphragm when a negative voltage is supplied, whereas it changes with the thickness when no voltage is supplied. (c) Count rate doesn't change with time when a negative voltage is supplied.

Fig. 2. 18 shows the relation between count rate and absolute thickness of alumi-

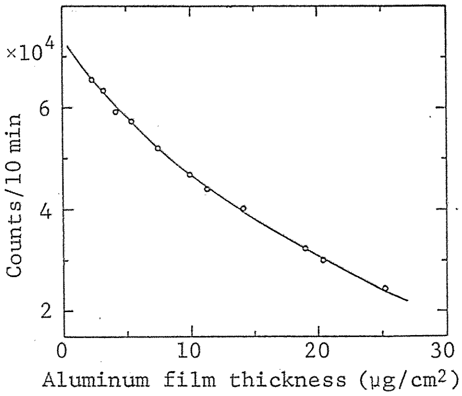

Fig. 2. 18. Calibration curve for aluminum film.

num film measured by atomic absorption analysis. The curve was obtained by the method of least squares, assuming that it was a part of a Gaussian distribution curve. The errors, expressed as standard deviation, in absolute thickness determination were estimated as follows.

a) Standard deviation of the reproducibility of the count rate for the same specimen film: Ten measurements of 10 minutes each for replacing repeatedly the same specimen film, gave a deviation of ±0.7%, that is about ±0.3 μg/cm² error for an aluminum film of 10 μg/cm². The value of ±0.7% included the statistical deviation, ±0.5%, of counts for 10 minutes.

b) The error caused by atmospheric pressure and temperature changes. If an atmospheric pressure change $\varDelta P$, or temperature change $\varDelta T$, occurs during the thickness measurement, they will cause a variation $\varDelta t_g$ of the mass thickness t_g of Q gas in the space between the ^{55}Fe source and the specimen film. The error $\varDelta t_f$ for film thickness t_f due to this effect is estimated as follows. The count rate n can be expressed as

$$n=n_0\left[1-\left(\frac{t_s}{2R_s}+\frac{t_g}{R_g}+\frac{t_f}{R_f}\right)\right], \tag{2.6}$$

under the simple assumption that the number of mono-energetic electrons decreases linearly with absorption thickness, n_0 is the number of Auger electrons without any absorption and t_s is the ^{55}Fe source thickness. R_s, R_g and R_f are electron ranges (2.30) for source material, Q gas and film, respectively. The following relation holds between the mass thickness t_g and its linear length d_g, $d_g/t_g=MPd_g/kT$, where M is the gram molecular weight and k is the gas constant. The variation $\varDelta t_g$ is expressed as

$$\varDelta t_g=t_g\left[\left(\frac{\varDelta P}{P}\right)^2+\left(\frac{\varDelta T}{T}\right)^2\right]^{\frac{1}{2}}. \tag{2.7}$$

This variation $\varDelta t_g$ will be measured as a change $\varDelta t_f$ of specimen film thickness. The reduced value $\varDelta t_f=\varDelta t_g R_f/R_g$ will be considered as the error due to atmospheric change. Substituting numerical values for the electron ranges and $d_g=1$ mm, $\varDelta t_f$ is calculated to be ±0.19 μg/cm² for variations of $\varDelta P=\pm 3$ mmHg and $\varDelta T=\pm 1.5$℃. Thus $\varDelta t_f$ is about 2% at a thickness of 10 μg/cm².

c) The error of the calibration curve resulted from the atomic absorption analysis and estimated to be ±0.4 μg/cm².

After all, the total error of thickness measurement was about ±0.6 μg/cm² for a thickness of 10 μg/cm² of aluminum film. This situation is almost same as VYNS and collodion films.

2, 3. 2. Energy calibration source emitting very low energy X-rays

It is sometimes necessary to give energy calibrations or to find detection efficiencies for a proportional counter when it is used in the fields of soft X-rays and low energy β-rays. Simple calibration sources having an energy below 1.5 keV are not easily available. It was tried to prepare soft X-ray sources (2.31) which emit X-rays with an energy of several hundred eV and have very small dimensions being able to be put even inside 2π or 4π proportional counters.

In an electron capture nuclide, for example, Auger electrons and X-rays are emitted. L X-ray energy is generally very low, several hundred eV, in a low atomic number nuclide and will be utilized for energy calibration. There are however the following various inconveniences on the utilization of such L X-rays. 1) There is rather large self-absorption of L X-rays, it would be therefore better to make a source with vacuum-evaporation method. 2) Since K and L Auger electrons are emitted abundantly, it is necessary to cut these Auger electrons by putting an appropriate absorber over an electron capture nuclide source. 3) Characteristic X-rays contain several monochromatic components. It should be examined, especially for L X-rays, if characteristic X-rays are usable for energy calibration. Radioactive sources were prepared by vacuum-evaporation. An aluminum plate with a thickness of 0. 3 mm and a diameter of 8 mm was used as a substrate.

Fig. 2. 19 shows the energy spectra of radiations emitted from an ^{55}Fe source observed by inserting the source inside a methane gas flow proportional counter. Since it was first intended to have only two characteristic X-rays, Mn L and Mn K X-rays, beryllium (Be) was evaporated onto a substrate to a thickness greater than the penetration range of Mn K Auger electrons and then ^{55}Fe was evaporated in vacuum. Again Be was evaporated to cut Mn K and L Auger electrons. L and K Auger electrons were almost absorbed by the Be coating of 4. 0 μg/cm^2 and 120 μg/cm^2, respectively. Mn L X-rays were clearly observed.

Aluminum (Al) was chosen as a target element instead of Be. On an ^{55}Fe or ^{54}Mn source with Al as substrate, Al was vacuum-evaporated up to a thickness of about 200 μg/cm^2 or 150 μg/cm^2, respectively. The pulse height spectra are shown in Fig. 2. 20 (a) from ^{55}Fe source and (b) from ^{54}Mn source with an energy calibration line. Fig. 2. 21 shows the spectra when the ^{55}Fe source was used in

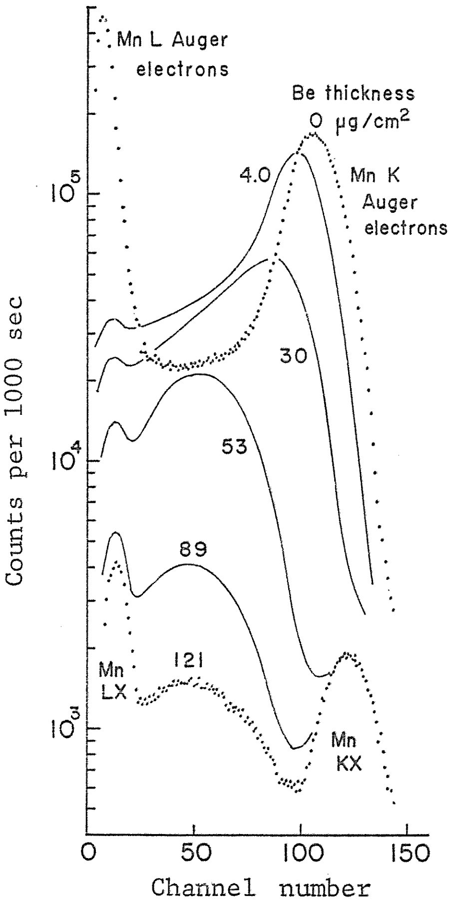

Fig. 2. 19. Pulse height spectra of radiations emitted from ^{55}Fe source in methane.

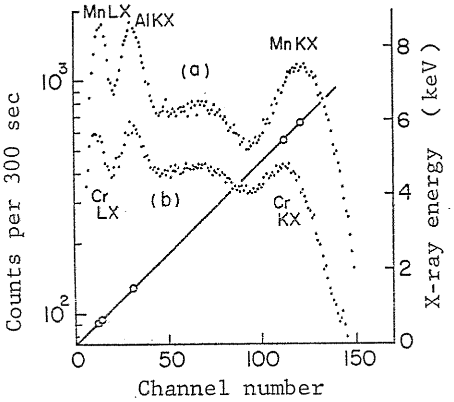

Fig. 2. 20. Characteristic X-rays (a) ^{55}Fe source, (b) ^{54}Mn source and energy calibration line.

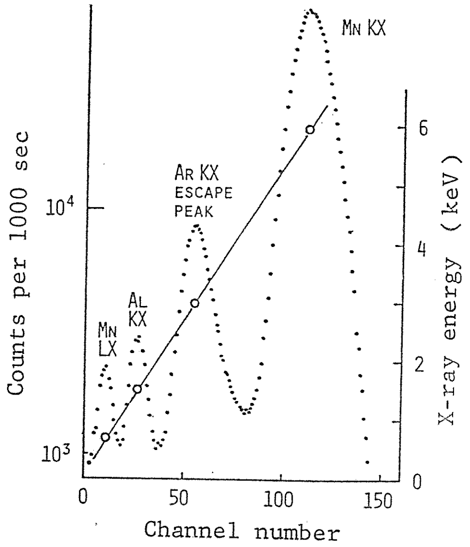

Fig. 2. 21. Pulse height spectra of X-rays from an ^{55}Fe source in P-10 gas.

a PR gas (Ar 90%, CH_4 10%) flow counter. Four peaks including Ar K X-ray escape peak can be used for energy calibration.

When characteristic X-rays are used for energy calibration it is necessary to examine the pulse height at the peak (peak position) and the half width of the observed pulse height distribution, because characteristic X-rays, especially L X-rays, are composed of several monochromatic X-rays. As shown in Table 2. 3 the calculated peak position (2. 31) of the pulse height distribution to be observed for ^{55}Fe X-rays has deviations less than 0. 3% from the weighted mean energy of $K_{\alpha 1}$ and $K_{\alpha 2}$ and the peak position for L X-rays has deviations less than 0. 65% from the energy of $L_{\alpha 1,2}$ X-rays. The deviations of the energy resolution of those complex X-rays from monochromatic X-rays are negligibly small. From Table 2. 3 it can be concluded that it is convenient to use the weighted mean energy of $K_{\alpha 1}$ and $K_{\alpha 2}$ for K X-rays as a peak energy and to use the energy of $L_{\alpha 1,2}$ for L X-rays. The absolute intensity of each characteristic X-rays per decay of ^{54}Mn was calculated theoretically (2. 31-32). The comparison with the experimental results showed good agreement. It is then possible to estimate the appropriate thickness of a target layer.

Table 2. 3. Calculated peak position and energy resolution of the pulse-height distribution which would be obtained from a proportional counter by observing Mn K or L X-rays emitted from ^{55}Fe.

Detector	X-rays to be observed	Peak position x_0 (eV)	Deviation from E^* (%)	Energy resolution
PR	$K_{\alpha 1}$, $K_{\alpha 2}$, $K_{\beta 1,3}$	5914	0. 31	19. 5%
PR	$L_{\alpha 1,2}$, $L_{\beta 1}$, $L_{\beta 3,4}$, L_{ι}, L_{η}	639. 9	0. 45	55. 2%

* E is the weighted mean energy of $K_{\alpha 1}$ and $K_{\alpha 2}$ for K X-rays and is the energy of $L_{\alpha 1,2}$ for L X-rays.

3. Proportional counters

Even with the development of solid state detectors, gas counters continue to be widely used in many applications. In the design and use of proportional counters, it is obviously important to have a general formula on the gas multiplication factor as a function of the counter geometry, applied voltage and gas pressure. Precise experimental and theoretical investigations on the gas multiplication factor are needed for cylindrical and rectangular cathode counters. Saturation and inordinate increasing phenomena of gas multiplication factor at high gas multiplication have also to be paid attention in the real usage of proportional counters. In addition to the description of gas multiplication, position-sensitive proportional counters specially designed are described.

3. 1. *Gas multiplication factor*

3. 1. 1. *Evaluation of gas multiplication formulas for coaxial counter*

Many works (3. 1-4) have been reported on gas multiplication formula which have been known to give considerably good agreement to the experiments carried out under relatively low gas pressure. Proportional counters with a cathode having a rectangular cross-section operated at high gas pressure have been recently applied to $4\pi\beta$-γ coincidence counting. Gas multiplication factors in coaxial counters under various conditions including high gas pressure were measured and gas multiplication formulas were evaluated (3. 5).

Experiments were carried out under the conditions that anode diameter ranged from 22 to 50 μm, cathode from 20 to 50 mm and counting gas pressure from 0. 1 to 1. 6 MPa for P-10 gas (90 % argon, 10 % methane) and from 0. 1 to 0. 5 MPa for methane. A charge sensitive preamplifier was used. Two amplifiers with different shaping times, 0. 5 μs and 3 μs, were used to check whether the pulse shape from the pulse generator was similar to that from the detector. An ^{55}Fe low energy X-ray source (3. 6) was used to find the relevant pulse heights and proportionality. Gas multiplication factor was obtained from the equation

$$G=VCW/(1.6\times10^{-19}E), \qquad (3.1)$$

where V is the output voltage from the pulse generator giving the same pulse height as the X-ray pulse height, C is the capacity of the test pulse input, W is 26 eV for P-10 gas and 28. 1 eV for methane and E is the energy of the X-rays.

Now we must reconsider the gas multiplication formulas. When λ is defined as a mean free path length for ionization, the Townsend coefficient α is theoretically obtained. However, elastic scattering and excitation by inelastic scattering actually occur where electrons travel in gas. It will be possible therefore to consider two kinds of λ for the Townsend coefficient expression

$$\alpha=(1/\lambda_1)\exp(-V_i/\lambda_2 E), \qquad (3.2)$$

where V_i is ionization energy and E is electric field. When $\lambda_1=\lambda_2$, the formula of Diethorn or Williams and Sara is led (3. 5).

$$\frac{\ln G}{Pr_aS_a}=k(\exp(-kV_i))(\ln S_a-\ln s_0), \qquad (3.3)$$

$$\frac{\ln G}{Pr_aS_a}=\frac{1}{V_i}\exp\left(-\frac{kV_i}{S_a}\right), \qquad (3.4)$$

where $S(=E/P)$ is electric field per unit gas pressure. Suffixes a and 0 mean the anode surface and the point where gas multiplication begins. In the formula of Zastawny $1/\lambda_1=kP(S-S_0)$ and $1/\lambda_2=k'PS$ and in that of Charles $1/\lambda_1=PJ$ and $1/\lambda_2$

$=HPS^{1/2}/V_i$, then

$$\begin{aligned}\frac{\ln G}{Pr_a S_a} &= k(\exp(-k'V_i))\left(\ln\ S_a+\frac{S_0}{S_a}\right)+C_z \\ &= k_z\left(\ln\ S_a+\frac{S_0}{S_a}\right)+C_z\end{aligned} \tag{3.5}$$

and

$$\frac{\ln G}{Pr_a S_a}=\frac{2J}{H^2}\left(\frac{H}{S_a^{1/2}}+1\right)\exp\left(\frac{-H}{S_a^{1/2}}\right)+C_c. \tag{3.6}$$

Our experimental results were examined to fit these formulas (3. 1-4). A linear relation on a graphical representation is obtained when an appropriate selection of both axis is done. However, for the experimental results obtained over a wide range of the pressure of the counting gas, all expressions showed no straight line for P-10 gas on the graphical expression and even for methane deviations from a straight line were recognized.

We must determine the constants to give the best fitting formula. However, the formula of Diethorn or Williams and Sara has no changeable constant. The formulas of Zastawny and Charles, on the other hand, have voluntary constants, the values of which given by them are, though, unsuitable. If the constants H and S_0 are selected properly, a linear relation can be obtained and an example (3. 5) is shown in Fig. 3. 1. Table 3. 1 shows the constants determined for both gases in the present experiments. The formula of Diethorn or Williams and Sara is applied only for the range of relatively low pressure, but the formulas of Zastawny and Charles can be applied for the wide range of pressure.

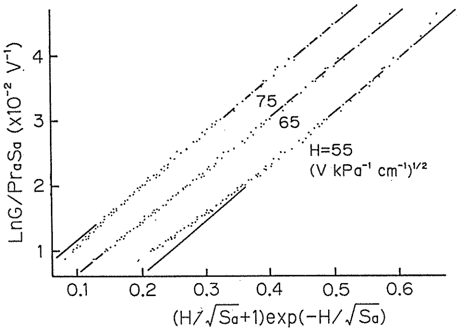

Fig. 3. 1. Charles plot for P-10 gas.

Table 3. 1. The constants of Zastawny and Charles formulas.

	P-10 gas	Methane
S_0[V kPa^{-1}cm^{-1}]	140 ± 10	200 ± 30
k_z[V^{-1}]	0.0252	0.0209
C_z[V^{-1}]	0.148	0.138
H[(V kPa^{-1}cm^{-1})$^{1/2}$]	65 ± 3	95 ± 5
J[cm kPa^{-1}]	170 ± 15	320 ± 25
C_c[V^{-1}]	1.7×10^{-3}	1.1×10^{-3}

3. 1. 2. Gas multiplication factor in rectangular counters

Recently, proportional counters with cathodes of rectangular cross sections (rectangular counters) have been used for $4\pi\beta$-γ coincidence counting at high gas pressure (3. 7). It is important to be able to estimate the gas multiplication factor by calculation for a rectangular counter operated at various pressures of the counting gas. Tomitani (3. 8) theoretically calculated the field strength of rectangular counter and multiwire counter and showed the conception of the cathode radius of

Table 3. 2. Dimensions of rectangular counters and the effective cathode radii of equivalent cylindrical counters.

Dimension of rectangular cross-section (mm)	Effective cathode radius (mm)
30×50	18.7
30×30	16.2
20×30	12.3

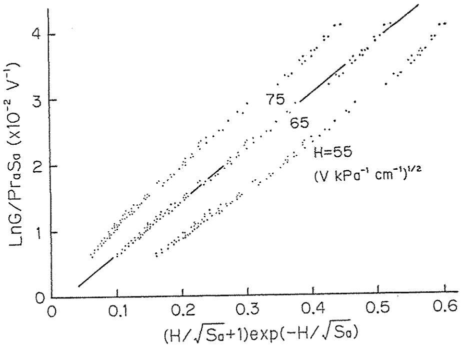

Fig. 3. 2. Charles plot obtained with rectangular counters for P-10 gas.

"equivalent cylindrical counter". Although the mathematical treatment is difficult, it was shown that the actual application was simple (3. 9).

In the following, it is shown that the gas multiplication factors obtained experimentally with rectangular counters agree well with the factors calculated for the equivalent cylindrical counters. In the calculation of the gas multiplication factors for the equivalent cylindrical counters, Charles (3. 3) and Zastawny (3. 4) formulas were used with the new constants obtained in section 3. 1. 1. Table 3. 2 shows the dimensions of rectangular counters and the effective cathode radii of the equivalent cylindrical counters. Fig. 3. 2 shows the gas multiplication factors for P-10 gas plotted according to the formula of Charles with various constants. Solid lines are the results obtained for cylindrical counters and fitted also to the results for rectangular counters. For the formula of Zastawny, the most linear relation was obtained for the same constants as in the coaxial counter. Also for methane, the similar results were obtained.

We could then show that the effective cathode radius calculated for a rectangular counter was a very useful measure in the calculation of gas multiplication factors of the counter.

3. 1. 3. *Effects of electron mean free path and ionization potential on gas multiplication*

Gas multiplication factor or gas gain G of cylindrical proportional counters can be expressed using the first Townsend coefficient α in the form

$$G=\exp\left(\int_a^c \alpha\, dr\right), \qquad (3.7)$$

where r is the distance from the axis of the counter, a is the anode radius and c is the starting position of gas multiplication. A theoretical expression for the coefficient α is deduced from the following classical argument (3. 10, 3. 11). Assuming λ_r to be the component of electron mean free path in the direction of the electric field, and λ_i to be the mean path length for an electron to travel in the field direction to ionize a gas molecule, we can express α as the mean number of free paths per unit length in the field direction multiplied by the chance of a free path longer than λ_i in the form

$$\alpha=(1/\lambda_r)\exp(-\lambda_i/\lambda_r). \qquad (3.8)$$

Since the electric field strength E can be regarded as a constant in the λ_i interval for cylindrical counter filled with a gas pressure of around 1 atm, λ_i is approximated using an effective ionization potential V_i by

$$\lambda_i = V_i/E. \tag{3.9}$$

Substituting Eq. (3.9) into Eq. (3.8) we obtain the relation

$$\alpha = (1/\lambda_r)\exp(-V_i/\lambda_r E). \tag{3.10}$$

3. 1. 4. Theoretical consideration on gas multiplication

If we consider a gas mixture to have a density N_j and a total cross section Q_j for electrons for the j-th component of the gas we obtain the relation

$$1/\lambda_r = h\sum_j N_j Q_j = hN\sum_j (N_j/N)Q_j = hNQ, \tag{3.11}$$

where $N=\sum_j N_j$ is the gas density, $Q=\sum_j (N_j/N)Q_j$ is the effective total cross section for electrons in the gas mixture and h is the inverse of the ratio of λ_r to the electron mean free path λ, i. e. $1/h=\lambda_r/\lambda$. The value h can be regarded as approximately constant taking a value of near unity. Substituting Eq. (3.11) into Eq. (3.10) we obtain

$$\alpha/N = (hQ)\exp(-hQV_i/S), \tag{3.12}$$

where $S=E/N$ is the ratio of the field strength to the gas density. If we assume the expression

$$Q = CS^m \tag{3.13}$$

to be a functional form for Q, C and m become in general constant depending only on the gas. Substituting Eq. (3.13) into Eq. (3.12) we obtain (3.12)

$$\alpha/N = KS^m\exp(-L/S^{1-m}), \tag{3.14}$$

where $K=hC$ and $L=hCV_i$ are constants characteristic of the gas. The value of m will be in the range of $0 \leq m \leq 1$ for the usual proportional counters.

When $0 \leq m < 1$ the logarithm of gas gain G is expressed using Eqs. (3.7) and (3.14) in the form

$$\frac{\ln G}{NaS_a} = \frac{1}{1-m}\,\frac{1}{V_i}\left[\exp(-LS_a^{m-1}) - \exp(-LS_c^{m-1})\right], \tag{3.15}$$

where S_a and S_c are the values of S at the anode and the starting position of gas multiplication, respectively. The second term in the braces of Eq. (3.15) can usually be neglected except when m is close to unity. Eq. (3.15) then reduces to the linear relation (3.12)

$$\ln(\ln G/NaS_a) = -LS_a^{m-1} - M, \tag{3.16}$$

where $M=\ln[(1-m)V_i]$. In the case of $m=1$, we can obtain directly from Eq. (3.14) the well-known formula of Diethorn (3.1)

$$\ln G/NaS_a = D(\ln S_a - \ln S_c), \tag{3.17}$$

where $D = hC\exp(-hCV_i)$ is the gas constant.

When $m=0$ Eq. (3.16) reduces to the formula by Williams and Sara (3.2), and when $m=1/2$ it reduces to a new formula

$$\ln(\ln G/NaS_a) = -L/\sqrt{S_a} - M. \tag{3.18}$$

Theoretical justification of Eq. (3.18) for Ar-CH_4 mixtures was confirmed from the data of total cross section for electrons in these gases and the characteristic energy of electrons in an electric field.

3. 2. Saturation and inordinate increase of gas multiplication factor

3. 2. 1. Gas multiplication for low energy X-rays

In the measurement of radiation with a proportional counter, gas multiplication factor depends on the radiation energy at large gas multiplication and hence the energy linearity is lost (3.12-13), which is called the saturation of gas multiplication factor and had not been well understood. In this section, the experimental and theoretical works (3.14-15) for the dependence of the saturation on the anode diameter and gas pressure are described.

Fig. 3. 3 shows gas multiplication factor against applied voltage for counters with a cathode radius of 14.6 mm and various anode radii operating at the atmospheric pressure of methane counting gas. The gas multiplication factor depends on the X-ray energy at large gas multiplication and the deviation from the energy linearity increases with X-ray energy. This tendency increases with decreasing anode diameter. Full lines show theoretically calculated values for Mn L, Al K and Mn KX-rays. The saturation of gas multiplication factor was also confirmed experimentally to be prominent at high gas pressure (3.15).

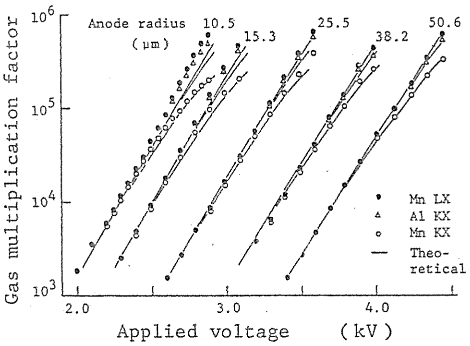

Fig. 3. 3. Gas multiplication factor vs. applied voltage.

The following is a theoretical calculation of the saturation. A photoelectron and subsequent Auger electrons liberated by an X-photon create primary ion pairs with a spatial length in the counting gas. Electrons in the primary ion pairs drift toward the anode wire like "a primary electron train". Townsend first ionization coefficient α and gas multiplication factor G are given by Eqs. (3.2) and (3.7), respectively. The preceding electrons in an electron train leave behind a large number of positive ions at the gas multiplication region and consequently the electric field strength $E(R)$ of the region is reduced for the succeeding electrons in the train, where R is the distance from the anode axis. The field strength $E(R, \Delta t)$ at R and at the time Δt after the arrival of the preceding electrons is expressed (3.15) by the following equation

$$E(R,\ \Delta t) = E_0(R) + \frac{1}{2\pi\epsilon_0 R\ln(b/a)}$$

$$\times\left\{\int_a^R \phi(r+v_+\Delta t,\ \Delta t)\ln\left(\frac{r}{a}\right)\mathrm{d}r \right. \tag{3.19}$$

$$\left. -\int_R^b \phi(r+v_+\Delta t,\ \Delta t)\ln\left(\frac{b}{r}\right)\mathrm{d}r\right\}.$$

where $E_0(R)$ is the electric field strength without space charge, $\phi(r+v_+\Delta t,\ \Delta t)$ is the equivalent space charge which was produced by the preceding electrons at a distance r and $\Delta t=0$ and drifted by $v_+\Delta t$ toward the cathode after a time delay Δt. The angle θ and the length L define the small area where the gas multiplication takes place and was estimated by the penetration range (3.16) of primary photoelectrons and by the diffusion (3.17) of electrons in the train. $v_+(=2\times10^3 E/P$ for CH_4^+(3.18)) is the drift velocity of positive ions. Combining Eqs. (3.19), (3.2) and (3.7), we can calculate gas multiplication factors under the presence of the effect of the positive ions called "self-induced space charge" and the results are shown in Fig. 3. 3 by full lines. The ratio $E(R,\ \Delta t)/E_0(R)$ is larger for larger radius of the anode wire and also for higher pressure (3.15) of the counting gas. The saturation of gas multiplication factor can be thus explained and we can estimate the saturation depending on the counter geometry, gas pressure and applied voltage.

3. 2. 2. *Gas multiplication for α-particles*

It is qualitatively known that when the track of α-particles is normal to the anode wire the multiplication factor is generally smaller than that in other directions (3.19). In this section, the dependence of the multiplication factor for α-particles on the incident angle and a phenomenon of inordinate increase of the factor at a higher applied voltage are described (3.20). After our work, Koori (3.21) investigated this phenomenon as a self-quenching streamer (SQS) transition.

The counter used was a coaxial type with a cathode diameter of 42 mm and with methane gas flow under the atmospheric pressure. Anodes with various diameters were used. Collimated α-particles from ^{241}Am were injected into the counter through a window of about 15μg/cm^2 with various incident angles θ from the normal to the counter axis. Fig. 3. 4 shows the change of the gas multiplication factor of the proportional counter against the applied voltage for α-particles together with those for Mn LX, Al KX and Mn KX-rays. At the applied voltage of about 3.3 kV, the gas multiplication factor in the direction $\theta=0°$ inordinately increases and jumps by about 20 times (3.20). The applied voltage where the jump occurs at $\theta=0°$ depends on the anode diameter as shown in Fig. 3. 5 (a). The ratio of the multiplication factor, just before and after the jump, depends on the diameter as shown in Fig. 3. 5 (b). Such

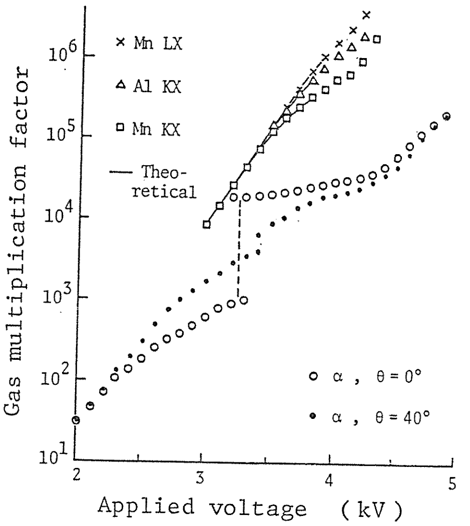

Fig. 3. 4. Inordinate increase of gas multiplication factor.

an inordinate increase was also found in P-10 gas and may be attributed to the following. In an electron train produced by an α-particle, the gas multiplication factor for the preceding electrons in the train will be large at comparatively high applied voltage and accordingly a large number of positive ions will be left in the gas multiplication region near the anode wire. The strength of the electric field between the positive ions and the anode wire will then become smaller than that without the positive ions as mentioned in section 3. 2. 1. On the contrary, the electric field strength in the region between the positive ions and the cathode will become larger than that without the ions (3.20), and consequently the gas multiplication factor in this region for the succeeding electrons in the electron train becomes larger than that for the preceding electrons. Such an increase will also be expected for the next succession of electrons in the same electron train and thus self-breeding of gas multiplication which will result in the inordinate increase or the jump of the gas multiplication factor is expected.

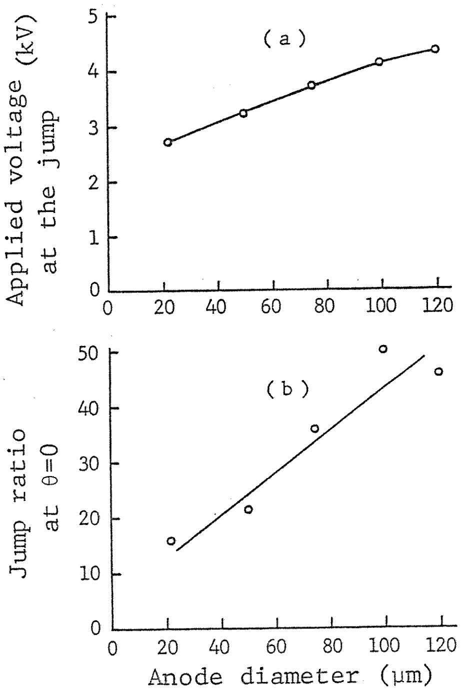

Fig. 3. 5. (a) The applied voltage at which the jump occurs and (b) the jump ratio.

It may be possible to use the inordinate increase of gas multiplication factor for the selective detection of radiations with specific incident angle or specified ionization density and for the discrimination of the background radiations.

3. 2. 3. Gas multiplication for ^3H β-rays

The maximum range of ^{3}H β-rays in methane is less than 1cm under normal temperature and pressure. We found that (3.22) there were a directional effect on the saturation and the inordinate increasing phenomena of gas multiplication even for ^{3}H β-rays with such a short range. A charge division type position sensitive proportional counter with a resistive anode (a radius of 11 μm) was used in this observation.

Fig. 3. 6 shows the pulse height distribution of ^{3}H β-rays in methane at applied voltage of 2.17 and 3.0 kV. The window of a pulse height selector (PHS) was set at (a), (b), (c) or (d) and the signals passed through the window were used as gating signals for the observation of position spectra. From Fig. 3. 3, it can be seen that the saturation of gas multiplication factor does not occur at 2.17 kV, but it does at 3.0 kV for the anode radius around 10~15 μm. A charge division type position-sensitive proportional counter with a resistive anode wire was used for obtaining position information as shown in Fig. 3. 7 (a). Tracks (b) of β-rays emitted from a point source contain primary ion pairs along the track proportional to dE/dx as shown in (c) and position spectrum (d) will be obtained depending on

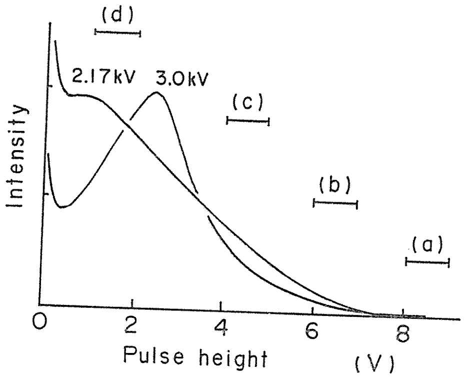

Fig. 3. 6. Pulse height distributions of ^{3}H β-rays.

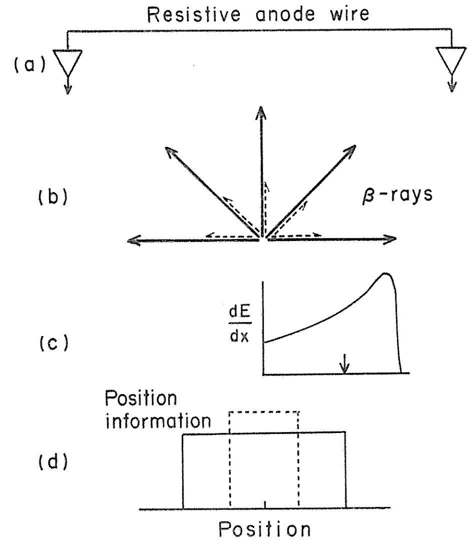

Fig. 3. 7. Explanatory figure for obtaining position information.

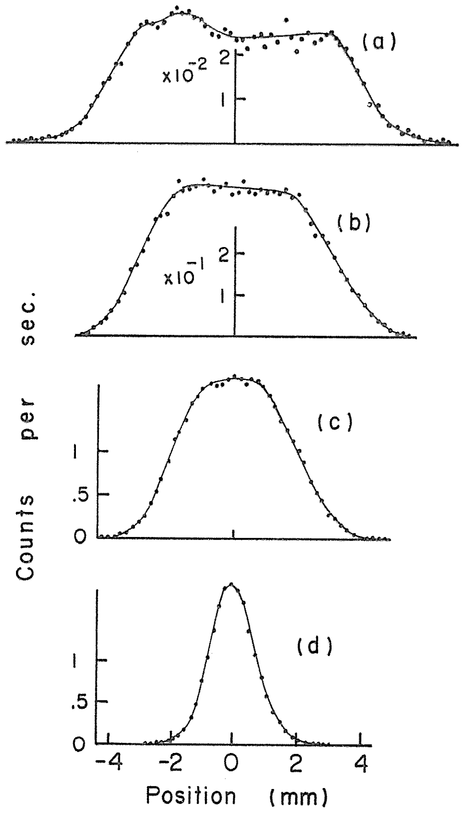

Fig. 3. 8. Position spectra of ^{3}H β-rays in methane at 2.17 kV.

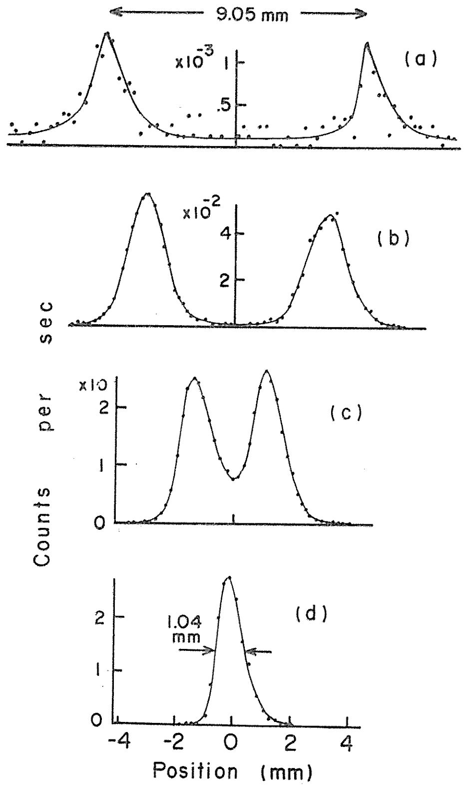

Fig. 3. 9. Position spectra in methane at 3.0 kV.

the β-ray energy, low energy (broken line) and high energy (full line). Fig. 3. 8 shows position spectra (a), (b), (c) and (d) at 2. 17 kV in methane for ^{3}H β-rays whose pulse heights fell in each channel (a), (b), (c) and (d) of the PHS, respectively, shown in Fig. 3. 6. The spectra are same as Fig. 3. 7 (d) as expected, since there is no saturation of gas multiplication factor and the pulse height is proportional to β-ray energy. Fig. 3. 9 shows the position spectra obtained at 3. 0 kV. In the large pulse height channels (a) and (b), no position signal can be observed at the position of the ^{3}H point source, which means that β-rays emitted from a point source normal to the anode wire suffer the saturation effect of gas multiplication mentioned in section 3. 2. 1. On the contrary, β-rays emitted parallel with the anode wire do not suffer the saturation effect and appear in the large pulse height channels (a) and (b). The distance between the peaks, 9. 05 mm, in (a) agrees with the calculated distance $2L_g$, where L_g is the distance between the position of the β-ray point source and the center of gravity of the primary ion pairs produced by a β-ray with the maximum energy of 18. 6 keV. The meaning of $2L_g$ is therefore the distance of the position signals of β-rays emitted in opposite direction each other and parallel with the anode wire. The calculation was done as follows.

The specific energy loss can be expressed as $\mathrm{d}E/\mathrm{d}x = -b/(a+E)$. The range R is, then,

$$R = \int_{E_0}^{0} \left(\frac{\mathrm{d}E}{dx}\right)^{-1} \mathrm{d}E = \frac{E_0}{b}\left(a + \frac{E_0}{2}\right). \tag{3. 20}$$

Since the ranges R_A and R_B for two different energies E_{0A} and E_{0B} can be obtained from literature (3. 23) for a particular element, the constants a and b can be determined. For a matter composed of two elements, $\mathrm{d}E/\mathrm{d}x$ can be obtained by a linear combination of those of two elements weighted by the weight contents. Then R and L_g are obtained as

$$R = k\left[E_0\left(\alpha - \beta - \frac{E_0}{2}\right) + \{\alpha(\alpha-\beta)+\gamma\}\ln\frac{\alpha}{E_0+\alpha}\right],$$

where

$$k = -(b_1c_1+b_2c_2)^{-1},\ \alpha = -k(a_1b_2c_2+a_2b_1c_1), \tag{3. 21}$$

$$\beta = a_1+a_2,\ \gamma = a_1a_2.$$

$$L_g = k\left[E_0\left\{\frac{E_0}{3} - \frac{1}{2}(\alpha-\beta)\right\} + \frac{\alpha\{\alpha(\alpha-\beta)+\gamma\}}{E_0}\ln\frac{\alpha}{E_0+\alpha}\right]. \tag{3. 22}$$

In the counting gas of isobutane, β-rays emitted perpendicularly to the anode wire caused inordinate increase of the gas multiplication factor as observed for α-particles. The reason why isobutane causes the inordinate increase is not clear. It may be attributed to the large molecular weight which results in a small mobility of ions produced by the preceding electrons as described in section 3. 2. 2 and hence a strong electric field at the gas multiplication region between the ions and the cathode is formed (3. 20).

3. 3. *Position-sensitive proportional counter (PSPC)*

3. 3. 1. *Charge division type PSPC with low resistive anode wire*

A charge division type with a resistive anode wire was adopted as a PSPC (3. 24), since this type is very simple and suitable for internal gas counting. Relative position resolution ($\Delta x/x$) at a position x in the charge division type is expressed by $(\Delta x/x)=k/(QR^{1/2})$ (3. 25), where k is a constant, Q is the total input charge on the anode wire and R is a total resistance of the anode wire. The position resolution is improved with the increase of the resistance R. Thin anode wires with a large resistance, for instance 1 kΩ/mm, and with a diameter of a few tens micrometers are rather difficult to obtain except for carbon coated quartz filament (Technology for Nuclear Corporation, U. S. A.) which is extremely expensive. We used therefore ordinary metal alloy wires such as stainless-steel or nickel-chromium with a diameter of about 20 μm, which had low resistance of about 10 Ω/cm. When the resistance is low, the input impedance of preamplifier should be low. As shown in Fig. 3. 10, the coupling capacitor C_c to take out the signal from the anode is put inside the feedback loop of a charge sensitive preamplifier, the input impedance Z_i can be substantially reduced to $(j2\pi f(1+A)C_f)^{-1}$. For example, when $f=1$ MHz, $A=1000$ and $C_f=10$ pF, Z_i equals 16Ω. A tiny capacitor for high voltage use with a capacity of more than 2×10^3pF is not commercially available. If the capacitor C_c with 2×10^3pF is used outside the feedback loop, Z_i is more than 80 Ω which corresponds to an anode length of about 8 cm.

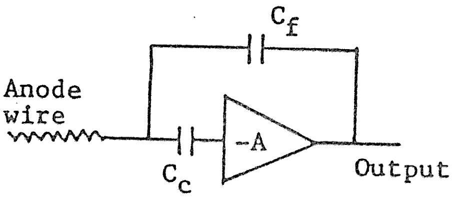

Fig. 3. 10. Preamplifier configuration.

An advantage to use a low resistive anode wire is a short propagation time of signals through the wire. A charge Q induced on a resistive anode wire at a position x which is the distance from the left end diffuses toward the left and the right ends resulting the charges Q_L and Q_R at a time t (3. 26),

$$Q_L(x,\ t)=(2Q_0/\pi)\sum_{n=1}^{\infty}n^{-1}\sin\{(n\pi/y)x\}[1-\exp\{n^2\pi^2t/(rcy^2)\}], \qquad (3.23)$$

$$Q_R(x,\ t)=(-2Q_0/\pi)\sum_{n=1}^{\infty}n^{-1}\sin\{(n\pi/y)x\}\cos(n\pi)[1-\exp\{-n^2\pi^2t/(rcy^2)\}], \qquad (3.24)$$

where y is the length of the anode wire, r is the resistance per unit length of the anode wire, and c is the capacity per unit length of the counter. Now the time t_d is defined that the division of the charge Q induced at the center is completed by the time t_d in the error of 0. 01 % for the ideal division at the infinite time t_d can be calculated by Eqs. (3. 23) and (3. 24). Then the relation between the t_d and the resistance per unit length is given in Fig. 3. 11 under the condition that the diameters of the anode and the cathode are 22 μm and 44 mm, respectively, and the length of the counter is 40 cm. A linear amplifier with a short time constant for pulse shaping less than 1μsec is usable for low resistive anode wires.

For the counter mentioned above, a few microseconds are substantially infinite for t. The charge Q_L and Q_R are therefore reduced to $Q_L(x)=Q_0(y-x)/y$, $Q_R(x)=Q_0x/y$. The position x can be determined by the following operation

$$Q_R/(Q_L+Q_R)=x/y. \qquad (3.25)$$

To obtain a good linearity for position determination, the operation characteristics including preamplifiers and linear amplifiers at both left and right sides must be same.

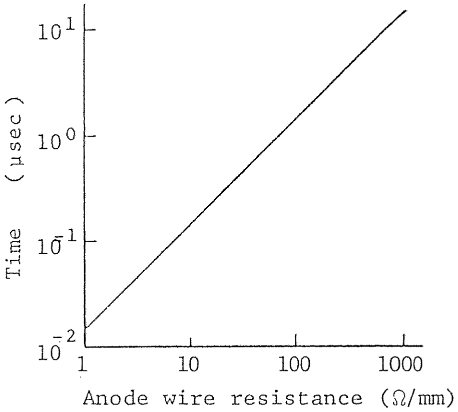

Fig. 3. 11. Signal propagation time vs. anode wire resistance.

3. 3. 2. Charge division type PSPC with carbon fiber anode wire

A resistive anode wire with an appropriate resistance is difficult to obtain as mentioned in section 3. 3. 1. We newly tried to apply commercially available carbon fibers (3. 27), which have been widely used as structural material, to an anode wire for a charge division type PSPC. The properties of commercially available carbon fibers are confined to 7μm in diameter and about $1.5\times10^{-3}\,\Omega$cm in specific resistance.

Since about 3000 fibers are weakly sticked together in a bundle with a kind of adhesives, the bundle was immersed in acetone to dissolve the adhesives. The bundle was then dried and each fiber could be taken out one by one in a length of, for instance, 1 m or so. Fig. 3. 12 shows microscopic photographs of carbon fibers (a) and (b) produced by different manufacturers. Although the surface is not so smooth compared with a stainless steel wire (c), there was no trouble for the usage as an anode wire.

The uniformity of the resistance along a fiber was examined by observing the position signals for collimated Mn KX-rays which were injected at various positions through the counter window. The

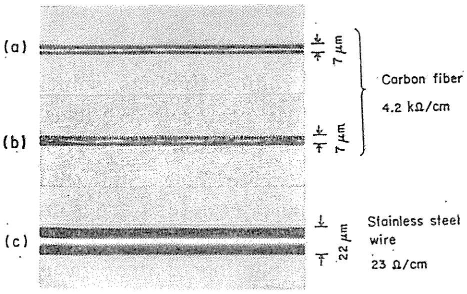

Fig. 3. 12. Microscopic photograghs of carbon fibers.

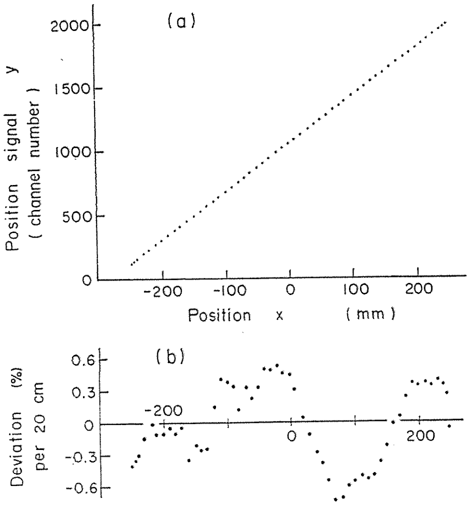

Fig. 3. 13. Linearity of position signal.

linearity of position signals is shown in Fig. 3. 13 (a) and (b). The deviation (b) per 20cm from a strict linear relation was 0. 34 % which was smaller than 0. 5 % for a carbon coated quartz filament commercially available. Position resolution as a function of the number of input electrons to the anode wire is shown in Fig. 3. 14 (a) together with energy linearity (b). The minimum position resolution (a) was 0. 42 mm which was limited by the penetration range of photoelectrons liberated by Mn KX-rays in the counting gas (Ar 50 %, CH_4 50 %). The energy linearity (b) was simply checked by taking the ratio of Ar KX-ray escape peak to the full energy peak of Mn KX-rays against the number of input electrons on the anode wire. A faster rise of the solid line for carbon fiber indicates the appearance of the saturation of gas multiplication factor for Mn KX-rays at smaller number of input electrons on the anode compared with that for carbon coated quartz filament shown by a broken line. Gas multiplication suffers a larger effect of space charge near the anode wire with a smaller diameter especially for higher energy X-rays as mentioned in section 3. 2. 1 and hence the energy linearity is lost. In position sensitive detectors, however, a strict energy linearity is seldom required and the loss of energy linearity may even be favourable in a special case such as ^{3}H counting (3. 24). Carbon fibers can be used as a new resistive anode wire for charge division type proportional counter.

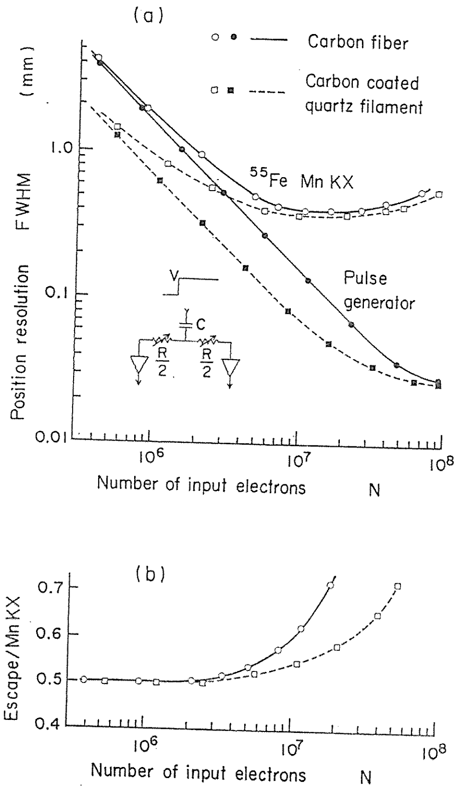

Fig. 3. 14. (a) Position resolution, (b) energy linearity.

4. Standardisation of radioactivity

We use radioisotopes of various physical forms, namely radioactive gas, solution and solid, and the standardisation of these sources is frequently required. We usually make solid sources with accurate activities from radioactive solution with known radioactivity concentration. Therefore, standardisation of gaseous and liquid radioisotopes is important. Radioactive solutions of pure α and β emitters are sometimes standardised by direct counting of solution, but in the most cases a solid source is made from one drop of solution and counted. Weighing of drop by extrapolation method or pycnometer difference weight method shows accuracy of more than 0. 1 percent, then the standardisation of the solid source requires that better than 0.1 percent. This chapter deals with standardisation of solid sources and gaseous sources.

4. 1. Standardisation of solid source

Standardisation of solid sources is made by a direct or a coincidence counting method. The former method is relatively simple in procedure, but contains some uncertain corrections. The standardisation by the latter method is carried out more accurately even though the presence of uncertain physical parameters of decay scheme. We mainly treat in this section a $4\pi\beta$-γ coincidence method which is the most important coincidence technique and requires only a small correction.

When the nuclide with simple decay is measured by the $4\pi\beta$-γ coincidence counting,

$$n_\beta = n_0\{\varepsilon_\beta + (1-\varepsilon_\beta)(\varepsilon_{\beta\gamma} + \alpha\varepsilon_{ce})/(1+\alpha)\} \tag{4.1}$$

$$n_\gamma = n_0\varepsilon_\gamma/(1+\alpha) \tag{4.2}$$

$$n_c = n_0\varepsilon_\beta\varepsilon_\gamma/(1+\alpha), \tag{4.3}$$

where n_β, n_γ, n_c: β, γ and coincidence count rates, n_0: disintegration rate, ε_β, ε_γ: counting efficiencies of β and γ detectors, α: total internal conversion coefficient, $\varepsilon_{\beta\gamma}$, ε_{ce}: counting efficiencies of the β counter for γ-rays and internal conversion electrons (4.1-4). An efficiency function then becomes

$$\frac{n_\beta \cdot n_\gamma}{n_c} = n_0\left\{1 + \frac{1-\varepsilon_\beta}{\varepsilon_\beta}\psi\right\},\quad \psi = \frac{\varepsilon_{\beta\gamma} + \alpha\varepsilon_{ce}}{1+\alpha}. \tag{4.4}$$

In this expression $n_\beta \cdot n_\gamma / n_c$ at $(1-\varepsilon_\beta)/\varepsilon_\beta = 0$ yields the true disintegration rate n_0. If the ψ is constant, the right-hand term of Eq. (4.4) can be approximated in a linear function of $(1-\varepsilon_\beta)/\varepsilon_\beta$. For the nuclide with many β branches Eq. (4.4) is

$$\frac{n_\beta \cdot n_\gamma}{n_c} = n_0\left\{1 + \frac{1-\varepsilon_\beta}{\varepsilon_\beta}(1-\phi)\right\}, \tag{4.5}$$

$$\phi = \sum P_k C_k (1-\psi_k),\quad C_k = (1-\varepsilon_{\beta k})/(1-\varepsilon_\beta),$$

where P_k: emission probability of k th β branch and suffix k means the k th branch.

Correction formulas for dead times and resolving time are proposed from many authors (4.2, 5-9), but for a counting result of source with low disintegration rate (<10 kBq) the following Campion's formula (4.2) corrected for the Gandy effect (4.5) is valid within enough accuracy.

$$\frac{n_\beta \cdot n_\gamma}{n_c} = \frac{N_\beta N_\gamma\{1-\tau_r(N'_\beta + N'_\gamma) + \tau_d(N'_\beta - N'_\gamma)\}}{N_c - 2\tau_r N'_\beta N'_\gamma} \cdot \frac{(1-\tau_\beta N'_\beta - \tau_\gamma N'_\gamma + \tau N'_c)}{(1-\tau_\beta N'_\beta)(1-\tau_\gamma N'_\gamma)}, \tag{4.6}$$

where N'_β, N'_γ, N'_c: observed β, γ and coincidence count rates including background, N_β, N_γ, N_c: β, γ and coincidence count rates corrected for background, τ_r: resolving time, τ_β, τ_γ: β and γ dead times, τ_d: delay time of β pulse and τ: shorter value of τ_β or τ_γ. It is, however, required for the result of high count rates to use Smith's equation (4. 9) by using the mathematical theory of Cox and Isham (4. 10).

4. 1. 1. Various system for coincidence counting

4. 1. 1. 1. Ordinary $4\pi\beta$-γ coincidence system

The detector part of $4\pi\beta$-γ coincidence system was constructed in the shielding box which caused little distortion of the γ-ray spectrum shown in a previous report (4. 11). The box had the inner size of 400×400×785 mm and the thickness of the wall was 100 mm of lead. The counting system consisted of two 76×76 ϕ mm NaI (Tl) scintillators and a $4\pi\beta$ counter placed between them. The $4\pi\beta$ counter was constructed with two $2\pi\beta$ counters composed of aluminum whose effective inner volume was 50×50×30 mm. The anodes were platinum wires with a diameter of 50 μm ($4\pi\beta$(pc)-γ coincidence system). The block diagram of the counting system is shown in Fig. 4. 1.

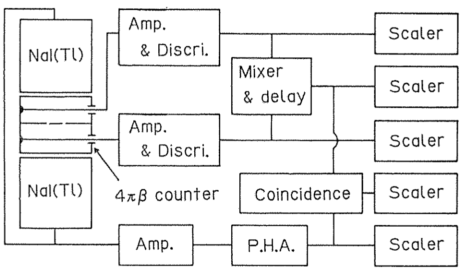

Fig. 4. 1. Block diagram of the counting system.

When in the γ-ray spectrum the discrimination level was set at 78 keV, the background count rate in the shielding box decreased from 425 to 4. 05 cps. Though the peaks of RaC, ThC″ and ^{40}K are recognized on the spectrum measured out of the box, in the shielding box only the peak of ^{40}K is clearly observed. The length of the plateau region of the $4\pi\beta$ counter was over 400 V with a slope of 1. 0% per 100 V for the ^{60}Co source in methane, and 300 V with a slope of 4. 6% per 100 V for ^{54}Mn source in 90% argon plus 10% methane mixture (P-10 gas). The relative time distribution of pulses in two channels showed that the spectrum of the ^{60}Co source with use of methane had 122 ns of FWHM and 667 ns of FWTM and ^{54}Mn source in P-10 gas had 52 ns and 810 ns of each.

4. 1. 1. 2. X-γ coincidence system

The absolute disintegration rate of sources of radioisotopes that decay by electron capture is determined by the X-γ coincidence counting method. The counting system consisted of an X-ray and a γ-ray detector, two single channel pulse height analysers, a fast-slow coincidence circuit and three scalers (4. 12). The detectors were NaI(Tl) scintillators; the one for the γ-rays was 51×44 ϕmm and the other for X-rays was 2 mm thick to minimize the background effect caused by energetic γ-rays, this effect being measured by inserting a copper plate of 0. 5 mm thick as an X-ray filter between the detector and the source.

A low noise preamplifier with a gain of 25 was used to amplify output signals from the X-ray detector. The X-rays and the γ-rays, which are to be coincided, were selected by the respective pulse height analysers. The resolving times of the fast and slow coincidence circuits were about 2 and 6 μs respectively. The operation of the system was examined by the absolute measurement of disintegration rate of a ^{88}Y source, the characteristic X-rays and the 1. 83 MeV γ-rays emitted from ^{88}Y are coincided. The absolute disintegration rate of the source was also measured by the γ-ray spectrometrical method with a $76\times76\,\phi$mm NaI(Tl) scintillator and a multichannel pulse height analyser. The photopeak efficiency of this spectrometer was determined by the use of ^{137}Cs, ^{60}Co and ^{24}Na sources, and the absolute disintegration rates were determined in advance by the $4\pi\beta$ counting or $4\pi\beta$-γ coincidence counting. The disintegration rates of ^{88}Y sources obtained by the X-γ coincidence method were in good agreement with those by the γ-ray spectrometrical method.

4. 1. 1. 3. $4\pi\beta$-γ coincidence system using a thin $4\pi\beta$ counter operated by negative high voltage

The shielding box described in sect. 4. 1. 1. 1 was effective for decrease of γ background and indicated no distortion of spectrum, but it was very expensive. To miniaturize the shield one needs to use a single scintillator, to bring a source close to that and to make a compact $4\pi\beta$ counter and preamplifier. Actually, the $4\pi\beta$ counters used in international comparison of ^{139}Ce usually had a half height of 20 to 30 mm (4. 13), but a thin multiwire proportional counter constructed for the reduction of the resolving time by Plch et al. showed good characteristics (4. 14). In consideration of these points, a thin $4\pi\beta$ counter with multiwires was constructed (4. 15).

The sectional plane of the constructed counter is shown in Fig. 4. 2. Each half had a volume of $70\times60\times11$ mm and five platinum wires with diameter of 30 μm that were arranged at intervals of 12 mm. Negative high voltage was supplied to the gold deposited inner wall of polymethyl metacrylate to leave coupling condensers. A $76\times76\,\phi$mm NaI(Tl) scintillator was positioned under the new counter. The output signals from each channel were led to each scaler and to a coincidence circuit.

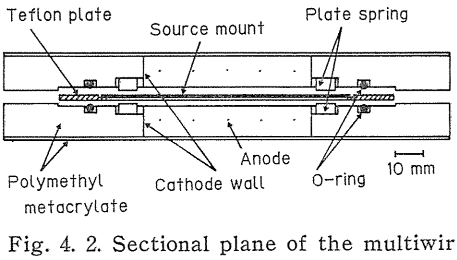

Fig. 4. 2. Sectional plane of the multiwire $4\pi\beta$ counter.

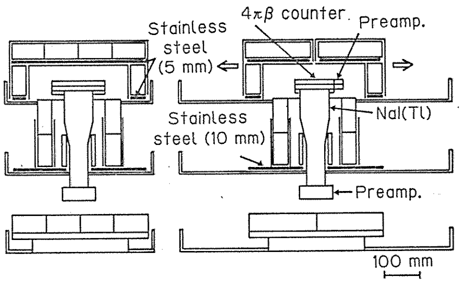

Fig. 4. 3. Diagram of the compact shielding system.

The detector part was put in the shielding system composed of three parts as shown in Fig. 4. 3. The distortion of γ-ray spectrum mainly depended on the $4\pi\beta$ counter, then the amount by this shield was smaller than by that described in sect. 4. 1. 1. 1. The count rate of γ background from 60 keV to 2. 8 MeV in the shield (50 mm lead) was decreased by about a factor 23, though that in the previous shield (100 mm lead) was decreased by about a factor 48. The γ-ray detection efficiency by the system coincided almost with the one by the previous system with two scintillators (4. 16).

The centre anode gave the β signals and the others were used only for cleaning excess charges, considering various experimental results (4.17–18). The plateau curve showed slopes of about 0.1 % per 100 V in methane gas and of 5.4 % per 100 V in P-10 gas. The relative time distribution of pulses in two channels showed 43 ns of FWHM and 105 ns of FWTM in methane gas, and 19 ns and 233 ns of each in P-10 gas.

4. 1. 1. 4. $4\pi\beta$-γ coincidence system using a multi source $4\pi\beta$ counter

A multi source $4\pi\beta$ counter was constructed in order to measure simultaneously up to five sources for several objects. Fig. 4. 4 shows a half of the counter with a height of 11 mm. Five anodes of stainless steel wires with a diameter of 30 μm were held at earth potential, and other wires with the same diameter held at earth potential were positioned at both sides of each anode for the limitation of the charge collection region. A 51×127 ϕmm scintillator was positioned under the $4\pi\beta$ counter. Measurements were carried out by using an electronic system similar to the ordinary coincidence system permitting of two independent γ channel gates.

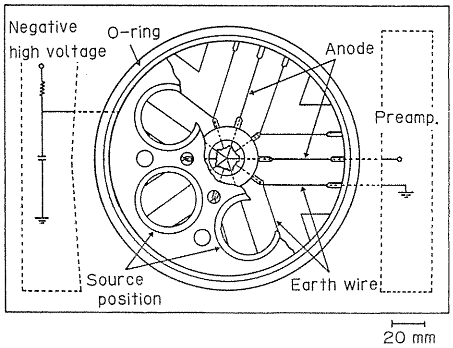

Fig. 4. 4. Sketch of the multi source $4\pi\beta$ counter.

When plural sources are simultaneously measured with this $4\pi\beta$-γ coincidence apparatus ($4\pi\beta$(MS)-γ coincidence system), the following equation is basically obtained:

$$\frac{n_\beta \cdot n_\gamma}{n_c}=\frac{\sum n_i\varepsilon_{\gamma i}\cdot\sum n_i\{\varepsilon_{\beta i}+(1-\varepsilon_{\beta i})\psi\}}{\sum n_i\varepsilon_{\beta i}\varepsilon_{\gamma i}}. \tag{4.7}$$

The notations have been given in the beginning of this chapter, and suffix i means the i th source. Here, $\varepsilon_{\beta\gamma}$ and ε_{ce} hardly depend upon the source position; therefore, ψ is treated as a constant.

Each source position was geometrically equivalent in regard to the γ detector, then it is fundamentally easy to keep $\varepsilon_{\gamma i}$ constant and Eq. (4.7) can be written as:

$$\frac{n_\beta \cdot n_\gamma}{n_c}=\frac{\sum n_i\cdot\sum n_i\{\varepsilon_{\beta i}+(1-\varepsilon_{\beta i})\psi\}}{\sum n_i\varepsilon_{\beta i}}. \tag{4.8}$$

Considering that $\sum n_i=n_0$ and $\sum n_i\varepsilon_{\beta i}/\sum n_i=\varepsilon_\beta$, Eq. (4.8) can be performed into

$$\frac{n_\beta \cdot n_\gamma}{n_c}=n_0\left\{1+\frac{1-\varepsilon_\beta}{\varepsilon_\beta}\psi\right\}. \tag{4.9}$$

The γ-ray detection efficiency obtained at each source position showed no system-

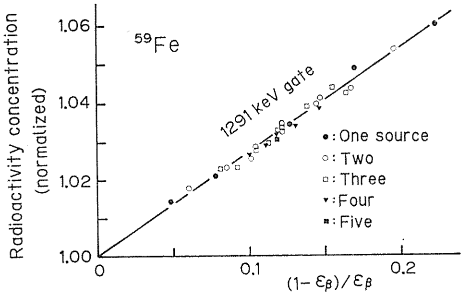

Fig. 4. 5. Efficiency function obtained from the measurements in all the combination.

atic deviation (4.19); Therefore the coincidence equation can be treated in the same way as that for one source measurement.

Fig. 4.5 shows the efficiency function of ^{59}Fe which was obtained from the measurements in all the combination of the five sources. It showed the appropriate efficiency function as a whole.

4. 1. 1. 5. $4\pi\beta$-γ coincidence system using a pressurized $4\pi\beta$ counter

When the efficiency function can be obtained from the measurements by change of the discrimination level of β channel, the proportional counter should be operated at elevated pressures. A $4\pi\beta$ counter was constructed with two $2\pi\beta$ counters composed of brass whose sensitive volume was 40×40×20 mm. The wall thickness was 5 mm to withstand pressures up to 5 MPa of P-10 gas, and the anodes were stainless steel wires with diameter of 22 μm. A 76×76 ϕmm NaI(Tl) scintillator was placed under the pressurized counter. Continuous measurements could be carried out in different detection efficiencies by change of the discrimination level or supplied voltages which were controlled by computer ($4\pi\beta$(ppc)-γ coincidence system).

A gas pressure control system is shown schematically in Fig. 4.6 which is the similar one by Baerg et al. (4.20). A differential pressure switch detected the pressure difference between the counter and reference volume, opening a magnetic valve MV1 till recovering the setting pressure. The variation of pressure in the counter was absolutely 2.8 kPa, but it gave no detectable effect (4.21).

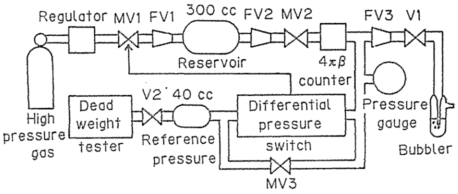

Fig. 4.6. Gas pressure control system. MV: magnetic valve, FV: fine metering valve and V: stop valve.

4. 1. 2. Optimisation of experimental condition and efficiency function

4. 1. 2. 1. Electrical conductivity of source backing film

Minimizing the self absorption of the source itself and the absorption of the source mount are essential factors to shorten the extrapolation range in the efficiency function. The former will be described in the sect. 4. 1. 3. As the latter, a VYNS film that has a strong toughness has been frequently used to reduce the absorption in the source mount, and the electrical conductivity of the film mostly given by the vacuum deposition of gold or gold-20% palladium (4.22-23). The small absorption in film requires the thin thickness of metal, but the extremely thin thickness shows the counting loss due to insufficient conductivity. Thus a metal film with moderate thickness is required for minimum counting loss.

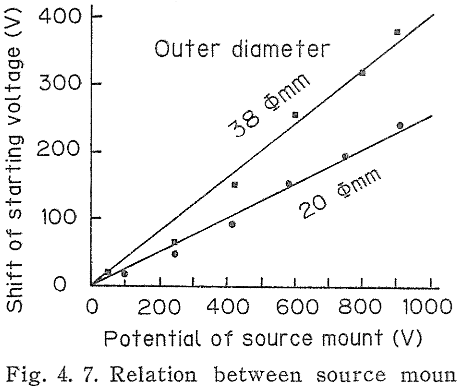

Fig. 4.7. Relation between source mount potential and voltage shift of plateau region.

The effect of charge up due to insufficient conductivity was examined by using the counter described in sect. 4. 1. 1. 1 (4. 24). The relation between the film potential and the shift of starting voltage of plateau region is shown in Fig. 4. 7. The calculated shift of starting voltage considerably agreed with the experimental. To give no effect for plateau region the source of about 2 kBq was desired that the resistance between film surface and cathode was smaller than 10^{10} Ω.

Electric resistances of gold deposited VYNS films were measured (4. 25) and roughly agreed with those by Colas et al. (4. 23) and were considerably smaller than those by Lowenthal et al. (4. 22). The resistance between the source and the catode is nearly the same order as the value in unit of Ω sq^{-1}, then the resistance of 10^{10} Ω means 2 μg cm^{-2} of gold. The resistance was increased or decreased with time lapse for the case of thickness thinner or thicker than 15 μg cm^{-2}, respectively.

A source was prepared on the surface of the mount where gold was deposited with appropriate thickness (front surface), then this source was repeatedly measured after deposition of gold on the other surface (back surface). The β-ray detection efficiency is shown in Fig. 4. 8 as a function of the thickness of gold on the back surface. The efficiency is maximum at gold thickness of about 2 μg cm^{-2}, and the improvement of the efficiency was defined as shown. To examine the effect of gold thickness on the front surface, the procedures were repeated using more than twenty sources with various gold thickness on the front surface. The effect of gold on the back surface was recognized up to the thickness about 10 μg cm^{-2} and the improvement of efficiency was mostly constant. These results were the same for a ring with larger diameter and also in the case of other nuclides.

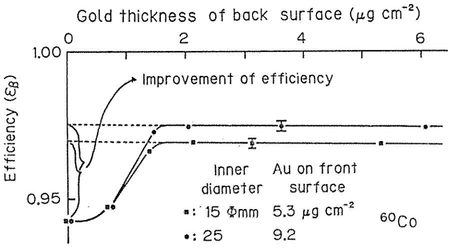

Fig. 4. 8. Detection efficiencies for various mean thicknesses of gold on the back surface.

Gold on the back surface must be deposited at thickness more than 2 μg cm^{-2} after source preparation. If the gold is desired to be deposited before source preparation or measurement extends over long period, a thickness of 10 μg cm^{-2} is demanded. Gold-20 % palladium, however, can be used in thin thickness because of no aging effect.

4. 1. 2. 2. *Geometry of source supporting ring*

The geometrical efficiency in an ordinary $4\pi\beta$ counter is usually kept very nearly equal to unity. It may be therefore unnecessary to consider the effect due to the lack of geometry. However, when the ring with a small inner diameter is used to stretch a thin VYNS film, the effective geometry may be reduced from unity due to weak electric field, and a considerable systematic error will be caused in the extrapolation procedure.

The inner diameters (R) of rings used were 10, 15, 20 and 25mm, and the thicknesses (h) were 0. 2, 0. 5, 0. 7 and 1. 0 mm. Sources, of ^{198}Au, ^{60}Co, ^{103}Ru and ^{95}Nb, were prepared by the aluminum chloride treatment method (4. 30), and the area of the sources was a circle of about 0. 2 cm^2 (4. 26). The β detection efficiency decreased linearly with increasing geometrical factor of h/R^2. In order to consider the origin of these inefficiencies, a method of top and bottom $2\pi\beta$ countings was used, and the number of β-rays entered directly to each half counter (N_t and N_b) was calculated approximately from top, bottom and $4\pi\beta$ count rates. N_t was not dependent on the inner diameter of the rings. N_b was reduced with decreasing inner diameter of the rings, but N_b in the case of 20 and 25 mm rings was the same. A simple calculated geometrical efficiency did not agree with the experimental results. All nuclides examined revealed the similar tendency, but the energy dependecny did not clearly appear. An effective dead space described in a previous paper interpreted these experimental results. In conclusion, it is appropriate that the ring should have a thickness of 0.1~0.3 mm and inner diameter of 15~20 mm ($h/R^2 \leq 10^{-3}$).

4. 1. 2. 3. *Calculation of theoretical efficiency function*

To determine radioactivity concentration, a polynomial function of first or second order is used as the efficiency function to fit the data for the extrapolation, but in the extrapolation region there is no clear general view for determining the order of the fitting function. Actually, all participants in the international comparison of ^{139}Ce (4.13. 27) used linear function, but various polynomials, including third order, were used in that of ^{134}Cs (4.28).

In order to justify the empirical fitting procedure, the theoretical efficiency function must be calculated more accurately than the calculation using an absorption coefficient (4.29). Therefore, the β-ray energy distributions and self absorptions of spherical particle sources are calculated by using the Monte Carlo method under the continuous slowing down approximation. As a long time is required for the Monte Carlo simulations, it is examined that a general solution based on analytical calculation using plural absorption coefficients fits the self absorption obtained.

Considering a source prepared by an aluminum treatment method (4.30), the calculation is carried out for an aluminum compound, such as aluminum hydroxide [$Al(OH)_3$], probably being created. The calculation can be approximated by limiting interactions in an aluminum and oxygen mixture (Al+3•0, i. e. neglecting the hydrogen) or aluminum only (Al), and the reason was described in a previous report (4.31). The calculation requires much numerical data, and they were shown in the report.

In the Monte Carlo calculation, the position and the energy of an emitted electron is chosen and the initial spectrum is accumulated for comparison. The electron with energy above a critical energy passes through in a straight line and loses its energy according the path length. The electron with lower energy repeats the elastic scatterings and the energy losses till it disappears from the surface of the particle or the energy decreases below the threshold energy (125 eV). The energy distribution of escaped electrons and the self absorption are determined from the calculation of

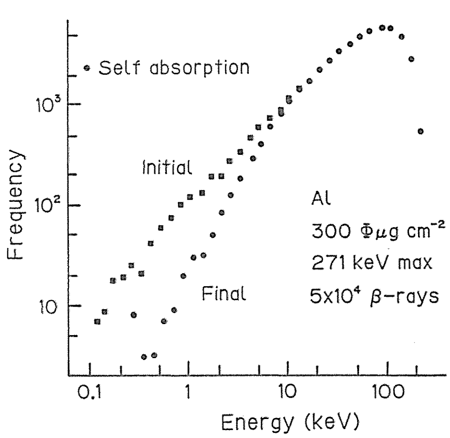

Fig. 4. 9. Example of calculated energy distribution.

many electrons. Examples of energy distribution are shown in Fig. 4. 9, where the frequency for a constant interval in the logarithmic scale is indicated. The final spectrum shows decrease from the initial one only at the low energy side and no significant differences at the high energy side above about 50 keV.

If the absorption coefficient of the source material is defined for a β-ray group, it is easy to compute the self absorption for a spherical particle source. When x denotes the distance between an arbitrary point in the particle and an arbitrary place on the particle surface, the transmission probability is

$$\int_V \exp(-\mu x)\, dV \Big/ \int_V dV, \tag{4. 10}$$

where μ is the absorption coefficient and V is the volume of the spherical particle. However, one absorption coefficient gave insufficient results for wide range of particle diameter. Then three components of absorption coefficients and the partial intensities were introduced. The main value was determined from the experimental data by Baltakmens (4. 32), and the others were approximately determind from the results of the Monte Carlo calculation for the small and large particles, respectively. These parameters were shown in a previous report (4. 31) and the calculated results will be shown in the latter sections.

4. 1. 2. 4. Optimisation of efficiency function

An efficiency function is obtained in a $4\pi\beta$(pc)-γ coincidence system by using absorber foils for the adjustment of detection efficiency or by measuring a number of sources with different self absorptions. In the former case, the effective geometry reduced from unity due to the space between source and absorber, and a considerable systematic error was caused (4. 33). In the latter case, the inhomogeneity due to the various sizes of the crystallines of the radioactive salts may give a systematic error. The effects of inhomogeneities in thin sources were investigated.

Sources were prepared on VYNS films deposited of about 1.5 μg cm^{-2} Au-20% Pd alloy and 3.5 μg cm^{-2} Au by aluminum treatment method (4. 30). Each group included the source with the smallest attainable self absorption and also one or two sources with higher values. Counting these sources by using the $4\pi\beta$(MS)-γ coincidence system in various combinations, 1, 2, etc. at a time led to the first set of results for fitting an efficiency function. Next, the sources were treated by adding carrier solution or more aluminum chloride to change their self absorption and were recounted. A new efficiency function was constructed and its slope was compared with that of the first one (4. 34).

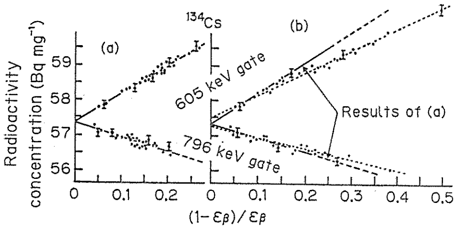

Fig. 4. 10. Results for (a) all sources subject to fairly small self absorption and (b) a source has large one.

Fig. 4. 10(a) shows an example of efficiency functions from five sources with $\varepsilon_\beta > 0.75$, all of which were prepared to consist of small crystallites only. The extrapolated results are seen to be identical well within the respective uncertainties. After that one of these sources was redried in condition to lead to the formation

of larger crystallites. This time the detection efficiencies extended down to 0.67 and Fig. 4.10(b) shows that the extrapolated results for the two γ gates are clearly different. Non-linearity becomes clearly apparent in the region above 0.2. This suggests that correct procedures of source preparation are particularly important for the efficiency function with large slope.

Usually, ψ in Eq. (4.5) can be regarded as constant irrespective of ε_β. So, the efficiency function is explained as a linear one of $(1-\varepsilon_\beta)/\varepsilon_\beta$ in the case of a constant C_k and as a second order one in the case that the C_k changes linearly with that. The C_k, calculated by the procedure in sect. 4.1.2.3, changed slowly with $(1-\varepsilon_\beta)/\varepsilon_\beta$ in the small region. Therefore, the following three conditions were assumed for the fitting functions. (a) good agreement with measured data, (b) a small number of arbitrary parameters and (c) the term C_k must be a monotonous function and the derivative at $\varepsilon_\beta=1$ is zero. The functions used for the purpose are shown in Table 4.1, and not all of them fulfill the above requirements.

Table 4.1. Various fitting functions.

	Function
1st.	$a+bx$
2nd.	$a+bx+cx^2$
1st.+2nd.	$a+bx$ $(x\leq p)$ $a+cp^2+(b-2cp)x+cX^2$ $(x>p)$
3rd.	$a+bx+cx^3$
cosh	$a+bx+cx\cdot\cosh x$

Three nuclides ^{59}Fe, ^{134}Cs and ^{141}Ce were used and the $4\pi\beta$(ppc)-γ coincidence system was used. The number of data points for the ^{59}Fe, ^{134}Cs and ^{141}Ce activity measurements was 74, 190 and 160, respectively. The two γ gates were set for ^{59}Fe and ^{134}Cs, but for ^{141}Ce only the 145 keV photopeak was available.

Fig. 4.11 shows results for ^{134}Cs with the linear extrapolated disintegration rates as a function of the fitting region. In the case of small extrapolation distance as in (a), relatively good results were obtained. However, in the case of a large extrapolation distance (b), the extrapolated value depends on the fitting region and may deviate from the true value.

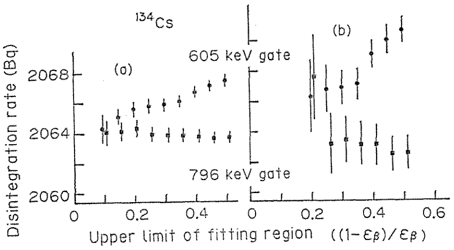

Fig. 4.11. Extrapolated disintegration rates by using linear functions. The high efficiency limits were 0.03 and 0.1 for (a) and (b), respectively.

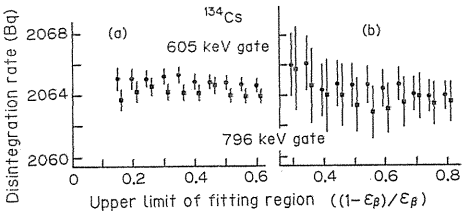

Fig. 4.12. Polynomial functions joining the first and second order were applied and other was the same as Fig. 4.11.

Often, a second order function was used where a linear fitting was insufficient. The results did not deviate greatly but they did not exactly agree either. The polynomial function joining the first and second order is an effective compromise.

Fig. 4. 12 shows the results of applying this function to the data for ^{134}Cs. In both figures, the function gives comparatively reasonable results and shows no noticeable systematic errors with changes in the fitting region. This function led to good results also for ^{59}Fe and ^{141}Ce. A weak point of this function was that the extrapolated value depended on the joining point p and that point p could not be selected rationally but only by inspection.

Also a special polynomial function of third order but with the coefficient of the second order term equal to zero, showed as good results as the first plus second order fitting function (4. 35). Fitting results using $x\cdot\cosh x$ function showed acceptable results. They were similar to those obtained with a third order function, but the distribution of these results was slightly large. The results by a fitting function of $x\cdot\exp x$ appeared similar to those obtained for a second order fitting.

The most suitable fitting function is a first order function in the region of high ε_β as predicted by calculation. However, for measurements without high efficiency data shows selection of function type is important problem.

4. 1. 3. Source preparation and evaluation

4. 1. 3. 1. Thickness measurement by α particle gauge

An α particle thickness gauge is used to measure non-destructively the thicknesses of uniform thin films. It is sometimes required to measure the mean superficial density of the radioisotope source which composes of a number of fine particles. The mean superficial density of fine uniform particles, such as polystyrene latex or ion exchange resin, dispersed on a thin supporting film was measured and compared with that calculated from the particle diameter, density and number of particles per unit area.

When a pressure of a gas between source and detector is changed in the thickness gauge, the count rate is a function of the pressure $N_0(p)$. In the case that the thin uniform film (t) is inserted, the absorption curve is displaced in parallel to the low pressure side by x.

$$N_t(p)=N_0(p+x). \tag{4. 11}$$

A non-uniform film is considered to be a set of films with various thicknesses. When the thickness distribution is shown by occupied area $\gamma(t)$, the count rate is

$$N(p)=\int\gamma(t)N_t(p)\,dt, \quad \int\gamma(t)\,dt=1. \tag{4. 12}$$

Considering Eq. (4. 11) and relation of $t=kx$, Eq. (4. 12) is

$$N(p)=\int\gamma(kx)N_0(p+x)\,kdx. \tag{4. 13}$$

When a sample has thickness of t_i and occupied area of γ_i, Eq. (4. 13) is

$$N(p)=\sum\gamma_i N_i(p)=\sum\gamma_i N_0(p+x_i). \tag{4. 14}$$

To evaluate experimentally, a mylar film with thickness of 3 or 6 μm is inserted to cover a part of α particles in the thickness gauge using of an ^{241}Am source (4. 36). The agreement of measurement and calculation for 3 μm mylar film was a natural result because of small change of slope. The agreement for 6 μm film, however, showed the appropriateness of calculation.

When a sample is composed of uniform spherical particles with radius of r and the number is n cm^{-2}, occupied area of $\gamma(t)$ is described as following

$$\gamma(t)dt = n\pi t dt/2\rho^2, \tag{4.15}$$

where ρ is density and unit of t is superficial density. Substituting Eq. (4. 15), then Eq. (4. 13) is

$$N(p) = (1 - n\pi r^2)N_0(p) + (n\pi k^2/2\rho^2)(\int x N_0(p+x)dx). \tag{4.16}$$

Constant k is determined from the measurement of a uniform film (4. 42). Next, to compare with calculation and measurement, particles with diameter of 2. 02 or 5. 7 μm polystyrene latex or 10. 8 μm ion exchange resin were sprayed on VYNS films by nebulizer. An example of results is shown in Fig. 4. 13. Curve A was obtained by least squares fit of polynomial function of fifth order, and curves B_1 and B_2 were calculated by Eq. (4. 16). Curve B_1 was obtained from the calculation for the sample with diameter of 5. 7 μm and number density of 1.0×10^5 cm^{-2}, and curve B_2 for the sample considering diameter distribution of 5. 7±1. 5 μm. The result that curve B_2 agreed well with measurement showed the appropriateness of Eq. (4. 16) and the possibility to estimate the non-uniformity of particles.

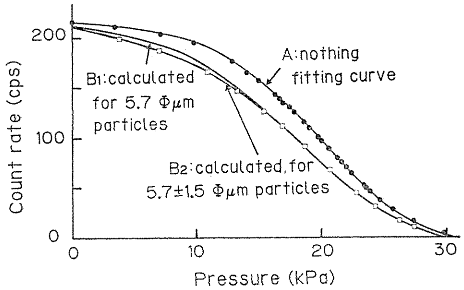

Fig. 4. 13. Measured and calculated absorption curves.

4. 1. 3. 2. Source preparation by electrospraying method

Self absorption and scattering cause the spectral distortion in spectroscopy and the loss in counting. A quantitative source preparation will be described in next section, but this section deals with non-quantitative treatment of electrospraying. When such a source by evaporation is not desired, self absorption is reduced to less than 1% for ^{60}Co by such means as electrospraying (4. 37–38), vacuum deposition (4. 39) and electro deposition (4. 40–41).

Electrospraying was performed on the source backing film with gold deposited on each surface more than 15 μg cm^{-2} by using a simple equipment (4. 42). When we prepare sources by the electrospraying method, their size and intensity distribution are important, but the mechanism of electrosprying is not clear. Vonnegut et al. (4. 43) and Drozin (4. 44) gave theoretical explanation for the yielding of the mist, but the agreement between theory and experiment was not so good. We assume the mechanism of electrospraying as following two steps. (1) A small droplet with a certain constant radius falls out from the top of a conical drop according to the balance between surface tension and electrical repulsive force of the charge in the small droplet and the charge in the rest of the conical drop. (2) Since the small droplet lies highly excited state, it breaks up to many small particles to lie ground state. And so excess energy is spent as kinetic energy of small particles.

Two spheres with radius R are considered in a tip of the conical drop. According to the step (1),

$$2\pi R\gamma = q^2/\varepsilon(2R)^2, \tag{4.17}$$

where γ and ε are surface tension and dielectric constant of the solution, respectively, and q is the charge of a droplet. The volume of spraying solution and the charge to be carried per unit time are defined as V and Q. So, $q=(4\pi R^3/3)\cdot(Q/V)$, then

$$R=(9\varepsilon\gamma V^2/2\pi Q^2)^{1/3}. \tag{4.18}$$

In the step (2), the total energy of particles with radius r, as given by Vonnegut et al. (4.43), is

$$E=3V\gamma/r+2\pi r^2Q^2/3\varepsilon_a V+K, \tag{4.19}$$

where ε_a is dielectric constant of air. The term K is independent on the radius r. A stable radius r_0 at equilibrium is found from the derivative of Eq. (4.19).

$$r_0=(9\varepsilon_a\gamma V^2/4\pi Q^2)^{1/3}. \tag{4.20}$$

Excess energy which is yielded from the change of radius should be changed to the kinetic energy of the small particles. Then each particle comes to have a velocity and gives a density distribution (4.42). The diameters of sprayed spots were explained by the above theory. Fig. 4.14 shows the density distribution measured using a GM counter with a slit for electrospraying of ethyl alcohol solution including ^{204}Tl. The corrected density was almost uniform and decreased rapidly at the boundary.

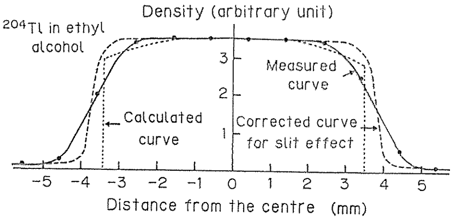

Fig. 4.14. Density distribution.

4.1.3.3. Source preparation by aluminum chloride treatment method

When quantitative source preparation is required, the most common way to counter crystallization is to use wetting or seeding agents. A wetting agent, such as insulin (4.45) or Catanac SN (4.46-47), serves to reduce the surface tension of the radioactive solution, while a seeding agent supplies fine particles. Merritt et al. (4.48) have used Ludox SM (colloidal silica) for such a purpose and Lowenthal et al. (4.49) have attempted to improve the source by drying it after spraying small particles of ion exchange resion on a source mount.

A precipitation method will bring a transformation of the radioactive nuclide and its carrier from a soluble to an insoluble form of salt, which is easier to turn into fine crystals upon drying. The method described in this section can be expected to exhibit features of both seeding and precipitation.

A good example of such a transformable salt is $AlCl_3$, and the transformation into an insoluble aluminum compound by reaction with ammonium hydroxide produces fine colloidal particles of an aluminum compound with a grain size of 1 μm (4.50).

Their surface charges bring about a uniform distribution of fine colloidal particles with grain size of 1 μm within the liquid medium (4. 30).

The procedure adopted for the source preparation was as follows. After a 20 μl parting of radioactive solution had been placed on the mount, a small amount of aluminum chloride dissolved in 20 μl of 1N hydrochloride acid was added to it. The mixed solution was first dried under an infrared lamp, then redissolved with distilled water dropped on to the surface, and finally dried again in ammonia atmosphere in a silica gel desiccator. The source was obtained after one day, but after exposure of ammonia atmosphere a final drying under the infrared lamp or in vacuum produced the source after about one hour (4. 51).

In order to determine the optimum amount of aluminum to be added to a source, the self absorption was measured on sources containing different amounts of aluminum. Three nuclides, ^{60}Co, ^{95}Nb and ^{103}Ru, were chosen in consideration of their different energies and conditions of solution. The ^{60}Co and ^{103}Ru nuclides were prepared in the chemical form of chloride, but the ^{95}Nb was made into oxalate. The result is shown in Fig. 4. 15. With a rise in the surface density of the deposited aluminum, the self absorption of the ^{60}Co and the ^{103}Ru sources is almost constant against the amount of aluminum below a 2 μg cm^{-2} superficial density; beyond this point the curves begin to rise, while with the ^{95}Nb source the curve lowers to an optimum range around 0. 25~2. 5 μg cm^{-2}. Cobalt chloride can easily be changed into an insoluble salt by the reaction with ammonia, and the precipitation method was equally effective with the ^{103}Ru source producing a result similar to ^{60}Co. In the case of ^{95}Nb, it contained a large amount of oxalic acid, which was non-volatile and which produced soluble ammonium oxalate. This would tend to increase the size of the precipitated soluble salt with a decrease in the amount of aluminum.

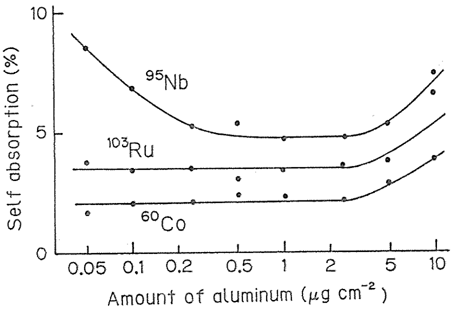

Fig. 4. 15. Relation between self absorption and amount of aluminum.

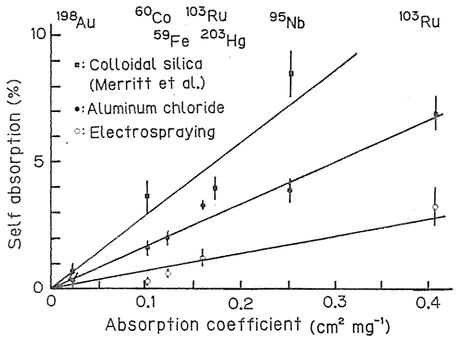

Fig. 4. 16. Self absorption of sources prepared by a few methods.

4. 1. 3. 4. *Evaluation of self absorption*

In this section, the self absorption of sources prepared by the methods described in previous sections will be shown for several radioactive nuclides and the results of special experiment will be evaluated.

Fig. 4. 16 shows the self absorption of sources prepared by electrospraying and aluminum chloride treatment and the value reported by Merritt et al. for sources prepared by colloidal silica treatment (4. 54). The error bars give an indication of the reproducibility related each

nuclide. The sources prepared by aluminum chloride treatment contained 2 μg cm^{-2} of aluminum and the sources by colloidal silica treatment contained 2 μg cm^{-2} of carrier.

The plots reveal that the values obtained by aluminum treatment were significantly lower than those obtained by colloidal silica treatment. Meanwhile, the values obtained by electrospraying method were lower than those by the other method, so the self absorption was smaller than the absorption of the mount. The good source prepared by electrospraying method showed no particle within the resolving power of an optical microscope (<1 μm).

Fig. 4. 17 shows the diameter distribution of particles to constitute the source. The source prepared by collodial silica treatment probably gave the large self absorption because of existence of particles with large diameter. Also, mean particle diameters of some sources were constant for the change of mean superficial density up to about 5 μg cm^{-2}.

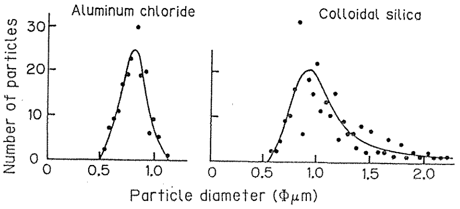

Fig. 4. 17. Distribution of particle diameter in sources.

Systematic treatment to correct the self absorption considerably succeeded for thick sources (4. 52-56). However, that for thin sources has not been established due to the difficulty of recognition of microscopic appearance. Then, the self absorption was measured for the source prepared mimetically. One was the granular source which consisted of fine ion exchange resin particles absorbing radioactive nuclides. The other was the membraneous source sandwiched with two absorbers of VYNS, but was not explained in this report (4. 57).

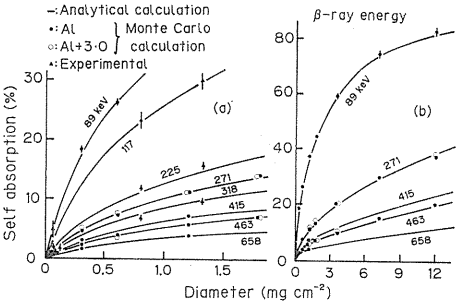

Fig. 4. 18. Self absorption of a spherical particle source.

Fig. 4. 18 shows the self absorption measured for spherical particle sources and calculated by the Monte Carlo method described in sect. 4. 1. 2. 3. The solid lines were the results of the analytical calculation using three parameters for the absorption coefficient described previously. Good agreement among them shows that the microscopic absorption of β-rays cannot be explained by an absorption coefficient and that use of three absorption coefficients covers considerable range of absorption.

4. 1. 4. *Absolute radioactivity measurement and application*

Activity standardisation of β-γ emitting nuclides can be easily carried out in the condition described in previous sections. This section will deal with a few examples of special nuclides and application.

4. 1. 4. 1. *Absolute standardisation of* ^{55}Fe

The absolute disintegration rate of a ^{55}Fe source emitting only X-rays has, ordinarily, been measured by the 4πX counting method (4.58). We attempted the calibration of a ^{55}Fe source by the X-γ coincidence method (4.59). A known amount of ^{57}Co or ^{54}Mn isotopes, which emits both X- and γ-rays, is added to a ^{55}Fe source. The atomic number of iron is close to that of cobalt and manganese and then the energy of the characteristic X-rays emitted from manganese is nearly same as that of iron and chromium. The radioactivity of each mixed source is counted with X-γ coincidence system described in sect. 4. 1. 1. 2, and then the absolute disintegration rate of the ^{55}Fe source is calculated by analysing the counting results. The ^{55}Fe solution used in this experiment was a standard solution supplied by the Radiochemical Centre. The absolute disintegration rates of ^{57}Co and ^{54}Mn sources were well defined by the X-γ coincidence method. Either ^{57}Co or ^{54}Mn master solution was mixed with the standard solution of ^{55}Fe. The mixing ratios of the solutions were determined by weighing the solutions with a chemical balance. The counting sources were prepared by dropping and evaporating the solution on a thin mylar film, and the radioactivity of these sources were measured with the X-γ coincidence system. The radioactive concentrations of the ^{55}Fe solution measured by the ^{57}Co and ^{54}Mn tracer method were coincided within 1.4%.

4. 1. 4. 2. Absolute standardisation of ^{85}*Sr*

Absolute standardisation of ^{85}Sr is described as an extension of 4πe$\cdot$X-γ coincidence counting. The nuclide decays to the excited level of ^{85}Rb by electron capture and the 514 keV γ-rays are emitted with half life of 0.96 μs. Therefore, the conventional 4πe$\cdot$X-γ coincidence technique with resolving time of about 1 μs cannot be applied to this nuclide. The standardisation can be carried out by various methods. In this section, the delayed 4πe$\cdot$X-γ coincidence technique with two different resolving times is described (4.60).

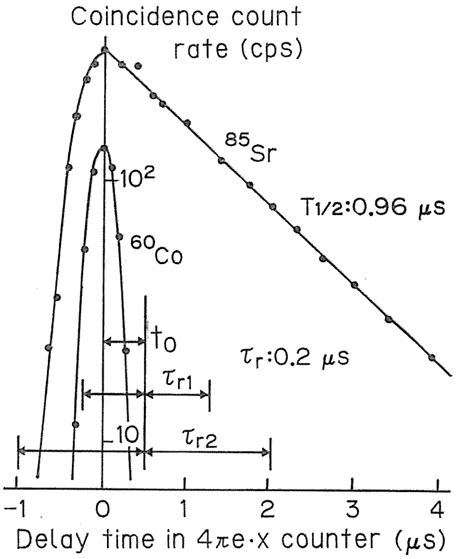

Fig. 4. 19. Delayed coincidence curves.

Fig. 4. 19 shows the delayed coincidence curves of ^{85}Sr and ^{60}Co which were measured by resolving time of 0.2 μs. The 0.96 μs of measured half life agreed with the reported values (4.61). When the 4πe$\cdot$X-γ coincidence counting with delay time of t_0 and resolving time of $\tau_{r1}(\tau_{r1}>t_0)$ is applied to ^{85}Sr (shown in Fig. 4. 19), the apparent disintegration rate

$$\frac{N_\gamma \cdot N_e}{N_{c1}} = N_0\left\{1+\frac{1-\varepsilon_e}{\varepsilon_e}\left(\frac{\varepsilon_{\beta\gamma}+\alpha\varepsilon_{ce})}{1+\alpha}\right)\right\}\left\{1-\exp\left[\frac{\ln 2}{T_{1/2}}(\tau_{r1}+t_0)\right]\right\}^{-1}, \tag{4.21}$$

where $T_{1/2}$: half life of the level, suffix e shows the Auger electrons and X-rays and the other notations were described in sect. 4. 1. For coincidence counting with the resolving time of $\tau_{\gamma 2}$, the equation replacing suffix 1 to 2 is obtained. The N_0 and t_0 are calculated from two equations,

$$N_0=\frac{N_\gamma \cdot N_e}{N_{c2}}\left\{1-\exp\left[\frac{-\ln 2}{T_{1/2}}(\tau_{\gamma 2}+t_0)\right]\right\}\left\{1+\frac{1-\varepsilon_e}{\varepsilon_e}\left(\frac{\varepsilon_{\beta\gamma}+\alpha\varepsilon_{ce}}{1+\alpha}\right)\right\}^{-1} \quad (4.22)$$

$$t_0=\frac{T_{1/2}}{\ln 2}\ln\left\{\left(\frac{\varepsilon_2}{\varepsilon_1}-1\right)\Big/\left(\frac{\varepsilon_2}{\varepsilon_1}\exp\frac{-\tau_{\gamma 1}\ln 2}{T_{1/2}}-\exp\frac{-\tau_{\gamma 2}\cdot\ln 2}{T_{1/2}}\right)\right\}, \quad (4.23)$$

where $\varepsilon_i=N_{ci}/N_\gamma (i=1, 2)$.

Fig. 4. 20 shows the result calculated by Eqs. (4. 22) and (4. 23) that $\tau_{\gamma 1}$ and $\tau_{\gamma 2}$ are 0. 47 and 1. 81 μs, respectively. A good efficiency function was obtained and the disintegration rate was determined with accuracy of ±0. 5 %. To evaluate the validity, the disintegration rate was measured also by two scintillators whose efficiency was previously determined and both results agreed within the accuracy.

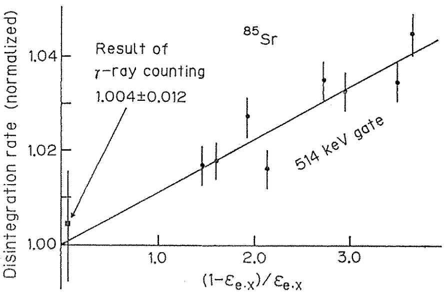

Fig. 4. 20. Efficiency function obtained by double coincidence counting.

4. 1. 4. 3. *Absolute standardisation and measurement of decay data of ^{86}Rb and ^{103}Ru*

About 90 % of ^{86}Rb transits directly to the ground level of the ^{86}Sr and ^{103}Ru has a large internal conversion coefficient for the main 40 keV transition; therefore, the γ-ray emission probabilities of both nuclides cannot be determined only from the relative γ-ray intensities. The γ-ray emission probability was evaluated from the disintegration rate, as measured with the $4\pi\beta$-γ coincidence apparatus described in sect. 4. 1. 1. 1, and the γ-ray intensity, as determined by means of the scintillators forming the apparatus. The half life was determined from the long-term measurements of the disintegration rate (4. 62).

Fig. 4. 21 shows the efficiency function of ^{86}Rb, where the γ channel was set on the 1077 keV photopeak and where the self absorption was changed by adding aluminum chloride to the source (4. 51). The efficiency function of ^{103}Ru was similar to the one of ^{86}Rb, where the γ channel was set on the 497 keV photopeak. ^{198}Au, ^{95}Nb, ^{54}Mn, ^{46}Sc and ^{60}Co were used for determination of detection efficiency of the detectors, and the sum efficiency of two detectors was adopted because of small effect for the reproducibility of source position. The efficiency for each detector was used for reference.

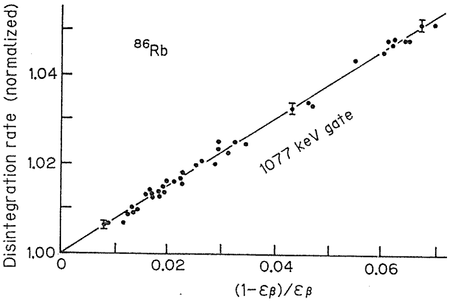

Fig. 4. 21. Efficiency function of ^{86}Rb.

The γ-ray emission probability of ^{86}Rb and ^{103}Ru is shown in Tables 4. 2 and 4. 3 along with other values. The results were obtained from five ^{86}Rb sources (20 γ-ray spectra) and five ^{103}Ru sources (29 γ-ray spectra). In the case of ^{86}Rb, the present value agrees with other results which were determined by various methods, because β-rays are scarcely absorbed for the high maximum energy and this nuclide emits only monochromatic γ-rays. The value for ^{103}Ru has not been measured by any authors, but the present values of relative intensities agree with the results obtained by using Ge(Li) detectors.

Table 4. 2. γ-ray emission probability of ^{86}Rb (%).

Energy (keV)	1077
Campion et al. (4.29)	8.66±0.15
Brandhorst et al. (4.63)	8.79±0.09
Present work	8.64±0.04

Table 4. 3. γ-ray emission probability of ^{103}Ru (%).

Energy (keV)	497	557	610
Present work	91.08±0.76	0.80±0.12	5.75±0.08

Relative intensity

Energy (keV)	497	610
Petterson et al. (4.64)	100	6.43±0.13
Macias et al. (4.65)	100.0±3.0	6.33±0.20
Present work	100.0±0.8	6.31±0.09

Table 4. 4. Half lives of ^{86}Rb and ^{103}Ru (day).

^{86}Rb		^{103}Ru	
Niday (4.66)	18.64±0.04	Debertin (4.68)	39.35±0.05
Baba et al. (4.67)	18.61±0.04	Houtermans et al. (4.69)	39.254±0.008
Present work	18.631±0.018	Present work	39.214±0.013

Four ^{86}Rb sources with different disintegration rates were measured during two or three half lives, and six ^{103}Ru sources during one or two half lives, for the determination of accurate half life. Table 4. 4 shows the results obtained and reported by other authors. The present results are the simple mean values since the differences in the variances were not large and meaningful. If the half life was calculated from the apparent disintegration rates, the variance was about twice as large as the one shown in the table.

4. 1. 4. 4. Effect of ^{55}Fe impurities for standardisation of ^{59}Fe

Activity standardisation of ^{59}Fe can be easily carried out by $4\pi\beta$-γ coincidence counting and efficiency extrapolation. Fig. 4. 22 shows an example of measurement by using the $4\pi\beta$(ppc)-γ system. It is important to extend such measurements to the highest attainable efficiencies where the efficiency function is likely approximate a straight line whose extrapolation is less uncertain than extrapolation of higher order functions (sect. 4. 1. 2. 4). Uncertainties in extrapolations are due also to radionuclide impurities. If impurities emit energetic photons they are readily identified by semiconductor detector. This method is not always practical for

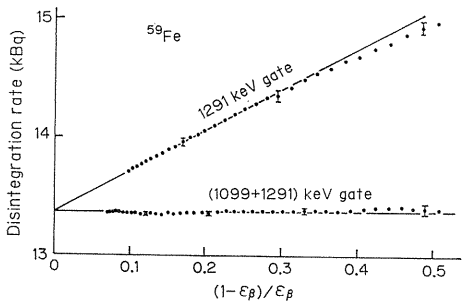

Fig. 4. 22. Efficiency function of ^{59}Fe.

nuclides decaying with the emission of only low energy radiations, such as ^{55}Fe or soft β emitters. This section will present a procedure for detecting ^{55}Fe impurities in ^{59}Fe and extrapolating the efficiency function of ^{59}Fe (4. 70).

Sources were prepared from the four ^{59}Fe solutions which were received from the New England Nuclear Co. in 1983. The measurement was carried out using the $4\pi\beta$(ppc)-γ system at a pressure of 1. 28 MPa P-10 gas. Fig. 4. 23 shows the worst case of the change of efficiency function with lapse of time, and the effects were caused by a longer-lived radionuclide than ^{59}Fe ($T_{1/2}$=44. 5 d). This pointed to ^{55}Fe ($T_{1/2}$=1000 d) as a likely impurity which must be suspected in neutron irradiations of iron.

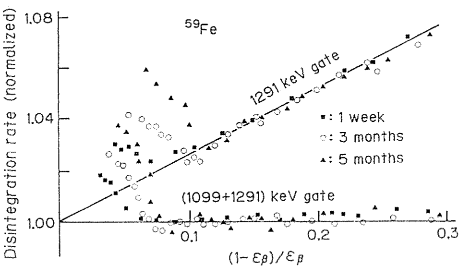

Fig. 4. 23. Effect of decay rates of ^{59}Fe and ^{55}Fe on the shape of the efficiency function.

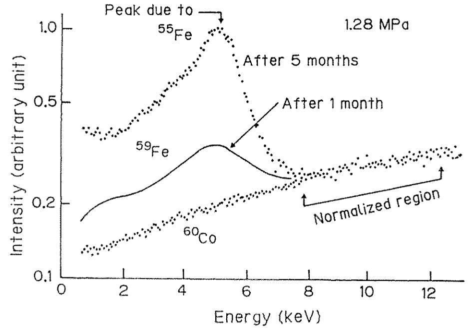

Fig. 4. 24. Pulse height spectra of ^{59}Fe and ^{60}Co in the $4\pi\beta$ counter.

Fig. 4. 24 shows the pulse height spectra for ^{59}Fe and ^{60}Co in the $4\pi\beta$ counter. There is a clearly defined peak at about 5 keV which corresponds to the Mn K Auger electrons emitted after decays of ^{55}Fe. These changes of spectra were not recognized in the measurement $4\pi\beta$ counter at an atmospheric pressure. The concentration of ^{55}Fe in the ^{59}Fe solutions estimated from these spectra were about 0. 6 to 1. 7%. Since effects due to ^{55}Fe impurities in ^{59}Fe appear only at high efficiency end of the efficiency function, these effects can be avoided by omitting those data when proceeding to the extrapolation, but the final result would, of course, be less accurate.

4. 2. *Standardisation of gaseous source*

4. 2. 1. *A new principle of the standardisation method*

When a radioactive sample is originally gaseous or is able to be turned into gaseous state, proportional counters are frequently used because of high detection efficiency and high discrimination capability against background radiations. Proportional counters, on the other hand, have a defect called "end-effect" which decreases the counting efficiency due to the lowering of the electric field at both ends of the anode wire as shown in Fig. 4. 25 (a) and (b) and brings an inaccurate result in the radioactivity determination.

Although a few methods (4. 71–72) have been proposed to overcome the end effect, each has its own shortcoming. We have developed a new method (4. 73–74) which can define the effective volume for the counting without the influence of the end effect. When a position-sensitive proportional counter with resistive anode wire is used, count rate as a function of position signal S which is proportional to the axial position in the counter is obtained as shown in Fig. 4. 25(c). With position calibration sources situated at the positions without the end effect as shown by arrows in Fig. 4. 25(a), position calibration signals are obtained as shown in (d). Hence, we can correlate the actual volume, which is completely free from the end effect and is hereafter called the effective volume, defined by the broken lines in (a) with the count rate in the broken lines in (c) and accordingly the radioactivity per unit volume in the counter is obtained. Knowing the total volume of the counter, we can obtain the total activity in the counter without suffering the influence of the end effect.

Since a charge division type with a resistive anode wire is employed for position sensitive proportional counter, when a β-particle with very low energy is detected near the end of the counter, the pulse height obtained from the opposite end is extremely low and hence the detection efficiency has a tendency to decrease. To avoid this decrease, lump resistors A are introduced as shown in Fig. 4. 26(a). However, the introduction of lump resistors A brings the deterioration of position resolution as a position-sensitive detector. To increase position resolution, a partially resistive anode wire is introduced as shown in Fig. 4. 26 (b). Then we can expect the relation between position signal pulse height S and geometrical position G on the anode wire as shown in

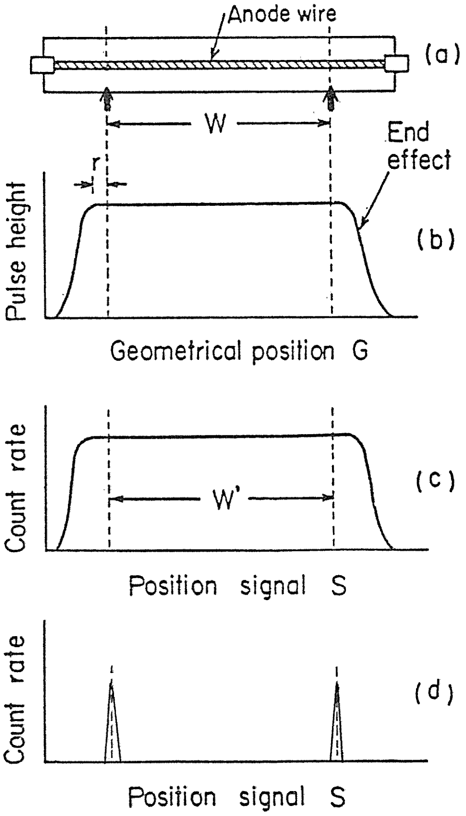

Fig. 4. 25. Basic principle of the use of position-sensitive proportional counter to eliminate end effect.

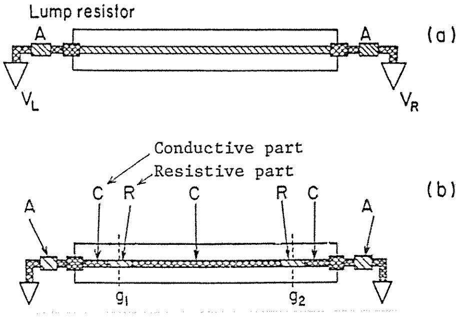

Fig. 4. 26. Continuous resistive anode wire (a) and partially resistive anode wire (b) C: conductive, R: resistive.

Fig. 4. 27 for the case (a) uniform resistive anode wire without lump resistors, (b) with lump resistors and (c) a partially resistive anode wire with lump resistors. The relation (c) can bring uniform detection efficiency (4. 75) throughout the anode wire except for the end regions and an excellent position resolution which can accurately define the effective volume.

4. 2. 2. *Experimental apparatus and its characteristics*

The structure of the position-sensitive proportional counter for the direct measurement of radioactivity of ^{3}H-labeled methane is shown in Fig. 4. 28. The cathode has three ports for the injection of ^{3}H-labeled gas and for the insertion of ^{3}H solid sources for position calibration.

A partially resistive anode wire was prepared as follows. A Pyrex glass wire was suspended in the vacuum-deposition bell-jar and rotated. Chromium was first vacuum-deposited to make a continuous resistive anode wire with a resistance of about 20 kΩ cm^{-1}. Over a length of 5 cm, two parts of the wire were covered with

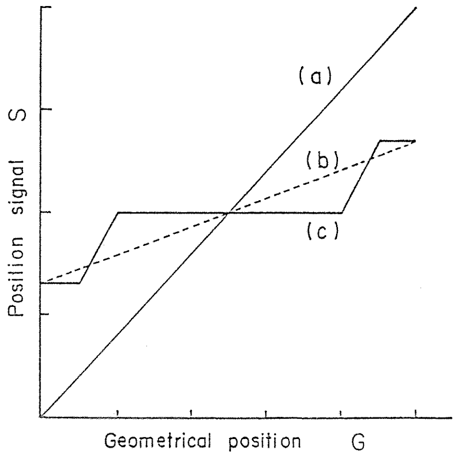

Fig. 4. 27. Relation between position signal S and geometrical position G on continuous resistive anode wire for the case (a) without lump resistors, (b) with lump resistors and (c) on partially resistive anode wire with lump resistors.

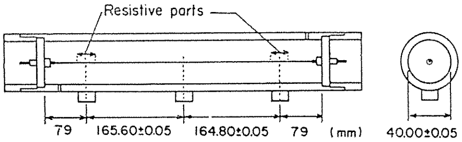

Fig. 4. 28. Position-sensitive proportional counter with partially resistive anode wire.

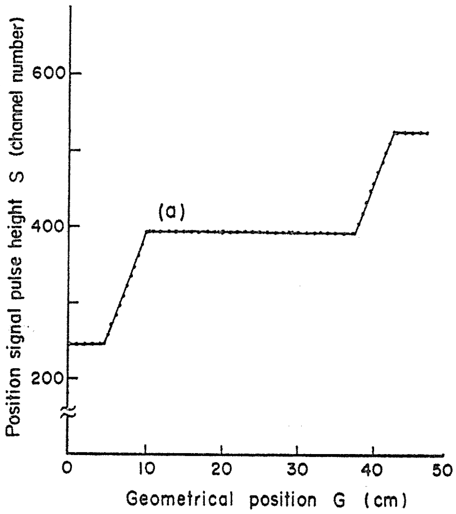

Fig. 4. 29. Characteristic of partially resistive anode wire.

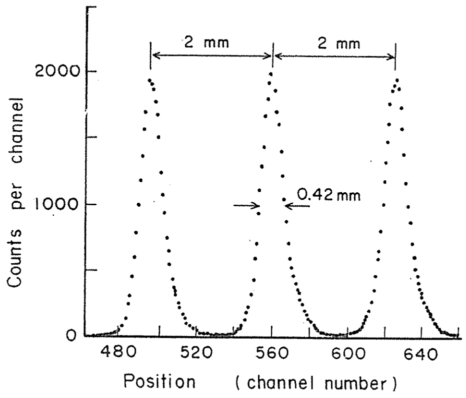

Fig. 4. 30. Position resolution.

aluminum foil and gold was, then, vacuum-deposited on the remaining parts of the wire to make conductive parts. The relation between the position signal pulse height S and the geometrical position G is quite satisfactory as shown in Fig. 4. 29 which is very similar to that we expected in Fig. 4. 27 (c). The position resultion for collimated Mn KX-rays on a resistive part is shown in Fig. 4. 30 with a full width at half maximum of 0. 42 mm.

4. 2. 3. *Direct measurement of radioactivity of ^{3}H-labeled methane*

There are two quantities related to a radioactive gas to be measured; one is the total activity of the injected gas and the other is the activity per unit volume, or mole, in the counter.

Fig. 4. 31 shows the position spectrum with position calibration sources. The peaks c_1 and c_2 show the positions of the calibration sources which define the edges of the effective volume of the counting. The peaks D_1, D_2 and B are the background counts at the conductive parts of the anode wire. The position calibration sources, then, were taken out and ^{3}H-labeled methane with a volume of 1. 1 cm^3 was injected through the central port. Fig. 4. 31 (b) shows the position spectrum measured for 5. 12 seconds after the injection. As it took time for the diffusion of the ^{3}H-labeled gas from the conductive part B to the conductive parts D_1 and D_2 shown in (a), there are, as seen in (b), negligibly small counts at the positions corresponding to D_1 and D_2 when the background counts are subtracted. The total count in the region shown by broken lines, therefore, corresponds to the total activity of the injected ^{3}H-methane, although the error is rather large due to the short measuring time. The total activity was 124±4 Bq.

^{3}H-labeled gas was circulated through a tiny pump for 8 minutes and the position spectrum was measured. The gas was again circulated and the spectrum was measured as shown in Fig. 4. 31(c). Both spectra were same, which meant that the ^{3}H-labeled gas was uniformly diffused throughout the counter. From the total counts in the range between the broken lines after subtracting the background counts, the activity in the unit volume of the counter was found to be 202. 5±1. 6 mBq cm^{-3} with an uncertainly of ±0. 79 % (standard deviation).

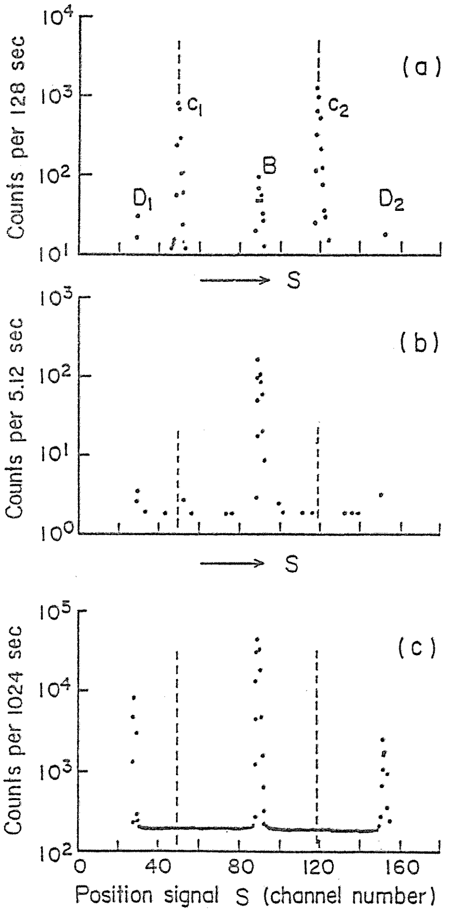

Fig. 4. 31. (a) Position spectrum with position calibration sources, (b) that of ^{3}H-labeled methane measured for 5. 12 s just after the injection and (c) that for 1024 s after complete diffusion.

The total volume of the counter including the pumping system was calculated from the drawing shown in Fig. 4. 28 and was 626 cm^3. The total activity injected into the counter was 127 ± 1.0 Bq, which was similar to the value of 124 ± 4 Bq determined preliminary by Fig. 4. 31 (b).

A new principle by use of a position-sensitive proportional counter was confirmed to be very effective for the direct measurement of the activity of ^{3}H-labeled gas without suffering the influence of end effect and will be useful for any other gaseous samples.

5. Radioactivity monitors

In this chapter development and application are described of novel detectors for α- and β-activity monitoring, i.e. spark chambers, air proportional counters and background-compensated GM counters, and of a new method for tritium-in-air monitoring using conventional liquid scintillation counters.

5. 1. Spark chambers

5. 1. 1. A parallel plate spark chamber for α-activity imaging

5. 1. 1. 1. Description of a spark chamber

Spark chambers are position sensitive detectors and they use as a position signal electrical sparks locally generated by incident radiations. Fig. 5. 1 shows the scheme of a spark chamber imaging device (5. 1). The chamber is composed of a pair of parallel plate electrodes, i.e. an anode made of electroconductive glass plate and a cathode made of stainless-steel wire mesh, which are separated by 5 mm. The gap between the electrodes was filled with mixtures of argon gas and a few percent of ethanol vapor with pressure from 40 to 101 kPa at room temperature. A high voltage was applied to the anode through a resistor of 98 MΩ, and counting signal was derived from the cathode which was connected through an RC network to the ground. Since capacitance of the anode to the ground was 37 pF, recovering time constant after sparking was 3. 6msec. α- and β-rays from a RaDEF source were injected through the mesh cathode to the gap and photographs of spark distributions were taken through the glass anode with a usual photographic camera.

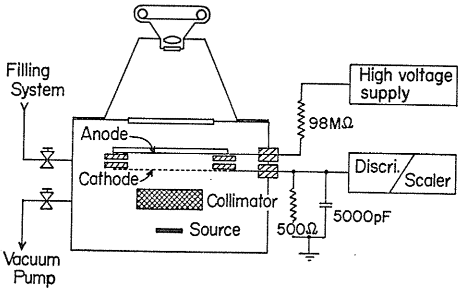

Fig. 5. 1. Scheme of the spark chamber imaging device.

5. 1. 1. 2. Dependence of sparking voltage on the specific ionization of charged particles

Fig. 5. 2 shows counting characteristics for the RaDEF source and for background. Two steps of plateau are seen for the RaDEF source. In comparison with counting characteristics for β-ray sources and for background it was clear that the

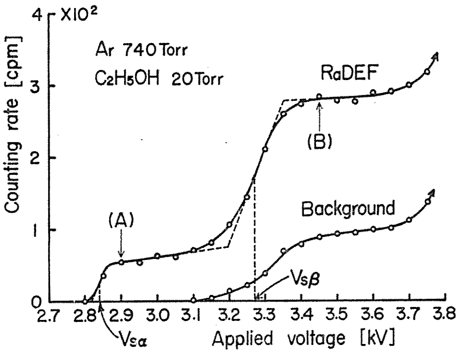

Fig. 5. 2. Counting characteristics of the spark chamber for a RaDEF source and for background. $V_{s\alpha}$ and $V_{s\beta}$ show experimental sparking voltages for α- and β-rays, respectively. (A) and (B) respectively correspond to applied voltages at which spark images (a) and (b) in Fig. 5. 3 were obtained.

first step was due to α-rays alone while the second was due to both α- and β-rays. It was found that the sparking voltage for α-ray incidence decreased more than 10% compared with that for β-ray incidence.

Theoretical consideration based on the streamer theory of spark reveals that sparking voltage V_s(volts) is expressed as a function of the specific ionization N_0 (cm^{-1}) of incident particles in the form (5. 1)

$$\begin{aligned} V_s &= F[15.8+(1/2)\ln V_s-\ln N_0]^{1/2}(pd/A)^{1/2}+Bpd \\ F &= [1-2(pd/A)\{V_s/(V_s-Bpd)^3\}]^{-1/2} \end{aligned} \tag{5.1}$$

where p is the pressure of filling gas, d is the gap length, A and B are constants, and normal incidence is assumed. Calculated values of sparking voltages $V_{s\alpha}$ and $V_{s\beta}$ for the incidence of α- and β-rays, respectively, are shown in Table 5. 1 with values of specific ionizations N_α and N_β for α- and β-rays, respectively. Experimental values of $V_{s\alpha}$ and $V_{s\beta}$, also shown in Table 5. 1, were determined to be applied voltages at which a half of the plateau counting rate was obtained, as shown in Fig. 5. 2. Agreement between theoretical and experimental values of $V_{s\alpha}$, $V_{s\beta}$ and $(V_{s\beta}-V_{s\alpha})/V_{s\beta}$ is excellent, which indicates that the decrease of sparking voltage for α-ray incidence was well explained with the large specific ionization of α-rays.

Table 5. 1. Comparison between calculated and experimental values of $V_{s\alpha}$, $V_{s\beta}$ and $(V_{s\beta}-V_{s\alpha})/V_{s\beta}$.

$\frac{p(C_2H_5OH)}{p(\text{total})}$	p [kPa]	N_α [cm^{-1}]	N_β [cm^{-1}]	Calculated values			Experimental values		
				$V_{s\alpha}[V]$	$V_{s\beta}[V]$	$\frac{V_{s\beta}-V_{s\alpha}}{V_{s\beta}}$	$V_{s\alpha}[V]$	$V_{s\beta}[V]$	$\frac{V_{s\beta}-V_{s\alpha}}{V_{s\beta}}$
$\frac{20}{760}$	40.0	1.53×10^4	39.6	1640	1925	0.15	1610	1840	0.13
	53.3	2.11	52.8	1940	2270	0.15	1890	2200	0.14
	66.7	2.75	66.0	2220	2590	0.14	2190	2545	0.14
	80.0	3.42	79.2	2475	2885	0.14	2470	2850	0.13
	101.3	4.66	100	2865	3330	0.14	2840	3275	0.13
$\frac{40}{760}$	40.0	1.61×10^4	40.5	2045	2360	0.13	1960	2280	0.14
	53.3	2.23	54.0	2450	2815	0.13	2365	2710	0.13
	66.7	2.91	67.5	2830	3235	0.13	2690	3060	0.12

5. 1. 1. 3. *α-activity imaging for α- and β-active samples*

Fig. 5. 3 shows spark images obtained with a collimator of cross cut Lucite plate put on the RaDEF source, where a Myler film is stretched along one direction of the cross to shield α-rays alone. It is seen from Fig. 5. 3 that a spark image by α-rays alone was obtained with a low applied voltage at 2900 V while an image by both α- and β-rays was obtained at 3450 V. This indicates that it is possible to obtain α-activity images with α- and β-active samples by setting high voltage low enough to generate sparks by α-rays alone.

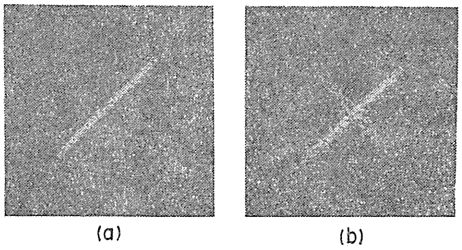

Fig. 5. 3. Spark images of a RaDEF α- and β-ray source. Applied voltage: (a) 2900 V, (b) 3450 V.

5. 1. 2. *A hybrid spark chamber for β-activity imaging*

5. 1. 2. 1. *Principle and construction*

Conventional parallel plate spark chambers described above have been proved to be unstable devices for the detection of minimum ionizing β-rays, though they have stable operation for α-rays. Instability of spark chambers is ascribed to spurious sparks which appear independently of incident particles. Those sparks are considered to be triggered by field emission of electrons from the cathode. We learned in a previous section that stable operation could be obtained with the decrease of sparking voltage when strongly ionizing α-rays were incident on the spark chambers. This induced us to construct a new type of spark chamber, i. e. a hybrid spark chamber (5. 2-5. 6), which has a parallel plate spark chamber gap and a parallel plate proportional chamber gap in the same gas space. With this construction of the chamber, a small number of electrons produced in the proportional chamber gap by an incident β-ray are largely multiplied before they trigger a spark in the spark chmber gap, and hence the same effect would be expected as the incidence of strongly ionizing α-rays.

Fig. 5. 4 shows the scheme of the hybrid spark chamber. The chamber consists of three plane parallel electrodes A, G 1 and G 2 in working gas, with a gap length of 5 mm. The electrode A is made of electroconductive glass plate, and the electrodes G1 and G 2 are stainless-steel wire meshes. A positive high voltage V_p of $2\sim3$ kV was applied to the electrode G 1, the electrode G 2 being the ground, and a higher voltage V_s of $5\sim6$ kV to the electrode A through quenching resistors. A mixture of argon and ethanol vapor saturated at 0℃ flowed constantly through the gaps at atmospheric pressure. β-ray plane sources such as thin-layer or paper chromatograms were placed in less than 1mm from the electrode G 2.

Fig. 5. 5 shows operational principle of the chamber. A β-ray emitted from the source ionize the gas in the proportional chamber gap between the electrodes G 1 and G 2, and also the spark chamber gap between the electrodes A and G1. Electrons produced there are accelerated by the electric field in each gap and start electron avalanches. Since the field strength in the spark chamber gap is controlled to be not so large as to trigger a spark independently, electrons multiplied in the proportional chamber gap start electron avalanches in the spark

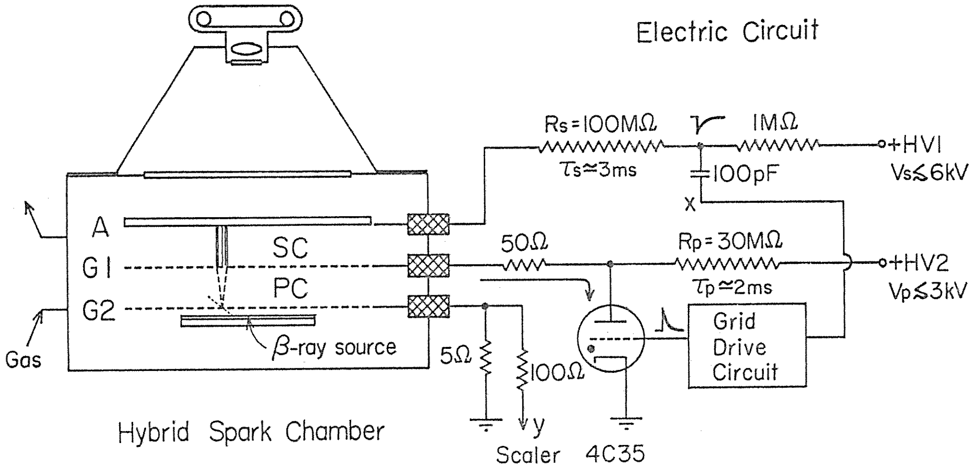

Fig. 5. 4. The hybrid spark chamber and the associated electronic circuit. SC: spark chamber gap; PC: proportional chamber gap.

chamber gap after passing through the electrode G 1. When one of these avalanches reach the critical size, a streamer followed by a spark occurs. The critical size of an electron avalanche is usually attained only at the point where the avalanche length becomes longest, and hence most sparks will be observed at the points where β-rays cross the electrodes G 2, as shown in Fig. 5. 5.

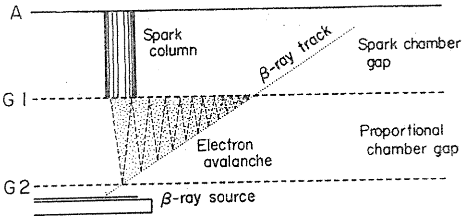

Fig. 5. 5. Relation between β-ray track and spark location.

Since a low field strength below that of breakdown is applied to the spark chamber gap, field emission of electrons from the spark chamber cathode G 1 cannot cause spurious sparks. Although electrons from the proportional chamber cathode G 2 can cause spurious sparks, the rate of the field emission is usually low enough due to the low applied field strength in the proportional chamber gap, which is the reason we can obtain good stability with hybrid spark chambers.

5. 1. 2. 2. Electronic circuitry—a thyratron discharge circuit

Fig. 5. 4 also shows an electronic circuit of the chamber. A thyratron discharge circuit was used to suppress the occurrence of sparks induced in the proportional chamber gap by sparking in the spark chamber gap. Since the induced sparks produce local accumulation of positive charges on the proportional chamber cathode, they may promote field emission of electrons from this cathode, thus reducing the stability of the hybrid spark chambers.

A hydrogen thyratron 4C35 was connected to the proportional chamber gap in parallel, and it was triggered by the voltage fall signal appearing on the electrode A by sparking in the spark chamber gap, thereby reducing the voltage applied to the electrode G1 to nearly zero volt within 0.2 μs of sparking in the spark chamber gap. Since the induced sparks occurred more than 0.2 μs later than the preceding sparks in the spark chamber gap (5.3, 5.5), the occurrence of the induced sparks could be completely suppressed with this circuit.

Voltage falls on the electrode A and on the electrode G1 by occurrence of a spark are restored exponentially with each time constant τ_s and τ_p, i.e. the product of the quenching resistance and the capacitance between the electrode and the ground. Since the capacitances of the electrodes A and G1 to the ground were found to be 33 pF and 67 pF respectively, a value of 100 MΩ for R_s and that of 30 MΩ for R_p were chosen to become $1\,\text{ms} \lesssim \tau_p (\simeq 2\,\text{ms}) < \tau_s (\simeq 3\,\text{ms})$ (5.6).

Effects of the thyratron discharge circuit were examined on stability of the hybrid spark chamber by using an intentionally contaminated G2 electrode. The electrode was deposited on the surface with barium stearate monomolecular films. Four-layer films about 10^{-6}cm in thickness were used in the experiment, since the field emission of electrons due to the accumulation of positive charges is considered to be significant when the thickness of dielectric films is between 10^{-7} and 10^{-4}cm on a cathode surface (5.7, 5.8).

Fig. 5.6 shows counting characteristic curves when a voltage V_p of 2.8 kV is applied to the proportional chamber gap. It is seen from this figure that spurious sparks increase sharply with applied voltage V_s when the discharge circuit is not used. This means that good stability cannot be obtained without the discharge circuit when the contamination of the electrode G2 is appreciable. Such contamination occurs inevitably by deposition of the decomposition products of organic components contained in the working gas on the surface of this electrode. When the thyratron discharge circuit was used good stability was obtained as seen in Fig. 5.6. This is because, in this case, positive charges could not be accumulated on the surface of the electrode G2 by suppression of sparking in the proportional chamber gap.

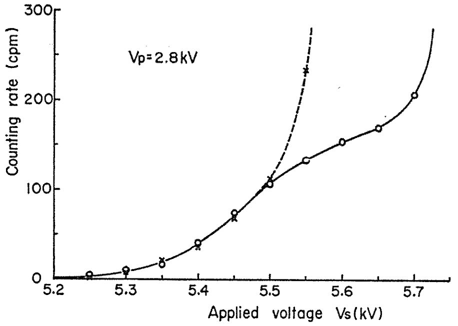

Fig. 5.6. Counting characteristics for a ^{60}Co β-ray source obtained (full line) with and (dashed line) without the thyratron discharge circuit.

5. 1. 2. 3. *Spatial resolution*

Spatial resolution of the chamber was measured with a ^{14}C triangular plane source which was covered with a slotted grid made of aluminum foil. The slots had a width of 2 mm, and were separated by 3, 2 and 1mm respectively. Fig. 5.7 shows images of the source. It is seen from this figure that the resolution of the chamber was approximately 1 mm for ^{14}C β-rays which have long ranges in the working gas. Even better resolution of less than 1 mm was observed with short range ^{3}H β-rays (5.4).

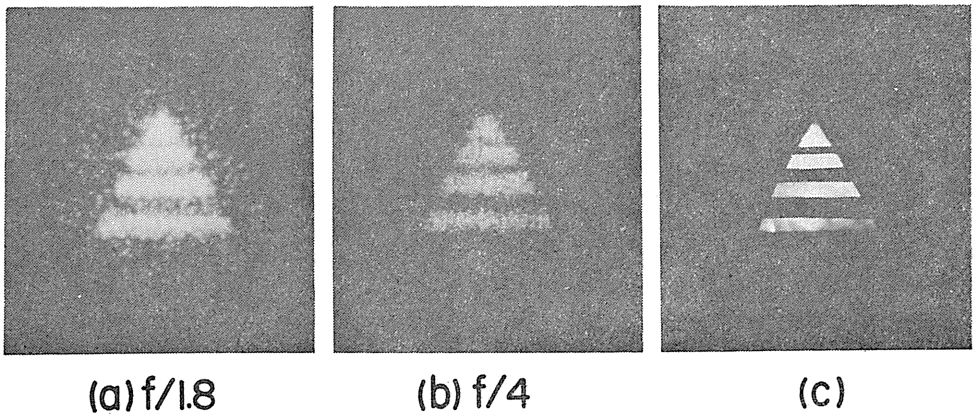

Fig. 5. 7. Spark images of a ^{14}C β-ray source. (a) and (b) were obtained with an identical electric field strength of 5.4 kV/cm for SC and PC gaps and with an exposure time of 2 min (3500 sparks). Lens stop: (a)f/1.8, (b)f/4 using ASA 100 film. (c) shows a film autoradiogram obtained with an exposure time of two weeks.

5. 2. *Air proportional counters*

5. 2. 1. *Primary electron removal in cylindrical counters*

Air proportional counters, i.e. proportional counters using air as a counting gas, would be useful as highly sensitive windowless counters to detect low energy β-rays emitted from surface contaminations by tritium, and as flow-through counters to detect β-activity in air. Although air proportional counters are successfully used as α-ray detectors, they have been considered to be difficult to use as β-ray detectors. This is because usual air proportional counters could not yield high intrinsic efficiency for weakly ionizing β-rays due the removal of primary electrons by attaching to oxygen molecules in air. We must therefore estimate the magnitude of electron attachment in air and find out how to escape attachment for air proportional counters to be used practically for the detection of β-rays.

We now assume that a tritium β-ray was injected into a coaxal cylindrical counter, with anode and cathode radii r_a and r_c, respectively, which was filled with air at atmospheric pressure, and that all the primary electrons having the number n_0 were created on the surface of the cathode. The latter assumption is justified considering a short range of tritium β-rays of about 1 mm on an average in air at atmospheric pressure. These electrons would decrease in number by attaching to oxygen molecules in air during the drift in the counter. If we take the radius r from the axis of the counter and define r_b as a boundary within which the electric field is high enough to cause gas multiplication, we can express the number, n, of free electrons surviving at the point r_b without suffering from electron attachment, using the attachment coefficient η in air, in the form (5.9)

$$n=n_0\cdot\exp\left(-\int_{r_b}^{r_c}\eta\,\mathrm{d}r\right). \tag{5.2}$$

The gas multiplication factor M is given using the first Townsend coefficient α alone in air in the form

$$M=\exp\left(\int_{r_a}^{r_b}\alpha\,\mathrm{d}r\right), \tag{5.3}$$

since no evidence for electron attachment was observed in gas multiplication process in dry air (5.10).

The amplitude of output pulses from proportional counters is proportional to the product of n and M. The factor M does not only change greatly with applied voltage but also fluctuates statistically for a given applied voltage. On the other hand, the number of primary electrons, n_0, created by a tritium β-ray is small — less than a few hundreds — and largely distributing. Hence the ratio n/n_0 of the number of electrons escaped from attachment to that of primary electrons — hereafter refered to as the electron surviving probability — must be kept as large as possible for obtaining a high intrinsic detection efficiency over a wide range of the applied voltage.

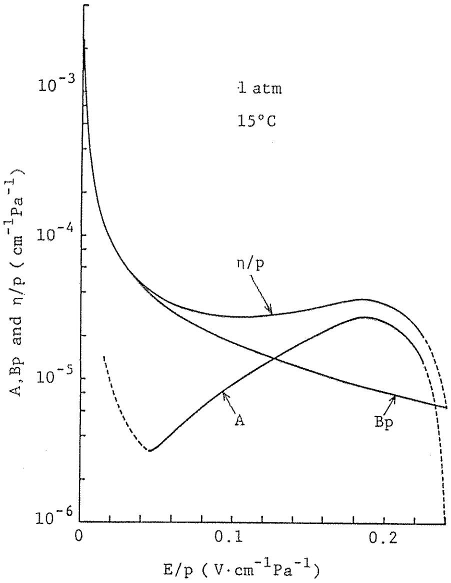

Fig. 5. 8. Attachment coefficients as a function of E/p in air at 1 atm. A, Bp and η/p represent, respectively, the dissociative, three-body and total attachment coefficients per unit pressure.

When electrons are drifting in air along an electric field of strength E, the ratio η/p of the attachment coefficient η to the pressure p of air is given by the expression (5.9)

$$\eta/p=A+Bp, \tag{5.4}$$

where A and B are functions of E/p and correspond, respectively, to dissociative and three-body attachments to oxygen molecules. Experimental values of A (5.11) and calculated values of Bp (5.12) and η/p for air at 1 atm and 15℃ are shown in Fig. 5. 8 over a range of E/p from 0.001 to 0.24 $\mathrm{V\cdot cm^{-1}Pa^{-1}}$ (for E/p larger than 0.24 $\mathrm{V\cdot cm^{-1}Pa^{-1}}$ gas multiplication takes place). For calculating the electron surviving probability n/n_0 by using the relation between η/p and E/p in Fig. 5. 8, Eq. (5.2) must be converted into the function of E/p. The ratio E/p for cylindrical counters is given by

$$E/p=V_0/[pr\cdot\ln(r_c/r_a)], \tag{5.5}$$

where V_0 is the applied voltage. Substituting Eq. (5.5) and the derivative with respect to r into Eq. (5.2), we obtain

$$\ln(n/n_0)=-\frac{V_0}{\ln(r_c/r_a)}\int_{E_c/p}^{E_b/p}\frac{\eta/p}{(E/p)^2}\mathrm{d}(E/p), \tag{5.6}$$

where E_c and E_b are the electric field strength, respectively, at the cathode ($r=r_c$) and at the boundary ($r=r_b$) within which gas multiplication takes place. For approximating the surviving probability n/n_0 to unity, and hence $\ln(n/n_0)$ to zero, the values of E_c/p should be increased to approach E_b/p since E_b/p is constant.

Since the numerator η/p of the integrand of Eq. (5.6) decreases with increasing E/p for $E/p \lesssim 0.1\,\mathrm{V\cdot cm^{-1}Pa^{-1}}$ (see Fig. 5. 8) and the denominator is the square of E/p, $\ln(n/n_0)$ is expected to decrease rapidly with increasing E_c/p. When increasing E_c/p, the gas multiplication factor M must be kept constant. The ratio α/p in air is known to be expressed for large valuse of E/p near the anode wire in the form (5.9)

$$\alpha/p = J\cdot\exp[-K/(E/p)] \tag{5.7}$$

where J and K are constants taking values of $0.113\,\mathrm{cm^{-1}Pa^{-1}}$ and $2.74\mathrm{V\cdot cm^{-1}Pa^{-1}}$ respectively, over the range of E/p between $0.75\sim6.00\,\mathrm{V\cdot cm^{-1}Pa^{-1}}$. Substituting Eqs. (5.5) and (5.7) into Eq. (5.3) we obtain

$$\ln M = \frac{JV_0}{K\cdot\ln(r_c/r_a)}\exp\left[-\frac{Kpr_a\ln(r_c/r_a)}{V_0}\right]. \tag{5.8}$$

The alternative expression of V_0 then is

$$V_0 = \frac{Kpr_a\ln(r_c/r_a)}{\ln[(JV_0)/(K\cdot\ln(r_c/r_a)\cdot\ln M)]}. \tag{5.9}$$

Eq. (5.9) indicates that V_0 is nearly proportional to $pr_a\ln(r_c/r_a)$ when M is constant. Substituting Eq. (5.9) into Eq. (5.5) we can confirm that E_c/p is nearly proportional to r_a/r_c. This implies that the anode radius r_a should be increased and the cathode radius r_c decreased for increasing E_c/p with M constant. Increase of the anode radius r_a, which is preferable to design large size counters, must be limited to obtain a reasonable operating voltage range, since the voltage V_0 also increses with r_a. The electron surviving probability n/n_0 can now be calculated as a function of the cathode radius r_c for a given anode radius r_a. When M, p and r_a are constants, $V_0/\ln(r_c/r_a)$ in Eq. (5.6) becomes constant without depending on r_c, since V_0 is proportional to $\ln(r_c/r_a)$ (see Eq. (5.9)). Substituting a typical value of $V_0=2.5\,\mathrm{kV}$ when $r_a=25\,\mu\mathrm{m}$, $r_c=1.25\,\mathrm{cm}$ and $p=1$ atm into Eqs. (5.5) and (5.6) we can obtain E_c/p and n/n_0 for the values of r_c between 0.05 and 1.25 cm as shown in Table 5.2. The anode radius r_a of $25\,\mu\mathrm{m}$ was decided for obtaining preferable operating voltages below 3 kV. Table 5.2 reveals that the values of n/n_0 decrease rapidly with increasing r_c and that it is necessary to limit the cathode radius within 2∼3 mm for an anode radius of $25\,\mu\mathrm{m}$ to obtain sufficient electron surviving probability in air at atmospheric pressure.

Table 5. 2. Dependence of the electron surviving probability n/n_0 on the cathode radius r_c of cylindrical air proportional counters; anode radius is $25\mu\mathrm{m}$ and the pressure of air is 1 atm at 15°C.

r_c (cm)	0.05	0.1	0.2	0.3	0.4	0.5	1.25
$E_c/p(\mathrm{V\cdot cm^{-1}\cdot Torr^{-1}})$	10.6	5.29	2.65	1.76	1.32	1.06	0.423
$\frac{n}{n_0}=\exp(-\int\eta\cdot dr)$	0.91	0.75	0.38	0.12	0.023	0.0031	10^{-27}

5. 2. 2. *Design consideration for tritium counters*

Although it is necessary to reduce the cathode radius for obtaining a high detection officiency of cylindrical air proportional counters, it results in the reduction of effective area of the counters, which is practically undesirable. Since multianode construction can satisfy a small cathode radius and a large effective area simultaneously, we constructed multiwire counters possessing small anode-cathode distances of 1 and 2 mm and large effective areas of more than 40×40 mm^2. Anode wire spacings of about two times the anode-cathode distances were adopted to approach the electric field around the anode wire to that of coaxal cylinder for utilizing the results in Table 5. 2. In multiwire counters there exist regions which have a low electric field and hence a large attachment probability in the middle of the anode wire spacings. Since the extension of the regions depends on the anode wire spacings for a given anode-cathode distance, the counters possessing different wire spacings were constructed for an anode-cathode distance of 2 mm. Dimensions of these counters are shown in Table 5. 3.

Table 5. 3. Dimensions and characteristics of the experimental multiwire air proportional counters; anode radius is 25μm and detection threshold is 2.1×10^{-15}C.

Detector number	1	2	3	4
Anode-cathode distance (mm)	1	2	2	2
Anode wire spacing (mm)	2	2	3	4
Effective area (mm^2)	42×42	50×50	50×50	60×52
Counter capacitance (pF)	41	61	58	42
Starting voltage (kV)	1. 6	2. 3	2. 1	2. 1
Operating voltage range (V)	350	>500	450	450
Plateau slope (%/100V)	14	16	26	31

Fig. 5. 9 shows the construction of the counters. The anode are made of tungsten wires, 50 μm in diameter. These wires, parallel in each other, were sandwiched between two glass epoxy frames. The cathodes are made of stainless-steel wire meshes (200 per inch) which were glued to both sides of the frames. To suppress leakage current passing through the inside of the frames, Mylar films of 50 μm in thickness were inserted between the anode wires and the frames. Inhomogeneous and anomalous high electric field at the sides of the counters were eliminated by the addition of auxiliary potential electrodes.

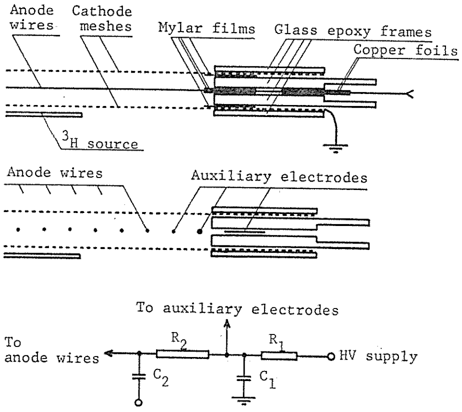

Fig. 5. 9. Schematic diagram of the experimental counter.

Performance of the counters were examined for the detection of tritium β-rays. A tritium disc source, having a diamerer of 2 cm and free from self-absorption, was placed about 0. 5 mm under the cathode mesh in parallel with the mesh. The counter and the source were assembled in a sealed vessel, through which pure air, i. e. ordinary air from which water vapor, carbon dioxide and other contaminants were eliminated, flowed at a constant rate of about 100 ml/min at atmospheric pressure at room temperature to avoid the influence of the change of air components on the counter characteristics. A charge-sensitive pre-amplifier was used to avoid change of the detection threshold by the counter capacities.

In Table 5.3 are shown the starting voltages, operating voltage ranges and plateau slopes for four sorts of the experimental counter. Although good plateaus were not observed for the counters possessing an anode-cathode distance of 2 mm (nos. 2, 3 and 4), they had larger operating voltage ranges. The largest operating voltage range was obtained with the counter (no. 2) possessing an anode-cathode distance and an anode wire spacing of 2 mm each. The plateau slope was smaller for smaller anode wire spacing, and hence the counter (no. 2) possessing the shortest anode wire spacing was also the most satisfactory one in this respect.

5. 2. 3. *Application to a tritium surface-contamination monitor*

5. 2. 3. 1. *Construction*

Newly designed air proportional counters were applied to highly sensitive windowless counters of tritium surface-contamination monitors (5. 13, 5. 14). Fig. 5. 10 shows a construction of the detector part of the monitor. The counter portion located at the bottom of the detector is separated from the upper pre-amplifier box by a partition wall. A multiwire proportional counter with mesh cathodes, which had an anode-cathode distance and an anode wire spacing of 2 mm each, was used as the counter. This geometry produced a long counting plateau with a small plateau slope for tritium β-rays, as described in section 5. 2. 2, when the counter was operated with air. It was found that the thin multiwire counters generated spurious pulses if they were operated with humid air (5. 12). To avoid this problem dry air flowed through the counter at a rate of 0. 5−1 l/min using a small diaphragm pump. The dry air was produced by passing room air into a silica gel cylinder. The air entered the counter through a membrane filter with a pore size of 0. 8 μm and was exhausted through the lower cathode mesh. The mesh had an area of 5.4×5.2 cm^2 and formed the counter sensitive area. A gap of 0. 7 mm was placed between the sensitive area and the surface to be surveyed.

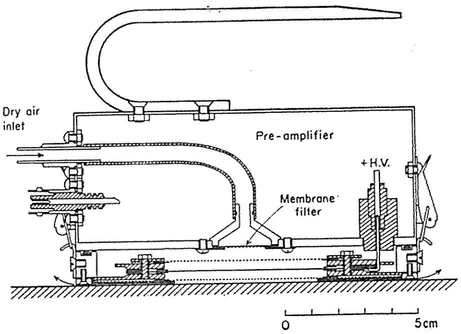

Fig. 5. 10. Detector part of the tritium surface-contamination monitor.

5. 2. 3. 2. *Optimum operating voltage*

Fig. 5. 11 shows counting characteristics of the counter for tritium β-rays and for background. A tritium disc source, the same as that used in section 5. 2. 2, was placed at the center of the counter's sensitive area and at the same level as the surface to be surveyed. The integral counting curves in Fig. 5. 11 were obtained with a discrimination level set at twice the pulse height of the maximum noise pulse. Since it was difficult to determine the optimum operating voltage

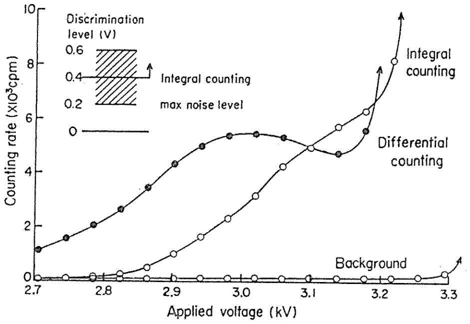

Fig. 5. 11. Counting characteristics of the counter for tritium β-rays and for background. The integral counting curves (open circles) were obtained with a discrimination level twice as large as the maximum noise level. The differential counting curve (closed circles) was obtained by the counting of pulses with a height between the maximum noise level and three times as large as the level.

from these curves, we adopted a different manner. The differential counting curve in Fig. 5. 11 was obtained by only counting pulses whose height fell in the range between the maximum noise level and three times as large as that level. It is seen from Fig. 5. 11 that the curve had the local minimum with an applied voltage of 3140 V. Since the best separation between β-ray pulses and other smaller pulses is attained at this applied voltage (5. 15), 3140 V was determined as the optimum operating voltage of the counter. The smaller pulses in this case were considered to be generated by single electrons which were produced by electron detachment from oxygen negative ions (5. 16) and by the photo-electric effect of incident photons. Since the counter is insensitive for these single electrons, the detector can be used in brightly illuminated places.

5. 2. 3. 3. Detection limit

The detection limit of the monitor for tritium surface contaminations were evaluated as follows. Assuming n_s to be the mean counting rate for a sample including background, and n_b the mean background counting rate, we can calculate the standard deviation δ of the net sample counting rate n_n from the equation

$$\delta=\sqrt{\frac{n_s}{t_s}+\frac{n_b}{t_b}}=\sqrt{\frac{n_n}{t_s}+n_b\left(\frac{1}{t_s}+\frac{1}{t_b}\right)}, \qquad (5.10)$$

where t_s and t_b are the measurement times, respectively, for the sample and for background. Providing that the presence of activities in the sample can be recognized when $n_n \geq K\delta$ (5. 17), where K is the constant, the minimum detectable net sample counting rate m is caluculated from the equation

$$m=K\delta=K\sqrt{\frac{m}{t_s}+n_b\left(\frac{1}{t_s}+\frac{1}{t_b}\right)}. \qquad (5.11)$$

Solving Eq. (5. 11) for m, we obtain for $m>0$ the relation

$$m=\frac{K}{2}\left[\frac{K}{t_s}+\sqrt{\left(\frac{K}{t_s}\right)^2+4n_b\left(\frac{1}{t_s}+\frac{1}{t_b}\right)}\right]. \qquad (5.12)$$

If we take $K=3$, i. e. a 99.7 % confidence level, and $t_s=t_b=t$, Eq. (5. 12) becomes

$$m=\frac{9}{2t}\left(1+\sqrt{1+\frac{8tn_b}{9}}\right). \qquad (5.13)$$

If we substitute $t=0.5$ min and $n_b=200$ cpm for the normal background level into Eq. (5.13) we obtain $m=94$ cpm. The detection limit S_a (Bq·cm^{-2}) for an area source distributed homogeneously on a flat source is evaluated using the value of m from the equation

$$S_a=\frac{m/60}{\varepsilon A}, \tag{5.14}$$

where ε is the β-ray detection probability for the detector per decay of tritium, and A is the sensitive area of the counter. Substituting $\varepsilon=1.76\times10^{-2}$ and $A=5.2\times5.4$ cm^2 into Eq. (5.14), we obtain $S_a=3.2$ Bq·cm^{-2} for sources free from self-absorption with a measurement time of 30 sec, respectively, for a sample and background. The value of S_a fully satisfies the requirement to detect tritium surface contamination within the permissible levels, i.e. 37 Bq·cm^{-2} in controlled areas and 3.7 Bq·cm^{-2} in general areas.

5.2.4. *Application to a tritium-in-air monitor*

5.2.4.1. *Principle and construction*

Air proportional counters were applied to flow-through counters of tritium-in-air monitor (5.18). Fig. 5.12 shows the scheme of the monitor. The detector consists of two layers of identical multiwire counters which have a common mesh cathode in a gas volume, and it operates with sampled air flowing through it. Each counter has 45 anode wires with a spacing of 4 mm, and has an anode-cathode distance of 7.5 mm. As the cathode, 5 mm thick aluminum plates were used for the counter wall, and a fine stainless-steel wire mesh, 50 μm in diameter and 50 per inch, was used between the two layers of the counter in order to minimize secondary electron emission by incident γ-rays.

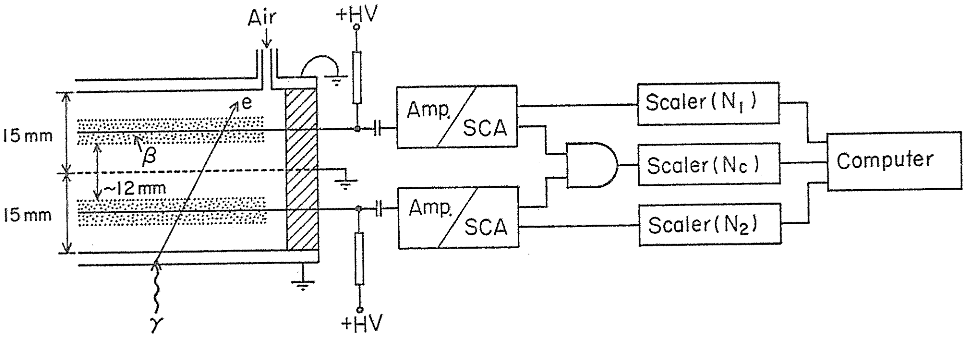

Fig. 5.12. Scheme of an air proportional counter-type tritium-in-air monitor. Dotted regions show the efffective volume of the counters.

A high voltage of 4.8 kV was applied to the anode wires, the cathode being at ground potential. Signal pulses derived from the anode wires of each counter were fed to pre- and linear amplifiers and then height-selected with a conventional single channel analyzer (SCA). The lower level of the SCA was set at twice as large as the maximum noise level, and the upper level was set at 10 V to eliminate huge saturated pulses exceeding 10 V due to α-background in the sampled air and counter materials. Logic pulses derived from each SCA were not only counted independently but also fed to a coincidence circuit. We call the independent counting rates N_1 and N_2, and the coincidence counting rate N_c. Scalers were computer-controlled and each counting rate was processed to obtain an anti-coincidence counting rate $N_a=(N_1-N_c)+(N_2-N_c)$ and a ratio $R=N_a/N_c$.

When a cylindrical proportional counter with an anode diameter of 50 μm operated with air at atmospheric pressure, the effective region around the anode wire was calculated and found to be less than 2 mm from the wire (5. 12). The range of tritium β-rays in air at atmospheric pressure is about 7 mm at the maximum, whereas the effective regions of the counters are separated with a gap of about 12 mm as shown in Fig. 5. 12. This made it impossible for tritium β-rays to be counted in coincidence. On the other hand, cosmic rays and electrons converted in the counter wall by the incidence of environmental γ-rays have generally long ranges, and they can pierce both effective ranges and be counted in coincidence. By this principle it would be possible to separate the signal of tritium β-rays from that of background radiations. In addition, the present monitor is expected to have no memory effect for tritium, since β-rays emitted from tritium deposition on the counter wall can scarcely reach the effective regions.

5. 2. 4. 2. Tritium monitoring in a γ-ray field

The ratio $R=N_a/N_c$ was verified to be independent of the intensity, energy and incident direction of γ-rays, though it varied with pressure and humidity of the sampled air (5. 18). The variation of R was ascribed to the dependence of the effective regions around each anode wire on the pressure and humidity at a constant temperature (5. 18, 5. 19).

When the value of R is known at a given pressure, temperature and humidity, background counting rates can be evaluated in real time from observed values of the coincidence counting rate N_c.

Fig. 5. 13 shows the change of the anti-coincidence rate N_a and the coincidence rate N_c with lapse of time, which was measured with a constant pressure and temperature and with a counting time of 1 min. After 25 min from the start of the measurement, tritium gas with an activity of 1620 Bq was injected into the detector from a slit opened at the center of the counter wall. At 40 min ^{137}Cs γ-rays were irradiated for 10 min with an exposure rate of 1. 7 mR/hr. At 65 min the tritium gas was purged by a constant flow of dry air with a rate of 0. 8 l/min.

It is seen from this figure that the values of N_c were independent of the presence of tritium and they increased solely when γ-rays were irradiated. A net counting rate N_n by tritium β-rays was calculated by subtracting the product of N_c and R from N_a, and the values of N_n are shown in Fig. 5. 13 as closed squares. It can be found that the calculated values of N_n were on a single line independent of γ-ray irradiation.

For the purging of tritium gas, air to an amount of three times the detector volume was enough, and the values of N_a returned to the same background level as at the beginning.

A detection efficiency of about 14 % was obtained for tritium β-rays, and a detection limit of 2.4×10^4 Bq$\cdot$m^{-3} was obtained with a normal background level and a counting time of 30 sec.

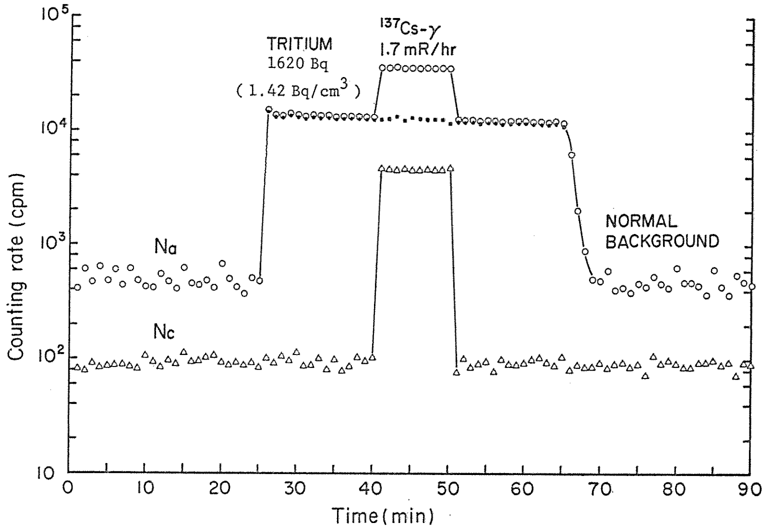

Fig. 5. 13. Tritium monitoring in a γ-ray field. 1000mb, 24°C. Closed squares show the net counting rate N_n for tritium β-rays calculated by $N_n = N_a - RN_c$, where $R = 5.0$ is a constant.

5. 3. *Background-compensated GM counters*

5. 3. 1. *Principle and construction*

When low level β-activities are to be measured with GM counters it is desirable to obtain net counts without γ-background through a single measurement. Two types of new background-compensated GM counter were designed and constructed (5.20) as shown in Fig. 5. 14. Each has a Teflon diaphragm of 7 mm thickness, which divides the counter into two parts, i. e. a front part A and a rear part B, and absorbs β-rays with energy up to 2 MeV. β-rays entered through the Mylar window are therefore counted in part A alone, and not in part B which counts only background radiations. In type I, the presence of a tiny 10 MΩ resistor between the anode wires of two parts yields different pulse shapes and heights from the two parts. Since the sensitive volumes in both parts are the same, the net count rate by β-rays in part A is obtained simply by taking the difference of the count rates in both parts.

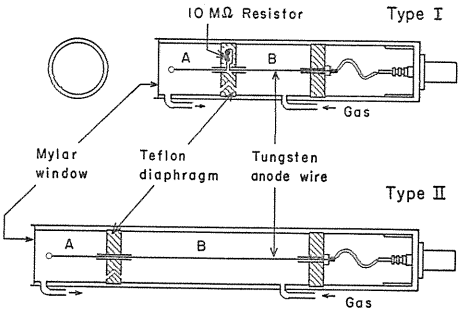

Fig. 5. 14. Background-compensated GM counter in two types.

5. 3. 2. *Electronic circuitry and counter characteristics*

Electrical connection in type I and its equivalent circuit are shown in Fig. 5. 15. When a charge q is deposited by an impulse current input on the anode wire of part A or B, an output voltage $v(t)$ is given as a function of time t by the expression

$$v(t)=\frac{qR_b}{\alpha}\left\{\frac{\gamma X_1+1}{X_1-X_2}e^{X_1t}+\frac{\gamma X_2+1}{X_2-X_1}e^{X_2t}\right\}, \tag{5.15}$$

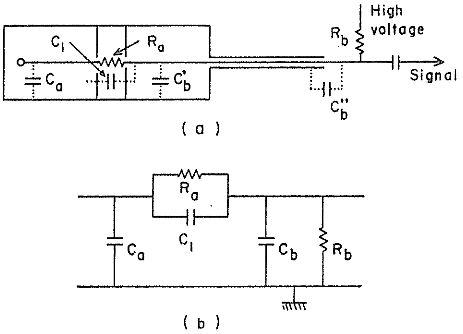

Fig. 5. 15. Electrical connection in counter type I (a) and its equivalent circuit (b).

where

$$X_1=\{-G+(G^2-4H)^{1/2}\}/2,$$

$$X_2=\{-G-(G^2-4H)^{1/2}\}/2,$$

$$G=\beta/\alpha, \qquad H=1/\alpha,$$

and when charge q is deposited on the anode wire in part A

$$\alpha=R_aC_a(R_bC_b-R_aC_1),$$

$$\beta=R_aC_a+R_bC_b+R_bC_a,$$

$$\gamma=R_aC_a,$$

or when q is deposited on the anode wire in part B

$$\alpha=R_aR_b(C_aC_b+C_aC_1+C_bC_1),$$

$$\beta=R_a(C_a+C_1)+R_b(C_a+C_b),$$

$$\gamma=R_aC_1.$$

In an actual GM discharge, the charge input $Q(t)$ on an anode wire is given by the equation

$$Q(t)=-Ne\ln\left\{\frac{2V\mu}{a^2p\ln(b/a)}t+1\right\}/\{2\ln(b/a)\}, \tag{5.16}$$

where Ne is the total charge input, V is the applied high voltage, μ is the ion mobility, p is the gas pressure, and a and b are the radii of the anode wire and the cathode, respectively. An actual output voltage is calculated by combining Eq. (5.15) and Eq. (5.16). Oscilloscope traces of the pre-amplifier output obtained with type I are shown in Fig. 5.16. Full line A

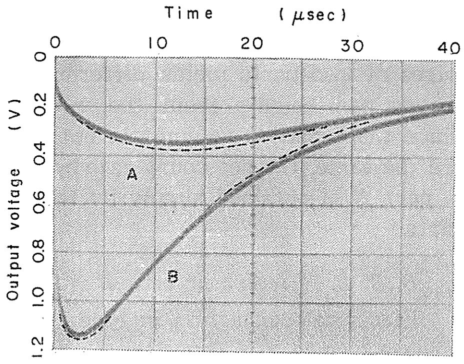

Fig. 5. 16. Pulse shapes obtained with counter type I. A and B show the shapes from part A and part B, respectively. Full lines are oscilloscope traces of a pre-ampliffier output. Dashed lines are calculated shapes.

shows the pulse shape from part A and the line B from part B. Broken lines are calculated shapes. Conventional pulse height discriminators can easily distinguish pulses from part A and B.

The ratio $k(=n_{AB}/n_{BB})$ of the background count rate n_{AB} in part A to the rate n_{BB} in part B was 1.011 ± 0.012 for type I and 0.429 ± 0.010 for type II. The net count rate n_β of β-rays emitted from a source is expressed with a standard deviation σ in the form

$$n_\beta \pm \sigma = n_A - k n_{BB} \pm \left\{ \frac{n_A}{t} + (n_{BB}\sigma_k)^2 + k^2 \frac{n_{BB}}{t} \right\}^{1/2}, \tag{5.17}$$

where $n_A = n_\beta + n_{AB}$, t is the measuring time and σ_k is the standard deviation of k.

The accuracy was calculated for the net count rate by β-rays emitted from a source with 15 Bq under a detection efficiency of 15%. Relative standard deviation σ_{rel} $(=\sigma/n_\beta)$ are shown in Table 5.4 for three counters, i.e. type I, type II and a conventional end-window counter. The table indicates that these counters give nearly the same accuracy despite the measuring time for type I and II counters is a half of that for the conventional counter.

Table 5.4. Comparison of measuring time and obtainable accuracy (σ_{rel}) among three counters—conventional, type I and type II counters.

	Conventional	Type I	Type II
n_β [cpm]	135	135	135
n_{AB} [cpm]	50.8	18.6	21.8
n_{BB} [cpm]		18.6	50.8
Measuring time [min]	1×2	1	1
σ_{rel} [%]	11.4	12.4	12.0

5. 3. 3. Application to a survey meter

Background-compensated GM counters were used as the probes of GM survey meter to obtain net count rate by β-rays from radioactive sources in a quick survey (5.21). However, there seems to be two problems. Firstly, the probes are generally held in the hand and pointed to various directions, and the background ratio of part A to part B may depend on the incident direction of background γ-rays. The deviation of the ratio from the average was confirmed experimentally to be permissible for the present purpose.

Secondly, the small pulses generated during the recovery time after a full Geiger discharge in part B may have the pulse height less than the discrimination level. These small pulses from part B will then be counted as if they were generated in part A. A retriggerable single pulse was generated by the triggering of a full Geiger discharge in part B and was used as an anti-gating pulse not to count any pulses in channel A, as shown in Fig. 5.17.

The relative standard deviation $\sigma_{rel} = \sigma_v/V$ of a differential rate meter output V for the indication of β intensity is given by the expression

$$\sigma_{rel} = [(1 + n_{AB}(1+k)/n_\beta)/2n_\beta\tau]^{1/2}, \tag{5.18}$$

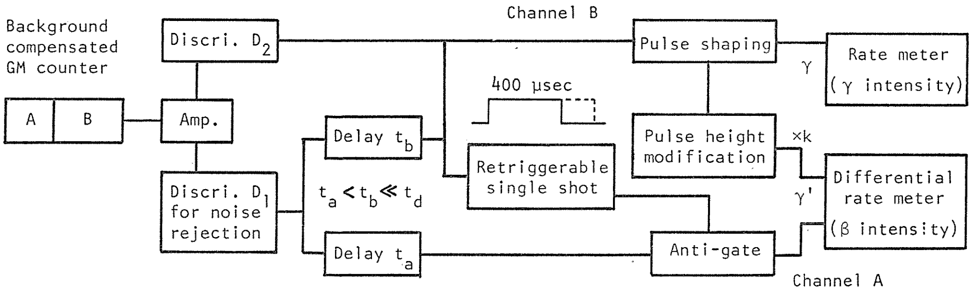

Fig. 5. 17. Circuit block diagram of the survey meter with the background-compensated GM counter.

where τ is the time constant of the rate meter.

The error σ_{rel} in the measurement of a surface contamination with an α- or β-emitter was calculated, and shown in Table 5. 5, under the conditions that a time constant $\tau=12$ sec, a measuring time $t=60$ sec, a detection efficiency 10 %, a background count rate $n_{\mathrm{BB}}=110$ cpm and a window area of the counter 4. 7 cm^2. A β-contamination can be measured down to one-tenth of the maximum permissible level in a single measurement.

Table 5. 5. Relative standard deviation in the measurement of surface contamination with an α- or β-emitter.

Maximum permissible surface contamination (μCi/cm^2)		Contamination level	n_{net} (cpm)	σ_{rel} (%)
α	10^{-4}	×1	102	21. 4
β	10^{-3}	×1/10		

5. 4. *A tritium-in-air monitor using liquid scintillation counter*

It is required to measure the concentration of tritium in environmental air around nuclear facilities. Since tritium is a pure β-emitter with a low β-ray energy of 18 keV at the maximum, the detection is rather difficult. Various methods were reported of tritium-in-air monitoring (5. 22). We developed a new method of the monitoring in which tritiated water vapor is cold trapped with liquid nitrogen and detected with conventional liquid scintillation counters (5. 23).

A sample air containing tritium were prepared by heating a tritium target used for a neutron generator in a sealed box with a volume of 126 liters. Vials with a volume of 30 cm^3 for liquid scintillation counting were used as bottles for the cold trap. Two tubes made of glass or copper were passed through the cap of the vial, and the sample air flowed in the vial and was then exhausted from it through these tubes. The vials were cooled with liquid nitrogen. In order to determine the yield of cold trapping, three traps were connected in series. A yield of 50~70 % was obtained, and it was independent of the humidity of the sample air. Detection limit of 6.7×10^2 Bq·m^{-3} obtained from our experiments satisfied the requirement to detect tritium concentration in air within permissible levels.

6. Summary

Our studies on the detection and measurement of radiation and radioactivity have been described.

Very thin films through which a few keV electrons were able to pass could be prepared and the mean free path length, energy loss and penetration range for low energy radiations were measured.

Gas multiplication factors for proportional counters were studied theoretically and experimentally, and new formulas which were applicable to wide ranges of counting gas pressure and applied voltage were introduced.

Error in the measurement of radioactivity standardization by $4\pi\beta$-γ coincidence absorption method for radionuclides emitting β- and γ-rays has been reduced to be less than 0.1 percent. Studies to make radioactive sources and backing films which have less absorption of β-rays and to improve instrumentations for the activity measurement are necessary in order to get higher accuracy. Position sensitive proportional counters were successfully applied to the absolute measurement of radioactivity of gaseous samples.

The air proportional counter which used air as counting gas was developed to detect β-rays. The counter can be applied for monitorings of tritium surface contamination and tritium concentration in an environmental air.

A new hybrid spark chamber was developed for imaging of the geometrical distribution of β-ray emitting nuclides.

Acknowledgements

Authors wish to thank Messrs. S. Hirokawa and K. Yanagida and a number of graduates of our laboratory for their collaboration. A part of the works was supported by the Grant in Aid for Science Research from the Ministry of Education, Science and Culture of Japan.

References

2. 1) Quinn J. J., Phys. Rev. **126** (1962) 1453.
2. 2) Kanter H., Phys. Rev. **B 1** (1970) 2357.
2. 3) Ishigure N., Mori C. and Watanabe T., J. Phys. Soc. Jpn. **44** (1978) 1196.
2. 4) Mori C., Koike J. and Watanabe T., Nucl. Instr. Meth. **121** (1974) 253.
2. 5) Ishigure N., Mori C. and Watanabe T., ibid. **135** (1976) 473.
2. 6) Jull G., Proc. Phys. Soc. (GB) **69** (1956) 1237.
2. 7) Klemperer O. and Shepherd J. P. G., Brit. J. Appl. Phys. **14** (1963) 85.
2. 8) Kunz C., Z. Phys. **167** (1963) 53.
2. 9) Peterson L. R. and Green A. E. S., Proc. Phys. Soc. ser. 2, **1** (1968) 1131.
2.10) Rohlich F. and Carlson B. C., Phys. Rev. **93** (1954) 38.
2.11) Gryzinsky M., Phys. Rev. **138** (1965) 305.
2.12) Garber F. W., Nakai M. Y., Hanter J. A. and Birkhoff R. D., J. Appl. Phys. **42** (1971) 1149.

2.13) Kalil F., Stone W. G., Hubell H. H. Jr. and Birkhoff R. D., ORNL-2731 (1959).
2.14) Ishigure N., Mori C. and Watanabe T., J. Phys. Soc. Jpn. 44 (1978) 973.
2.15) Sugiyama H., Bull. Electrotech. Lab. Jpn. 38 (1974) 352.
2.16) Mizuno M., Mori C. and Watanabe T., Oyo Buturi 48 (1979) 532 (in Japanese).
2.17) Blodgett K. and Langmuir I., Phys. Rev. **51** (1937) 964.
2.18) Mizuno M., Mori C. and Watanabe T., Oyo Buturi 45 (1976) 514 (in Japanese).
2.19) Henke B. L. and Anderson M. W., Proc. 6th Int. Conf. X-ray Optics Microanalysis, Tokyo (Univ. of Tokyo Press, Tokyo, 1971) p. 367.
2.20) Mizuno M., Mori C. and Watanabe T., Oyo Buturi 49 (1980) 138 (in Japanese).
2.21) Fink M. and Yetes A. C., Atomic Data **1** (1970) 385.
2.22) Mori C., Noguchi H., Mizuno M. and Watanabe T., Jpn. J. Appl. Phys. **19** (1980) 725.
2.23) Mori C., Noguchi H., Ishigure N. and Watanabe T., Nucl. Instr. Meth. **164** (1979) 113.
2.24) Cole A., Radiat. Res. 38 (1960) 7.
2.25) Davis M., Phys. Rev. **94** (1954) 243.
2.26) ICRU Report 16, Linear Energy Transfer (ICRU Publication, Washington D. C., 1970) p. 42.
2.27) Tolansky S., Multiple beam interferometry of surfaces and films (Univ, Press, Oxford, 1948).
2.28) Anderson H. L., Nucl. Instr. Meth. **12** (1969) 111.
2.29) Miyahara H., Yoshida M. and Watanabe T., Radioisotopes **26** (1977) 761 (in Japanese).
2.30) Feldman C., Phys. Rev. **117** (1960) 455.
2.31) Mori C., Noguchi H., Ishigure N. and Watanabe T., Nucl. Instr. Meth. **155** (1978) 435.
2.32) Mori C., Radioisotopes 23 (1974) 681.
3. 1) Diethorn W., US AEC Report NYO-6628 (1956).
3. 2) Williams A. and Sara R. I., Int. J. Appl. Rad. Isot. **13** (1962) 229.
3. 3) Charles M. W., J. Phys. E **5** (1972) 95.
3. 4) Zastawny A., J. Sci. Instr. **43** (1966) 179.
3. 5) Miyahara H., Watanabe M. and Watanabe T., Nucl. Instr. Meth. **A241** (1985) 186.
3. 6) Mori C., Noguchi H., Ishigure N. and Watanabe T., ibid. **155** (1978) 435.
3. 7) Baerg A. P., Bowes G. C. and Adams R. J., "Standardization of Radionuclides" IAEA (1967) p. 91.
3. 8) Tomitani T., Nucl. Instr. Meth. **100** (1972) 179.
3. 9) Miyahara H., Watanabe M. and Watanabe T., ibid. **A251** (1986) 156.
3.10) Watanabe T., Mori C., Aoyama T. and Christmas P., ibid. **178** (1980) 121.
3.11) Aoyama T., ibid. **A234** (1985) 125.
3.12) Hanna G. C., Kirkwood D. H. W. and Pontecorvo B., Phys. Rev. **75** (1949) 985.
3.13) Campion P. J., Int. J. Appl. Rad. Isot. **19** (1968) 219.
3.14) Mori C., Uno M. and Watanabe T., Proc. INS Int. Symp. Nucl. Rad. Detectors, Tokyo (1981) p. 403.
3.15) Mori C., Uno M. and Watanabe T., Nucl. Instr. Meth. **196** (1982) 49.
3.16) Mori C., Noguchi H., Mizuno M. and Watanabe T., Jpn. J. Appl. Phys. **19** (1980) 725.
3.17) Cochran L. W. and Forester D. W., Phys. Rev. **126** (1962) 1785.
3.18) Cottrel T. L. and Walker I. C., Trans. Faraday Soc. **61** (1956) 1585.
3.19) West D., Progress in Nucl. Phys. **3** (1953)18.
3.20) Mori C. and Watanabe T., Nucl. Instr. Meth. **204** (1982) 149.
3.21) Koori N., Sakai H., Sakae T., Matoba M. and Kumabe I., Jpn. J. Appl. Phys. **25** (1986) L986.
3.22) Mori C. and Watanabe T., J. Nucl. Sci. Technol. **22** (1985) 461.
3.23) Sugiyama H., Jpn. J. Appl. Phys. **15** (1976) 1779.
3.24) Mori C., Nakamoto M., Uritani A. and Watanabe T., J. Nucl. Sci. Technol. **21** (1984) 942.
3.25) Matoba M., Tsuji K., Marubayashi K. and Shintake T., Nucl. Instr. Meth. **165** (1979) 469.
3.26) Kalbitzer S. and Melzer W., Nucl. Instr. Meth. **56** (1967)301.

3.27) Mori C., Aoyama T. and Watanabe T., J. Nucl. Sci. Technol. **23** (1986) 214.
4. 1) Mann W. B., Proc. Informal Conference, NRC-573 (1958) 23.
4. 2) Campion P. J., Int. J. Appl. Radiat. Isotopes **4** (1959) 232.
4. 3) Baerg A. P., Metrologia **2** (1966) 23.
4. 4) Baerg A. P., Nucl. Instr. Meth. **112** (1973) 143.
4. 5) Gandy A., Int. J. Appl. Radiat. Isotopes **11** (1961) 75.
4. 6) Gandy A., ibid. **13** (1962) 501.
4. 7) Bryant J., ibid. **14** (1963) 143.
4. 8) Grigorescu L., Nucl. Instr. Meth. **112** (1973) 151.
4. 9) Smith D., ibid. **152** (1978) 505.
4.10) Cox D. R. and Isham V., Proc. Roy. Soc. London **A356** (1977) 149.
4.11) Watanabe T., Miyahara H., Suzuki K. and Takeuchi N., Radioisotopes (Tokyo) **16** (1967) 457 [in Japanese].
4.12) Watanabe T. and Takeuchi N., Oyo Buturi, **33** (1964) 322 [in Japanese].
4.13) Rytz A., Rapport BIPM-77/4 (1977).
4.14) Plch J., Zederadička J. and Kokta L., Int. J. Appl. Radiat. Isotopes **24** (1973) 65.
4.15) Miyahara H., Suzuki M. and Watanabe T., Radioisotopes (Tokyo) **27** (1978) 439.
4.16) Miyahara H., Yoshida M. and Watanabe T., ibid. **28** (1979) 33.
4.17) Miyahara H., Suzuki M. and Watanabe T., ibid. **27** (1978) 625.
4.18) Miyahara H. and Watanabe T., ibid. **30** (1981) 195.
4.19) Miyahara H., Takiguchi Y. and Watanabe T., Nucl. Instr. Meth. **204** (1982) 203.
4.20) Baerg A. P., Bowes G. C. and Adams R. J., "Standardization of Radionuclides", IAEA, Viena (1967) 91.
4.21) Miyahara H., Momose T. and Watanabe T., Radioisotopes (Tokyo) **33** (1984) 867.
4.22) Lowenthal G.C. and Smith A. M., Nucl. Instr. Meth. **30** (1964) 363.
4.23) Colas C. and Rytz A., Rapport BIPM-71/1 (1971).
4.24) Watanabe T., Inda J. and Genka T., Radioisotopes (Tokyo) **21** (1972) 69 [in Japanese].
4.25) Miyahara H., Yoshida M. and Watanabe T., ibid. **25** (1976) 437 [in Japanese].
4.26) Miyahara H., Yoshida M. and Watanabe T., ibid. **26** (1977) 708.
4.27) Rytz A., Nucl. Instr. Meth. **157** (1978) 131.
4.28) Rytz A., Rapport BIPM-80/2 (1980) and Nucl. Instr. Meth. **192** (1982) 427.
4.29) Campion P. J., Taylor J. G. V. and Merritt J. S., Int. J. Appl. Radiat. Isotopes 8 (1960) 8.
4.30) Yoshida M., Miyahara H. and Watanabe T., ibid. **28** (1977) 633.
4.31) Miyahara H., Mizuno M. and Watanabe T., Nucl. Instr. Meth. **228** (1985) 397.
4.32) Baltakmens T., ibid. **142** (1977) 535.
4.33) Kawada Y. and Kimura M., Int. J. Appl. Radiat. Isotopes **22** (1971) 251.
4.34) Miyahara H. and Watanabe T., ibid. **35** (1984) 345.
4.35) Miyahara H., Momose T. and Watanabe T., Appl. Radiat. Isotopes **37** (1986) 1.
4.36) Yoshida M., Miyahara H. and Watanabe T., Radioisotopes (Tokyo) **26** (1977) 767 [in Japanese].
4.37) Carswell D. J. and Milsted J., J. Nucl. Energy **4** (1957) 51.
4.38) Bruninx E. and Rudstam G., Nucl. Instr. Meth. **13** (1961) 131.
4.39) Pate B. D. and Yaffe L., Canad. J. Chem. **34** (1956) 265.
4.40) Ujihira Y. and Roy J. C., ibid. **46** (1954) 1221.
4.41) Van der Eijk W. and Vaninbroukx R., Nucl. Instr. Meth. **97** (1971) 131.
4.42) Miyahara H., J. Phys. Soc. Japan **27** (1969) 1062.
4.43) Vonnegut B. and Neubauer R. L., J. Colloid Sci. **7** (1952) 616.
4.44) Drozin V. G., ibid. **10** (1955) 158.
4.45) Langer L. M., Rev. Sci. Instrum. **20** (1949) 216.
4.46) Baerg A. P., Meghir S. and Bowes G. C., Int. J. Appl. Radiat. Isotopes **15** (1964) 279.
4.47) Wyllie H. A., Johnson E. P. and Lowenthal G. C., ibid. **21** (1970) 497.
4.48) Merritt J. S., Taylor J. G. V. and Campion P. J., Canad. J. Chem. **37** (1959) 1109.
4.49) Lowenthal G. C. and Wyllie H. A., Int. J. Appl. Radiat. Isotopes **24** (1973) 415.

4.50) Yoshida M., Miyahara H. and Watanabe T., Radioisotopes (Tokyo) **24** (1975) 851 [in Japanese].

4.51) Miyahara H. and Watanabe T., ibid. **28** (1979) 506.

4.52) Gleason G. I., Taylor J. D. and Tabern D. L., Nucleonics **8** (5) (1951) 12.

4.53) Evans R. D., The Atomic Nucleus, McGraw-Hill Book Co., New York (1952) p. 627.

4.54) Baker R. G. and Katz L., Nucleonics **11** (2) (1953) 14.

4.55) Gora E. K. and Hickey F. C., Anal. Chem. **26** (1954) 1158.

4.56) Roalsvig J. P. and Haslam R. N. H., Canad. J. Phys. **37** (1959) 499.

4.57) Yoshida M., Miyahara H. and Watanabe T., Radioisotopes (Tokyo) **27** (1978) 1.

4.58) Allen R. A., Int. J. Appl. Radiat. Isotopes **1** (1957) 289.

4.59) Watanabe T. and Takeuchi N., Oyo Buturi **35** (1966) 876 [in Japanese].

4.60) Miyahara H. and Watanabe T., Radioisotopes (Tokyo) **27** (1978) 69 [in Japanese].

4.61) Nuclear Data Group (ORNL), Nucl. Data Sheets **5** (1971) 131.

4.62) Miyahara H., Gotoh T. and Watanabe T., Int. J. Appl. Radiat. Isotopes **32** (1981) 573.

4.63) Brandhorst H. W. Jr and Cobble J. W., Phys. Rev. **125** (1961) 1323.

4.64) Petterson H., Autman S. and Grunditz Y., Z. Phys. **233** (1970) 260.

4.65) Macias E. S., Phelps M. E. and Sarantites D. G., Phys. Rev. **C14** (1976) 639.

4.66) Niday J. B., ibid. **98** (1954) 42.

4.67) Baba S., Baba H. and Natsume H., J. Inorg. Nucl. Chem. **33** (1971) 589.

4.68) Debertin K., Z. Naturf. **26a** (1971) 596.

4.69) Houtermans H., Milosevic O. and Reinchel F., Int. J. Appl. Radiat. Isotopes **31** (1979) 153.

4.70) Miyahara H. and Watanabe T., ibid. **36** (1985) 75.

4.71) Mann W. B., Seliger H. H., Marlow W. F. and Medlock R. W., Rev. Sci. Instrum. **31** (1960) 690.

4.72) Hoizumi K. and Takeuchi N., Proc. 19th Ann. Meeting on Radioisotopes in Physical Sciences and Industry. Tokyo (1982) p. 137 [in Japanese].

4.73) Mori C., Fujii Y. and Watanabe T., Int. J. Radiat. Appl. Instrum. Part A **38** (1987) 371.

4.74) Mori C., Fujii Y. and Watanabe T., ibid. **38** (1987) 379.

4.75) Mori C., Nakamoto M., Uritani A. and Watanabe T., J. Nucl. Sci. Technol. **21** (1984) 942.

5. 1) Aoyama T., Kamata K., Kobayashi Y. and Watanabe T., Radioisotopes **24** (1975) 305. [in Japanese]

5. 2) Aoyama T., Inagaki K. and Watanabe T., Radioisotopes **25** (1976) 191 [in Japanese].

5. 3) Aoyama T., Inagaki K. and Watanabe T., Radioisotopes **25** (1976) 199 [in Japanese].

5. 4) Aoyama T. and Watanabe T., Radioisotopes **27** (1978) 7 [in Japanese].

5. 5) Aoyama T. and Watanabe T., Nucl. Instr. and Meth. **150** (1978) 203.

5. 6) Aoyama T. and Watanabe T., Nucl. Instr. and Meth. **174** (1980) 291.

5. 7) Llewellyn Jones F. and Morgan C. G., Proc. Roy. Soc. **A-218** (1953) 88.

5. 8) Loeb L. B., Basic processes of gaseous electronics (Univ. of California Press, Berkeley, 1961) p. 826.

5. 9) Brown S. C., Introduction to electrical discharges in gases (J. Wiley, New York, 1966) pp. 99, 130.

5.10) Moruzzi J. L. and Price D. A., J. Phys. **D 7** (1974) 1434.

5.11) Chatterton P. A. and Craggs J. D., Proc. Phys. Soc. **85** (1965) 355.

5.12) Aoyama T. and Watanabe T., Nucl. Instr. and Meth. **205** (1983) 311.

5.13) Aoyama T., Miyai H. and Watanabe T., Nucl. Instr. and Meth. **221** (1984) 644.

5.14) Aoyama T. and Watanabe T., Health Phys. 48 (1985) 773.

5.15) Houtermans H., Miguel M. and Werner E., Proc. Symp. on Standardization of Radionuclides (IAEA, Vienna, 1967).

5.16) Aoyama T., Mori T. and Watanabe T., Nucl. Instr. and Meth. **212** (1983) 281.

5.17) Kishida M. and Suga S., Radioisotopes **26** (1977) 823 [in Japanese].

5.18) Aoyama T., Sugiura H. and Watanabe T., Nucl. Instr. and Meth. **A254** (1987) 620.

5.19) Aoyama T., Totogawa M. and Watanabe T., Nucl. Instr. and Meth. **A255** (1987) 524.
5.20) Mori C., Kumanomido H. and Watanabe T., Nucl. Instr. and Meth. **211** (1983) 429.
5.21) Mori C., Kumanomido H. and Watanabe T., Nucl. Instr. and Meth. **228** (1984) 177.
5.22) Kato J. et al., JAERI-memo **Nos. 2233, 2246, 2283** (1966) [in Japanese].
5.23) Watanabe T., Mizuno S. and Kosaka K., Radioisotopes **22** (1973) 44 [in Japanese].